THE MAGNETOCALORIC EFFECT

AT A FIRST ORDER PHASE TRANSITION

by

Milan Bratko

Imperial College London, Department of Physics

A Thesis submitted for the Degree of Doctor of Philosophy

ABSTRACT

The magnetocaloric effect (MCE) can be defined as the isothermal entropy change (or adiabatic temperature change) of a material upon application/removal of an external magnetic field and is the key physics for a magnetic cooling device. A discontinuity of entropy at a first order phase transition (FOPT) allows for a large entropy change to be induced by a relatively small field. However, a hysteresis is necessarily associated with a FOPT.

The effects of hysteresis, as measured in a sensitive microcalorimeter, are the focus of the thesis. The calorimetric setup used is unique in allowing a separate measurement of heat capacity and latent heat and thereby the possibility to clearly distinguish the first and higher order contributions to MCE. Due to the high measurement fidelity required, the experimental chapter is a core component of the thesis and includes a thorough analysis of the measurement errors associated with the microcalorimeter. Several improvements are proposed to improve precision and accuracy of the measurement in future studies.

The first of the hysteresis effects is a spurious 'colossal' MCE. Its indirect observation was claimed in 2004 from magnetisation measurements analysed using a Maxwell relation and was widely disputed thereafter. It was shown that a different measurement protocol leads to non 'colossal' MCE. This thesis investigates whether the 'colossal' MCE can be achieved by a particular magnetisation history by reproducing the original measurement protocol in a more direct calorimetric measurement. It is shown that the 'colossal' MCE is just an artefact of the use of Maxwell relation in a non-equilibrium process.

The final chapter discusses a second effect of hysteresis: a subtle difference between the indirect and calorimetric measurements of MCE that can be clearly observed when comparing measurements on field application and removal. Maxwell relation leads to an artefact related to temperature dependence of the hysteresis. In the calorimetric measurement the dissipation of magnetic work in a hysteretic magnetisation cycle is observed.

DECLARATION OF ORIGINALITY

I hereby declare that the work presented here is entirely my own. Where I have incorporated the work of others it has been acknowledged and referenced appropriately.

Milan Bratko
September 2013

COPYRIGHT DECLARATION

The copyright of this thesis rests with the author and is made available under a Creative Commons Attribution Non-Commercial No Derivatives licence. Researchers are free to copy, distribute or transmit the thesis on the condition that they attribute it, that they do not use it for commercial purposes and that they do not alter, transform or build upon it. For any reuse or redistribution, researchers must make clear to others the licence terms of this work.

ACKNOWLEDGMENTS

I would like to thank my supervisors Dr Karl G Sandeman and Prof Lesley F Cohen for their support and guidance. A special thanks goes to Karl for patiently answering the same questions over and over again and also for being on call in the more stressful moments of my PhD.

A huge thanks goes to Dr Kelly Morisson who was there, holding my hand when I was taking my first steps with the microcalorimeter. Always happy to help, answer a question, dig out that paper or just chat.

I would also like to thank Prof David Caplin, Dr Adam Gilbertson and Dr Zsolt Gercsi for some useful discussions; Katharina Zeissler, Dr Karen Yates, Dr Ulli Hannemann, Dr Rob Maher and Dr Tyler Roschuk for some entertaining tea-times; Themis for making coffee. Big thanks to Dr Michèle Piscitelli for being a friend.

Finally, I would like to thank my friends and family back home, who may not have been involved all that much but who offered a perfect break and lots of support when needed.

I would also like to acknowledge the funding through EPSRC Doctoral Training Award.

PUBLICATIONS

- Milan Bratko, Kelly Morrison, Ariana de Campos, Sergio Gama, Lesley F. Cohen, and Karl G. Sandeman. History dependence of directly observed mangetocaloric effect in (Mn, Fe)As. *Appl. Phys. Lett.*, 100:252409, 2012.

- Kelly Morrison, Milan Bratko, Jeremy Turcaud, Andrey Berenov, A. David Caplin, and Lesley F. Cohen. A calorimetric method to detect a weak or distributed latent heat contribution at first order magnetic transitions. *Rev. Sci. Instrum.*, 83:033901, 2012.

Contents

Table of Contents **6**

List of Figures **8**

List of Tables **10**

1 Introduction **11**
1.1 Basic thermodynamics and measurement of MCE 14
1.1.1 Indirect determination of MCE 16
1.1.2 Calorimetric methods and direct ΔT measurement 18
1.2 MCE in first order phase transitions 19

2 Experimental Methods **27**
2.1 Vibrating Sample Magnetometer 27
2.2 Microcalorimeter Overview 29
2.3 AC Heat Capacity Probe 31
2.3.1 Principle of Operation 31
2.3.2 Deviations from Simple Model 33
2.3.3 Seebeck Coefficient Calibration 40
2.3.4 Measurement Setup 42
2.3.5 High Accuracy Considerations 43
2.3.6 Measurement Error Summary 64
2.4 Quasi-adiabatic Temperature Probe for Latent Heat Measurement 65
2.4.1 Principle of operation 66
2.4.2 Measurement Setup 67
2.4.3 Measurement Error 68

3 Analysis **72**
3.1 Latent Heat Contribution to Entropy Change 72
3.2 Heat Capacity Contribution to Entropy Change 73
3.2.1 Integral of Heat Capacity Change across a First Order Phase Line . . 75
3.2.2 An Accurate Separation of Entropy Change Contributions 76
3.2.3 Treatment of hysteretic systems 80
3.3 Utilising the interplay between latent heat and heat capacity 82
3.3.1 Measuring the Equilibrium Entropy Change of a First Order Phase Transition 84

3.4 Propagation of Errors 84

4 'Colossal' magnetocaloric effect: Is it an artefact or history-dependent effect? 86
4.1 Review of the 'colossal' magnetocaloric effect in MnAs and other compounds 86
4.2 The sample — $Mn_{0.985}Fe_{0.015}As$ 102
4.3 Magnetisation Measurements 103
4.4 Measurements in Microcalorimeter 104
4.4.1 Heat Capacity 106
4.4.2 Latent Heat 108
4.4.3 Total Isothermal Entropy Change 110
4.4.4 Latent Heat in a Mixed-phase State 111
4.5 Summary 113

5 Further effects of hysteresis on the magnetocaloric effect 114
5.1 Irreversibility in conventional MCE 115
5.1.1 Issues in magnetometry estimates beyond the 'colossal' artefact . . . 115
5.1.2 Comparison with calorimetry 119
5.2 Irreversibility in inverse MCE 124
5.2.1 The sample — CoMnSi 124
5.2.2 Magnetometry estimates 125
5.2.3 Irreversibility in calorimetry 127
5.3 Summary 132

6 Conclusions 134

7 Further Work 137

Bibliography 138

A Copyright Permissions 145

List of Figures

1.1 Basic refrigeration cycle utilising MCE 12
1.2 MCE in ErAgGa (Pecharsky et al., 2001) 16
1.3 A schematic T-S diagram in the vicinity of a first order phase transition (Pecharsky et al., 2001) 20
1.4 A schematic T-S diagram for ΔT_{ad} (Pecharsky et al., 2001) 21
1.5 Schematic of isothermal entropy change and adiabatic temperature change for a first order phase transition (Pecharsky et al., 2001) 22
1.6 Heat capacity/entropy in $Gd_5Si_2Ge_2$ (Pecharsky et al., 2001) 23
1.7 Magnetisation data and entropy change estimates in $Gd_5Si_2Ge_2$ (Pecharsky and Gschneidner, 1997a) 24

2.1 PPMS VSM schematic, after Quantum Design (2008). 28
2.2 The Xensor TCG-3880 gauge (van Herwaarden, 2013) 30
2.3 Basic thermal circuit representing the heat capacity measurement. 31
2.4 Plots for Seebeck coefficient calibration 41
2.5 Schematic of the experimental setup for heat capacity measurement. 44
2.6 Flow chart of the core of the LabVIEW data acquisition loop 44
2.7 Low-pass filter on the thermopile output. 45
2.8 Low-pass filter transfer properties at room temperature 47
2.9 Erroneous addition to the measured values of heat capacity (C) and heat exchange coefficient (G_{ac}) due to the low-pass filter 48
2.10 Temperature fluctuations in R_{shunt} 51
2.11 R_{shunt} as a function of heater power 54
2.12 LIA output at usual settings 59
2.13 LIA output at modified settings 62
2.14 Schematic of the instrumentation used for the latent heat measurement. . . 68
2.15 Thermopile response to latent heat calibration pulses 69

3.1 Schematic of an isothermal entropy change as measured using the ac heat capacity probe 77
3.2 Schematic of an alternative analysis method for determining the heat capacity contribution 79
3.3 Analysis for treatment of a hysteretic system 81
3.4 Measuring latent heat in ac heat capacity probe 83
3.5 Measuring an equilibrium entropy change of an FOPT 85

4.1 First report on MCE in MnAs (Wada and Tanabe, 2001) 87
4.2 First report of 'colossal' MCE (Gama et al., 2004) 88
4.3 *P-T* magnetic phase diagram of MnAs (Menyuk et al., 1969) 89
4.4 Structural and magnetic phase diagram for $Mn_{1-t}Fe_tAs$ (Fjellvåg et al., 1988) 90
4.5 Isothermal magnetisation data on $Mn_{1-x}Fe_xAs$ for x = 0.006 (de Campos et al., 2006) 91
4.6 'Colossal' MCE reported at ambient pressure in $Mn_{1-x}Fe_xAs$ (de Campos et al., 2006) 91
4.7 'Colossal' MCE in MnAs at ambient pressure (von Ranke et al., 2006) 92
4.8 'Colossal' peak comparison with calorimetry in $La_{0.7}Pr_{0.3}Fe_{11.5}Si_{1.5}$ (Liu et al., 2007) 93
4.9 Correction for phase coexistance (Liu et al., 2007) 94
4.10 Phase diagram of MnAs (Tocado et al., 2009) 96
4.11 Magnetic phase diagram of $MnFeP_{0.8}Ge_{0.2}$ (Caron et al., 2009) 97
4.12 Magnetisation data and entropy change estimates for $MnFeP_{0.8}Ge_{0.2}$ - 'standard process' (Caron et al., 2009) 98
4.13 Magnetisation data and entropy change estimates for $MnFeP_{0.8}Ge_{0.2}$ - 'loop process' (Caron et al., 2009) 98
4.14 Modelled hysteretic magnetisation data (Amaral and Amaral, 2009) 100
4.15 Modeled entropy change – actual vs. estimated by Maxwell relation (Amaral and Amaral, 2009) 100
4.16 Phase diagram of $Mn_{0.985}Fe_{0.015}As$ 102
4.17 Hisotry-dependent magnetometry in $Mn_{0.985}Fe_{0.015}As$ 105
4.18 Example of heat capacity measurement in $Mn_{0.985}Fe_{0.015}As$. 107
4.19 Integration reference point fitting for $Mn_{0.985}Fe_{0.015}As$ 109
4.20 Example of latent heat measurement in $Mn_{0.985}Fe_{0.015}As$ 110
4.21 History-dependence in calorimeter ($Mn_{0.985}Fe_{0.015}As$) 111

5.1 Extended magnetisation data for $Mn_{0.985}Fe_{0.015}As$ 116
5.2 Isothermal entropy change estimates from magnetometry for $Mn_{0.985}Fe_{0.015}As$ 117
5.3 Phase diagram for $Mn_{0.985}Fe_{0.015}As$ 118
5.4 $Mn_{0.985}Fe_{0.015}As$ — comparison of irreversibility in magnetometry and calorimetry 122
5.5 Hysteresis loss in an isothermal magnetisation loop in $Mn_{0.985}Fe_{0.015}As$ . . . 123
5.6 Phase diagram of CoMnSi 125
5.7 Magnetisation data for CoMnSi 126
5.8 CoMnSi isothermal entropy change estimates from magnetisation data . . . 127
5.9 Heat capacity measurement in CoMnSi 128
5.10 Fitting of reference points in CoMnSi 129
5.11 Latent heat measurement in CoMnSi 130
5.12 Comparison of irreversibility in magnetometry and calorimetry (CoMnSi). . 131

List of Tables

2.1 Characteristic thermal exchange length in the heat capacity probe 35
2.2 Typical errors considered in the latent heat calculation. 70

4.1 Latent heat component of isothermal entropy change in a mixed-phase state at 295 K (fragment 2). 112

5.1 Repeated latent heat measurement in $Mn_{0.985}Fe_{0.015}As$ 120
5.2 Hysteresis loss in CoMnSi 132

Chapter 1

Introduction

Recently there has been a great interest in the magnetocaloric effect (MCE) as a basis for solid state magnetic refrigeration. This technology has several potential advantages over the conventional vapour-compression refrigeration systems. Most often the conventional systems use volatile fluorinated gases. The ozone-depleting CFCs have been banned already and their replacements in the form of HCFCs (to be banned in the near future) and HFCs are both very potent greenhouse gases (Coulomb, 2010). Solid state refrigeration offers an environmentally friendly alternative. Furthermore, higher energy efficiency should be attainable, stemming mostly from high tunability of the magnetocaloric properties, e.g. by composition. Thus the solid state refrigerant can by optimised for a particular application and its power requirement (Sandeman, 2011).

The MCE can be defined as either the adiabatic temperature change or isothermal entropy change of a material upon application or withdrawal of an external magnetic field. The isothermal entropy change in MCE is usually attributed to the magnetic entropy change (e.g. its reduction caused by spin alignment in magnetic field). In adiabatic conditions, when the entropy is conserved, this has to be compensated by an opposing lattice entropy change. Thus, if the magnetic entropy decreases, the lattice entropy increases correspondingly, resulting in a temperature increase of the material. The use of the effect in a refrigeration cycle is illustrated in figure 1.1.

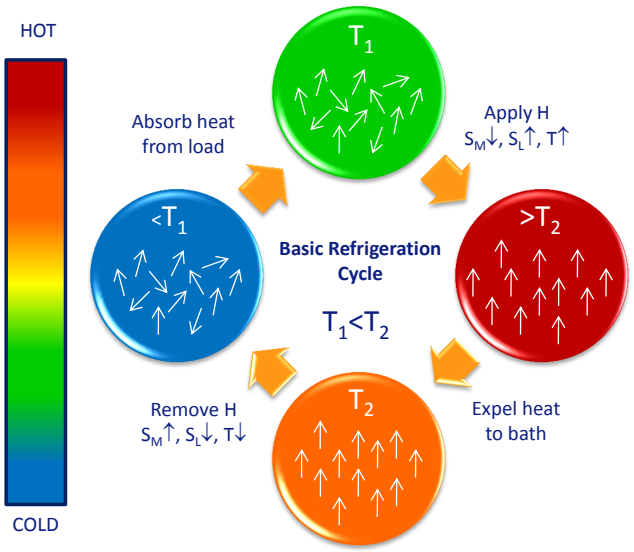


Figure 1.1 Schematic representation of a simple magnetic refrigeration cycle. Starting from top, magnetic field is applied adiabatically resulting in temperature increase of the refrigerant above the temperature of the hot reservoir. Heat is expelled into the hot reservoir. Magnetic field is removed adiabatically resulting in temperature decrease of the refrigerant below the temperature of the heat load. Heat is transferred from the heat load (cold reservoir) to the refrigerant.

A reversible magnetic field-induced temperature change of a material was discussed theoretically by Lord Kelvin already in 1860 (Thomson, 1860). First experimental measurement of *magnetocaloric effect* was done in Ni in the vicinity of its Curie temperature by Weiss and Piccard (1917). Most of the subsequent research was focused on adiabatic demagnetisation of paramagnetic salts, which was used to achieve temperatures below 1 K (Giauque and MacDougall, 1933). The first heat pump prototype operating at room temperature was built in 1976 (Brown, 1976). The magnetocaloric material used was gadolinium, a rare-earth metal undergoing second order magnetic phase transition at its Curie temperature near room temperature.

Nevertheless, the real interest in room temperature refrigeration was sparked by the discovery of *giant* magnetocaloric effect around 280 K in $Gd_5Si_2Ge_2$ (Pecharsky and Gschneidner, 1997a). It was demonstrated that the temperature at which a large MCE exists could be tuned to between 280 K and 20 K by substituting Ge for Si (Pecharsky and Gschneidner, 1997b) and even above room temperature, without reducing the size of MCE, by alloying with small amount of Ga (Pecharsky and Gschneidner, 1997c).

The giant MCE in $Gd_5Si_2Ge_2$ is associated with a first order magnetostructural phase transition. The reported isothermal entropy changes were at least twice as big as those of the benchmark second order material, gadolinium. After this discovery, the research focus shifted from second order transitions to first order. This soon led to a controversial report of 'colossal' MCE in MnAs under pressure, which surpassed the theoretical limit for magnetic entropy change (Gama et al., 2004). It was quickly followed by a 'colossal' MCE in ambient conditions achieved by substituting Fe for Mn (de Campos et al., 2006). In both cases, the MCE was measured indirectly from isothermal magnetisation loops. Nevertheless, there is usually a large thermal and field hysteresis associated with first order magnetostructural transitions which can lead to significant history-dependent effects, such as metastable mixed-phase states. The anomalous 'colossal' MCE was more recently attributed to such effects, e.g. Liu et al. (2007).

In the context of the current interest in magnetocaloric systems that possess a first order

phase transition (FOPT), this thesis focuses on the hysteresis and its effect on the MCE and its measurement. Indirect method of MCE determination (from magnetisation data) is compared with calorimetric measurements. The latter were performed in *microcalorimeter*, a unique setup enabling a separate measurement of latent heat and heat capacity as a function of applied field.

The remainder of the introduction covers basic thermodynamic concepts of MCE and its measurement techniques. It is followed by an experimental methods chapter which focuses on the microcalorimeter in great detail as it has been used for a measurement requiring very high fidelity. As a result a thorough understanding of its current limitations has been achieved and several improvements were proposed. Thus, the experimental chapter forms an essential part of the thesis. In chapter 3 an analysis method is developed for an accurate conversion of latent heat and heat capacity into first and higher order contributions to entropy change. These concepts were utilised in the two results chapters. Chapter 4 studies the aforementioned 'colossal' MCE. It is concluded that the 'colossal' MCE is just an artefact of an improper use of Maxwell relation. The final chapter (chapter 5) studies more subtle effects of irreversibility in a simple magnetisation/demagnetisation cycle. While the magnetisation estimates provide a non-physical result, a dissipation of irreversible magnetic work is observed in the calorimetric measurement.

1.1 Basic thermodynamics and measurement of MCE

Conventional MCE is usually observed in materials that have a continuously varying order parameter, and therefore either have no phase transition or a second (or higher) order phase transition of some kind. At room temperature, large MCEs are usually only associated with a phase transition, and so this section focuses on the thermodynamics of phase transitions.

Second order phase transitions involve changes of the order parameter only. Therefore the total entropy is a continuous function of temperature regardless of magnetic field.

Furthermore, the transition can be considered to be fully reversible, and so the total entropy is a single-valued function of state. As a result, the thermodynamics is somewhat more straightforward in these systems. For this reason they will be considered first and the concepts will then be extended to first order materials.

As already indicated, the MCE in solids is essentially the result of the entropy variation due to the coupling of a magnetic spin system with an applied magnetic field. The total entropy of a magnetic material with localised magnetic moments can be expressed as the sum of the magnetic, lattice, and electronic contributions (S_M, S_L, and S_E, respectively) (Tishin and Spichkin, 2003). Thus, at constant pressure, the total entropy of a magnetic material can be presented as

$$S(T,H)_P = [S_M(T,H) + S_L(T,H) + S_E(T,H)]_P. \tag{1.1}$$

Since, in general, all three contributions depend on temperature and magnetic field, they cannot be clearly separated. This is the case especially in the low-temperature region, where the electronic entropy and electronic heat capacity can exhibit strong nonlinear dependencies on temperature as well as magnetic field. Nevertheless, to a first approximation the lattice and electronic parts of entropy can be considered to be independent from magnetic field (Tishin and Spichkin, 2003). Thus, MCE is usually attributed to the change of magnetic entropy.

Using a mean-field model of a magnetic material, an upper limit on the magnetic entropy change can be calculated (Tishin and Spichkin, 2003)

$$|\Delta S_{M,max}| = R\ln(2J+1), \tag{1.2}$$

where R is the universal gas constant and J is the total angular momentum of the magnetic atom. This assumes that the action of the magnetic field is to completely order the spins, each of total angular momentum J.

Figure 1.2 shows two isofield entropy curves for a second order material and indicates the two parameters that are usually used to quantify the MCE — isothermal entropy

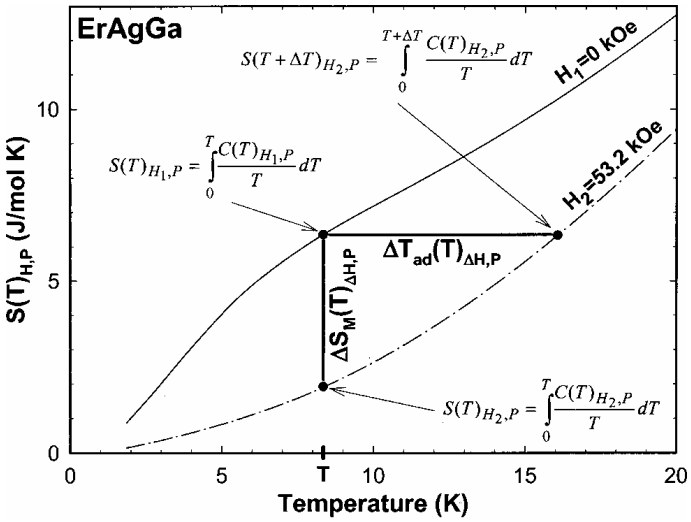


Figure 1.2 The total entropy functions of ErAgGa in magnetic fields 0 and 53.2 kOe. The thick vertical and horizontal bars show the magnetocaloric effect in terms of isothermal entropy change and adiabatic temperature change respectively. Reprinted figure with permission from Pecharsky et al. (2001). Copyright 2001 by the American Physical Society.

change or adiabatic (isentropic) temperature change. Here the entropy change is attributed to magnetic entropy change, ΔS_M, only.

1.1.1 Indirect determination of MCE

The total isothermal entropy change is most often inferred indirectly from magnetisation data using Maxwell relation

$$\left(\frac{\partial S}{\partial H}\right)_T = \left(\frac{\partial M}{\partial T}\right)_H. \tag{1.3}$$

The Maxwell relation can be derived from Gibbs free energy, G, which can be defined for a paramagnetic salt as

$$G = U - MH - TS. \tag{1.4}$$

Here U is the internal energy of the material. In differential form, as given by the first law of thermodynamics

$$dU = đQ + đW, \tag{1.5}$$

where $đQ$ is the heat flowing into the system and $đW$ is the external work done on the system — the magnetic work in case of paramagnetic salt. For an infinitesimal reversible process

$$đQ = TdS. \tag{1.6}$$

By combining equations 1.4, 1.5, and 1.6 a total differential of Gibbs free energy can be obtained

$$dG = -SdT - MdH. \tag{1.7}$$

Thus,

$$S = -\left(\frac{\partial G}{\partial T}\right)_H \quad \text{and} \quad M = -\left(\frac{\partial G}{\partial H}\right)_T.$$

By partially differentiating S with respect to H and M with respect to T, we get

$$\left(\frac{\partial S}{\partial H}\right)_T = \frac{\partial^2 G}{\partial T \partial H} \quad \text{and} \quad \left(\frac{\partial M}{\partial T}\right)_H = \frac{\partial^2 G}{\partial H \partial T}.$$

Since the right-hand side terms are equal, the Maxwell equation 1.3 can be obtained. Nevertheless, it is important to note that by the use of equation 1.6 the application of Maxwell relation is restricted to reversible quasi-static equilibrium processes.

Analytical integration of equation 1.3 is impossible since magnetisation is material-dependent and is generally an unknown function of temperature and magnetic field. Numerical integration is usually performed on a finite number of isofield or isothermal magnetisation curves, e.g.

$$\Delta S(T)_{H_1 \to H_2} = \sum_{i=1}^{\frac{H_2 - H_1}{\Delta H}} \frac{M(T + \Delta T/2, H_1 + i\Delta H) - M(T - \Delta T/2, H_1 + i\Delta H)}{\Delta T} \Delta H \tag{1.8}$$

where ΔH and ΔT correspond to the field and temperature steps in magnetisation measurements. This approach is usually the first choice because of the straightforwardness of magnetisation measurement. Due to the time required to stabilise the system at a given temperature, an isothermal measurement is usually preferred over an isofield magnetisation measurement.

1.1.2 Calorimetric methods and direct ΔT measurement

Alternatively, the MCE can be determined from a calorimetric measurement. The heat capacity at constant parameter x is defined as

$$C_x = \left(\frac{đQ}{dT}\right)_x, \tag{1.9}$$

Combining equations 1.9 and 1.6, the isofield entropy curves at a field H can be calculated as

$$S(T)_H = \int_0^T \frac{C(T)_H}{T} dT. \tag{1.10}$$

Although the lower limit of the integral is impossible to reach, it is important to approach it as close as possible in order to avoid problems with the constant of integration (from the third law of thermodynamics $S(T) \to 0$ as $T \to 0$). Again, the use of equation 1.6 assumes reversibility of the magnetisation/de-magnetisation process. The isothermal entropy change or adiabatic temperature change for a given field variation can be determined by comparing two isofield entropy curves at different fields, as indicated on figure 1.2. If only zero-field heat capacity measurement is available, the adiabatic temperature change can be inferred indirectly by using the zero-field total entropy curve and isothermal entropy change data from magnetisation measurements to construct an in-field entropy curve, e.g. in Pecharsky and Gschneidner (1997a). This approach, was necessary in the early days as the measurement of heat capacity in magnetic field was not usual and readily available.

In fact the MCE research stimulated development of several calorimeters operating in magnetic field. Most of these are Differential Scanning Calorimeters (DSCs), for instance by Marcos et al. (2003); Basso et al. (2008); Jeppesen et al. (2008). In a DSC measurement, there are two (ideally identical) heat flow sensors and a sample is mounted on one of them. Conventionally, the DSC is operated in a temperature-sweeping mode at constant pressure and magnetic field. The differences in heat flow between the two sensors are attributed to sample heat capacity.

The DSCs listed above do also operate in a field-sweeping mode. Rather than heat capacity, an enthalpy associated with the field variation is measured by the heat flow. The

entropy change is given by integration of equation 1.6 yielding

$$\Delta S(T)_{H_1 \to H_2} = \frac{\Delta Q_{H_1 \to H_2}}{T} = \frac{\int_{H_1}^{H_2} \frac{\dot{Q}}{\dot{H}} dH}{T}. \tag{1.11}$$

A calorimetric technique similar to DSC is Differential Thermal Analysis (DTA), where instead of maintaining the same temperature of the two sensors, an equal heat flow is provided. An alternative to DSC or DTA is a relaxation (or heat pulse) technique where a heat pulse is applied to the sample. The sample heat capacity is derived from the decay of the heat pulse into bath through a well-defined thermal link. This is available also in commercial systems such as Quantum Design Physical Properties Measurement System (PPMS).

The heat capacity measurement technique employed here, ac calorimetry, is much less common in the MCE field. A detailed discussion of the technique is covered in chapter 2.

Another direct method of measuring the MCE is the measurement of the adiabatic temperature change (Dankov et al., 1997; Gopal et al., 1997). In such a measurement, special care needs to be taken to ensure adiabatic conditions and good thermal contact of the thermometer with the sample.

1.2 MCE in first order phase transitions

Whereas in second order materials the total entropy is a continuous function of temperature, at a first order phase transition there is a discontinuous change of entropy. This discontinuity is associated with a change of order rather than the change of order parameter only. As a result there is an isofield enthalpy associated with the transformation, ΔE_H, which is the latent heat of the first order transition. The first order character of the transition requires a coupling to a secondary field. Thus, the first order phase transition is typically a coupled magnetostructural or magnetoelastic transition. Another feature characteristic of first order materials is hysteresis, which results in a finite region of irreversibility of the phase transition. In order to use any of the equations introduced in the previous

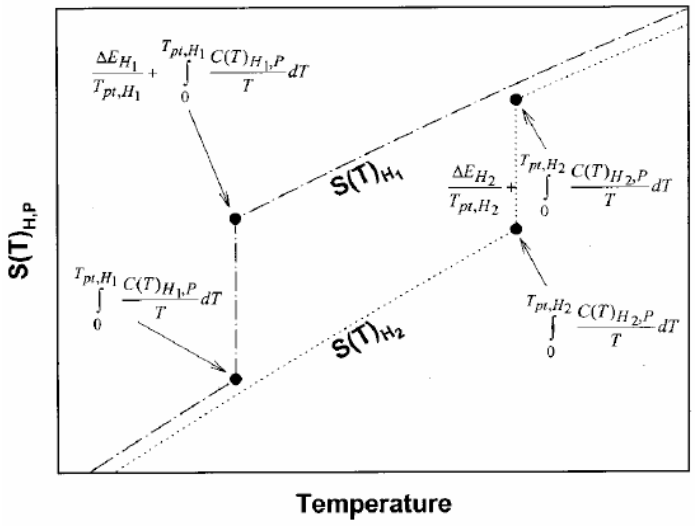


Figure 1.3 A schematic T-S diagram of a magnetic system in the vicinity of the first order phase transition in two magnetic fields, H_1 and H_2. It is assumed that the magnetic field has a small but finite effect on the heat capacities. Reprinted figure with permission from Pecharsky et al. (2001). Copyright 2001 by the American Physical Society.

section, the hysteresis must be assumed to be negligible.

Figure 1.3 shows a schematic T-S diagram with a model system where magnetic field stabilises the low temperature phase (i.e. transition moves to higher temperatures with increasing field) and it has a small effect on the heat capacity both below and above the transition.

In order to take into account the enthalpy change, equation 1.10 needs to be modified

$$S(T)_H = \int_0^{T_{pt,H}} \frac{C(T)_{H,LT}}{T} dT + \frac{\Delta E_H}{T_{pt,H}} + \int_{T_{pt,H}}^{T} \frac{C(T)_{H,HT}}{T} dT, \tag{1.12}$$

where indices LT and HT indicate the heat capacity before and after the phase transformation, respectively. T_{pt} is the temperature of phase transformation in a field H. Assuming that there is only a small change in heat capacity at the phase transition, and that it has a negligible field dependence, i.e. $C_{H_1,LT} \approx C_{H_2,LT} \approx C_{H_1,HT} \approx C_{H_2,HT}$, the isothermal entropy change is dominated by the enthalpy change and it is non-zero only in the range

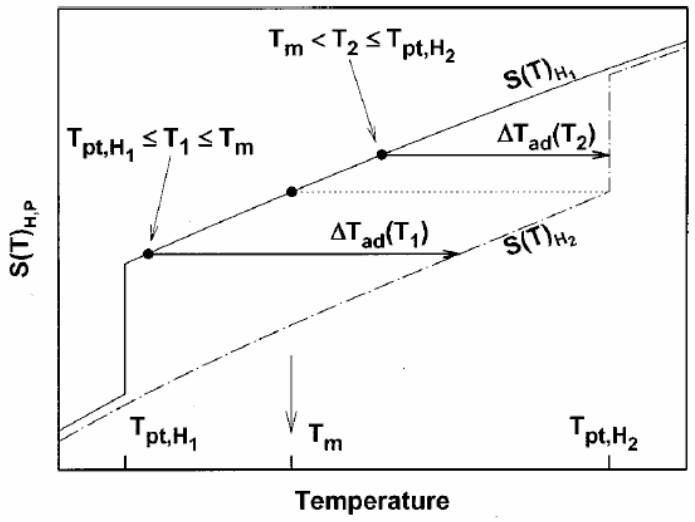


Figure 1.4 A schematic T-S diagram in the vicinity of first order phase transition in two different magnetic fields, H_1 and H_2. There is a temperature T_m above which ΔT_{ad} cannot exceed T_{pt,H_2} (horizontal arrow at T_2). Below this temperature, ΔT_{ad} reaches a plateau. Reprinted figure with permission from Pecharsky et al. (2001). Copyright 2001 by the American Physical Society.

$T_{pt,H_1} < T < T_{pt,H_2}$ where

$$\Delta S(T)_{H_1 \to H_2} = S(T)_{H_2} - S(T)_{H_1} \approx \frac{\Delta E_{H_1}}{T_{pt,H_1}}. \tag{1.13}$$

This results in a characteristic plateau in the plots of isothermal entropy change vs. temperature for first order materials.

Adiabatic temperature change has a slightly different behaviour. As illustrated in figure 1.4, the adiabatic temperature change reaches a plateau in the range from T_{pt,H_1} to T_m, however, it cannot exceed T_{pt,H_2} above T_m and gradually decreases to zero as T_{pt,H_2} is approached. The different behaviour of isothermal entropy change and adiabatic temperature change is depicted in figure 1.5.

Due to the discontinuity in entropy at first order phase transition, one might expect problems in experimental measurements of the MCE. In general, however, the same meth-

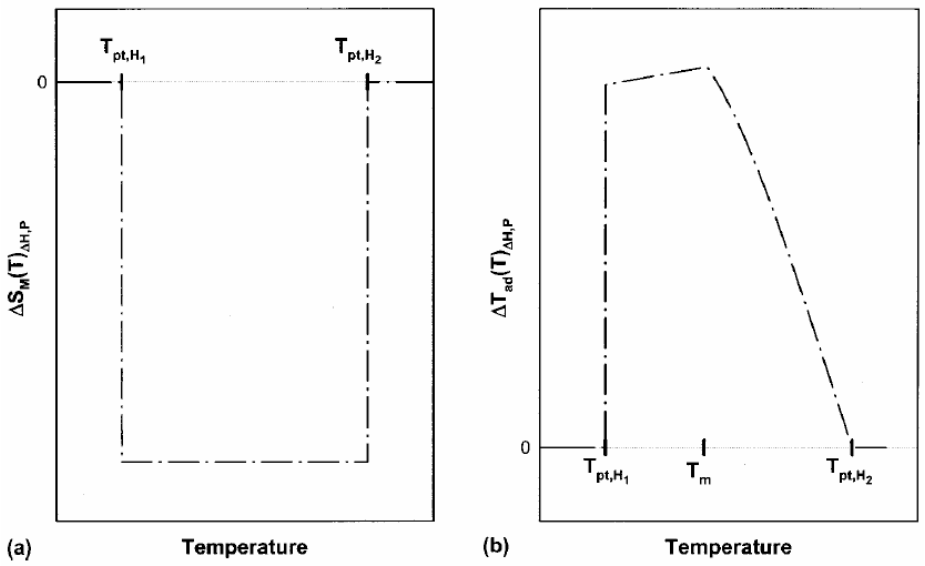


Figure 1.5 Schematic of isothermal entropy change and adiabatic temperature change for a typical first order phase transition. Reprinted figure with permission from Pecharsky et al. (2001). Copyright 2001 by the American Physical Society.

ods used to measure MCE in second order materials are also used for first order materials. In the calorimetric measurement, the latent heat term in equation 1.12 theoretically corresponds to an infinite heat capacity at the phase transition temperature. In reality the first order transition happens in a finite temperature range rather than at fixed temperature and the amount of latent heat is finite. In a temperature-sweeping DSC the latent heat is usually picked up as a spike in heat capacity around the transition temperature. Such a calorimetric measurement, performed on $Gd_5Si_2Ge_2$ is shown in figure 1.6. The figure also shows the resulting entropy curves. It can be noticed that due to finite temperature range of the transition, the entropy curves are not truly discontinuous.

Similar problems should be expected when determining the entropy change from magnetisation data. Theoretically, first order magnetic phase transitions should have a discontinuous jump in magnetisation as function of temperature or field. Thus, the Maxwell relation, equation 1.3, should fail to describe the MCE since the differential $(\partial M/\partial T)_H$

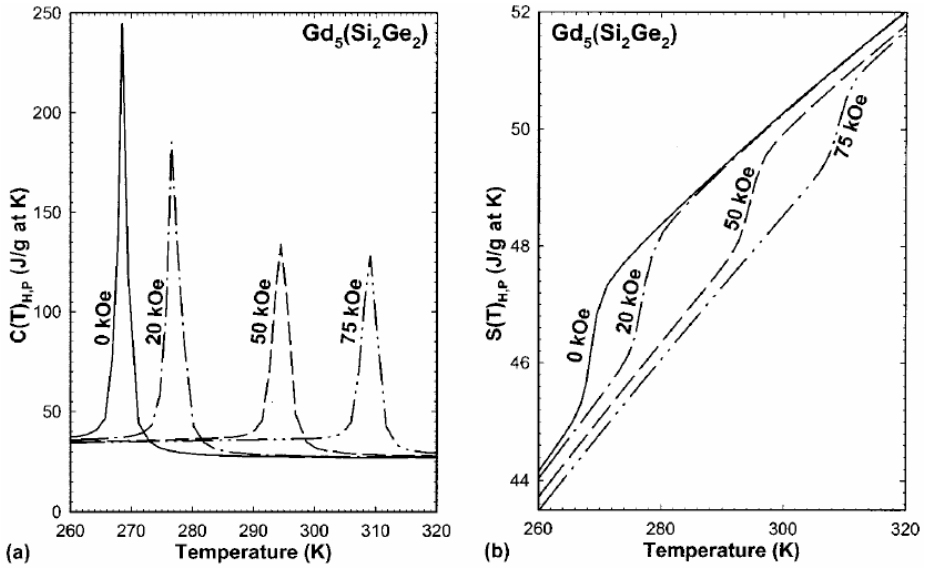


Figure 1.6 (a) The heat capacity and (b) total entropy of $Gd_5Si_2Ge_2$ at constant pressure in magnetic fields 0, 20, 50, and 75 kOe. Despite a theoretically infinite heat capacity at the phase transition, large but finite heat capacities are recorded in an actual experimental measurement. Reprinted figure with permission from Pecharsky et al. (2001). Copyright 2001 by the American Physical Society.

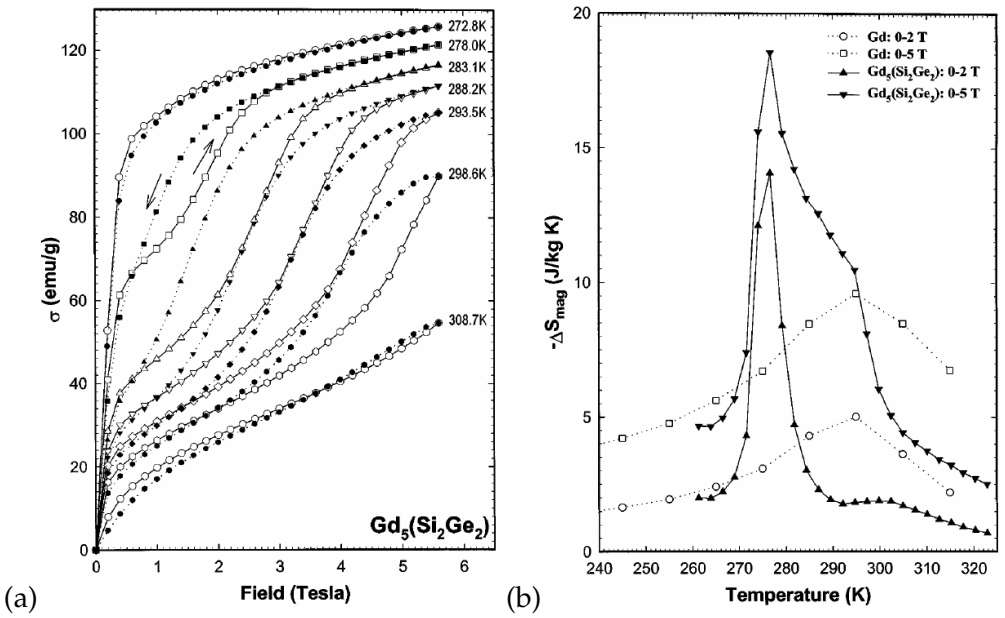


Figure 1.7 (a) The isothermal magnetisation data for $Gd_5Si_2Ge_2$. Data displays finite field range of the transition as well as field hysteresis of the transition. (b) Giant isothermal entropy change as inferred from the magnetisation data using Maxwell relation for field variation 0 to 2 T and 0 to 5 T. For comparison, open symbols show the entropy change of gadolinium, benchmark second order material. Reprinted figure with permission from Pecharsky and Gschneidner (1997a). Copyright 1997 by the American Physical Society.

does not exist. However, as already stated, the transition usually takes place over a finite temperature/field range. Figure 1.7 comes from the first report of giant MCE (Pecharsky and Gschneidner, 1997a) and shows isothermal magnetisation data and the corresponding isothermal entropy changes calculated using the Maxwell relation. As can be seen, the change in magnetisation due to the first order magnetostructural transition of $Gd_5Si_2Ge_2$ is not step-like.

Giguere et al. (1999) disputed the use of Maxwell equation based on the discrepancies between the adiabatic temperature change measured directly and inferred from isothermal entropy change calculated using Maxwell relation; claiming that Maxwell relation overestimates the entropy change. According to the authors, the entropy change cannot

be calculated using Maxwell equation because it is not a magnetic entropy change, and $M(T)$ or $M(H)$ is not a continuous, derivable function. They proposed the use of Clausius-Clapeyron equation instead

$$\left|\frac{\Delta T_c}{\Delta H}\right| = \left|\frac{\Delta M}{\Delta S}\right| = const, \tag{1.14}$$

where ΔT_c is the is the shift of critical temperature for a certain change in field, ΔH. The entropy change depends also on the change in magnetisation at the transition, ΔM. The left-hand side is essentially the slope of the phase line of the transition in an H-T phase diagram. Most often the equation can be found in the form

$$\Delta S = -\Delta M \frac{dH_c}{dT}, \tag{1.15}$$

where H_c is the critical field of the transition in an isothermal measurement (Balli et al., 2009; Gama et al., 2009; Cui et al., 2010).

In a comment, Sun et al. (2000) have shown that the Clausius-Clapeyron equation is only a special case of Maxwell relation. While Clausius-Clapeyron equation calculates the entropy change from the first order change of the magnetic order only, Maxwell relation includes the contribution from changes in the order parameter as well. Further discussion on the topic was sparked by the controversial discovery of 'colossal' MCE in MnAs and it will be covered in section 4.1.

As stated in the beginning of the section, the irreversibility of the first order phase transitions is usually considered to have a negligible effect on thermodynamics of the MCE. Even though this may be the case with magnetoelastic transitions (e.g. Mn_3GaC (Tohei et al., 2003), $MnFeP_{0.45}As_{0.55}$ (Tegus et al., 2002)), there is often significant field/temperature hysteresis associated with magnetostructural transitions (e.g. MnAs (Wada and Tanabe, 2001), also the case of $Gd_5Si_2Ge_2$, as can be seen in figure 1.7. An obvious problem with irreversibility of the phase transition is the fact that the entropy change vanishes after one magnetisation cycle unless the sample is treated thermally. This can make it impossible to use such a material in a refrigeration cycle.

Furthermore, as a result of hysteretic magnetisation cycle, there is a net magnetic work

applied on the magnetic material, which should be proportional to the area of the hysteresis loop, $\oint HdM$ (Tishin and Spichkin, 2003). This work is dissipated as a heat which leads to an additional rise in temperature. When the sample is expected to cool, the non-reversible effects can decrease the sample cooling.

These effects are not very often considered in the literature. If they are, the hysteresis is usually accounted for by calculating an average heat dissipated in the isothermal magnetisation loops, using the magnetic work integral. This is then deducted from the total refrigerant capacity (*RC*) of the material. *RC* is most often calculated as the integral of isothermal entropy change with respect to temperature in the limits of full-width-half-maximum of the entropy change peak. The limits are assumed to be the temperatures of the hot and cold reservoirs. See, for example, Pathak et al. (2007), Hernando et al. (2009), Rao et al. (2009).

Throughout this thesis the indirect estimates from Maxwell relation are compared with a measurement in microcalorimeter. The issues related to the use of Maxwell relation are examined but also the dissipation of magnetic work is studied in the microcalorimeter. The description of the experimetal apparatus follows in the next chapter.

Chapter 2

Experimental Methods

*This chapter describes the two main experimental techniques employed in this thesis. While the **vibrating sample magnetometry** is one of the most strongly established techniques within the magnetism community and beyond, the **microcalorimeter** is a rather novel instrument offering a unique perspective on the magnetocaloric effect. An intensive use of the microcalorimeter throughout the course of the PhD has led to a thorough understanding of the way it functions and of its current limitations in terms of measurement error. This allowed me to propose several improvements, which, although not utilised in the measurements performed here, can help to improve the accuracy and precision of the future measurements.*

2.1 Vibrating Sample Magnetometer

Vibrating sample magnetometer (VSM) was originally invented by Simon Foner (Foner, 1959). The basic concept relies on a detection of magnetic flux changes caused by the sample movement. For this purpose an arrangement of pickup coils is placed in the vicinity of the vibrating sample. As given by Faraday's law, the changes in magnetic flux through the pickup coils induce a voltage in the coils. This voltage signal can be detected at the frequency of the vibration by a lock-in method.

The magnetisation measurements presented here were performed using a VSM Option

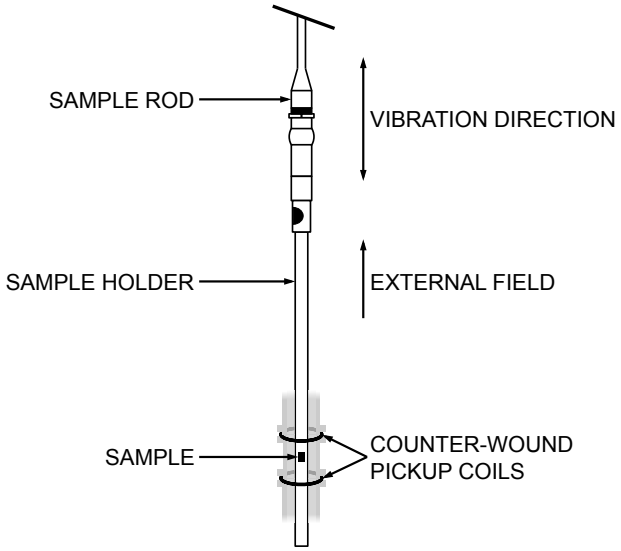


Figure 2.1 PPMS VSM schematic, after Quantum Design (2008).

for the Physical Property Measurement System (PPMS) by Quantum Design. The PPMS uses a superconducting electromagnet to provide an external magnetic field up to 9 T. The sample temperature can be varied between 1.9 K and 350 K.

The VSM is set up in a longitudinal configuration, i.e. the sample vibration, external field and moment detection are all along the vertical axis (figure 2.1). The sample is suspended from a motor head on a vertical sample rod. The motor oscillates the sample sinusoidally with a typical amplitude of 1-3 mm and at a frequency of 40 Hz. There are two pickup coils with their central axes aligned with the sample oscillation and the sample oscillates around the midpoint between the coils. Thus, the sample always travels away from one coil (magnetic flux decreases) and towards the other (magnetic flux increases). In order to add the voltage induced in the two coils constructively, they are connected in series but wound in opposite senses. In addition, this arrangement rejects voltages induced by the changes in external magnetic field, which allows for continuous sweeping of magnetic field during the measurement. The response of the pickup coils is calibrated against a Palladium reference. The system can thus resolve magnetisation changes of less than 10^{-6} emu at a sampling rate of 1 Hz (Quantum Design, 2008).

2.2 Microcalorimeter Overview

The microcalorimeter was originally developed by Y.V. Bugoslavsky and A.A. Minakov to measure the heat capacity of extremely small samples as a function of temperature and magnetic field (Minakov et al., 2005). The setup uses a lock-in technique to measure the temperature fluctuations of the sample in response to a modulated heat influx. As a result, it cannot measure irreversible effects such as the release of latent heat at a first order phase transition. To recover the missing thermodynamic information, the probe was later adapted to operate in a passive, quasi-adiabatic mode (Miyoshi et al., 2008). The two modes of operation now form a unique setup enabling a separate measurement of the heat capacity (related to continuous changes in entropy) and the latent heat (associated with discontinuities in entropy). This in turn allows us to separate the first and higher order contributions to entropy changes.

The experiment utilises a commercially available thermal conductivity gauge for gas, TCG-3880, from Xensor Integration (van Herwaarden, 2010). The gauge consists of a submicron thick silicon-nitride membrane suspended on a silicon frame of 2.50 $\times$ 3.33 mm, 0.3 mm thick (figure 2.2 a). There is a resistive heater in the centre of the membrane consisting of two stripes of polysilicon (5 $\times$ 100 μm, approximately 50 μm apart). The heater is surrounded by six hot thermopile junctions $\sim$50-100 μm away (figure 2.2 b). The cold thermopile junctions are located on the silicon frame (at bath temperature), thus allowing us to sense the temperature of the central region with respect to the bath.

The sample size should correspond to the area of the heater. A smaller sample size may have a detrimental effect on the thermal contact with the heater, especially considering the geometry of the heating elements. A larger sample size may result in significant thermal gradients within the sample, which may corrupt the model used for heat capacity calculation. This limits the sample size to tiny fragments, with mass typically of the order of μg. Measurement of such a small sample mass can introduce an error in the measurement when specific heat capacity is required.

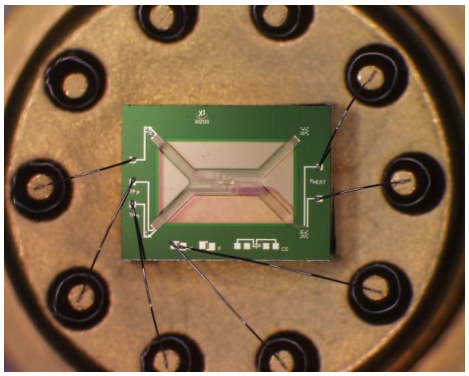
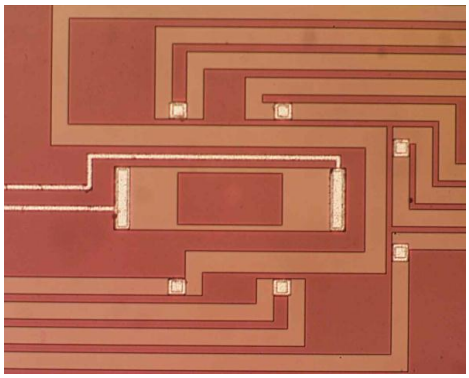
(a)  (b) 

Figure 2.2 The Xensor TCG-3880 gauge (van Herwaarden, 2013). (a) Top-side image of the gauge. (b) Close-up of the central region showing the heater surrounded by hot thermopile junctions (six white dots). Reprinted images with the permission of the rights holder, Xensor Integration.

The sample is usually attached to the membrane using Apiezon N-grease for good thermal contact. Alternatively, GE varnish can be used. The adhesive together with the membrane form addenda in the heat capacity measurement. For absolute values of sample heat capacity, the addenda must be subtracted. This process is another major source of error and it will be discussed later.

The gauge is placed in a vacuum can which can be inserted into an Oxford Instruments VSM cryostat. The cryostat has a superconducting magnet (for fields up to 8 T) and a temperature control using a continuous gas flow system (4.2 K to room temperature). Note that the heat exchange gas used for temperature control does not enter the sample space in the vacuum can but flows around the vacuum can.

2.3 AC Heat Capacity Probe

2.3.1 Principle of Operation

The basic concept of the heat capacity measurement can be described by a simple thermal circuit (figure 2.3). The system is driven by a controlled heat source (the heater), which

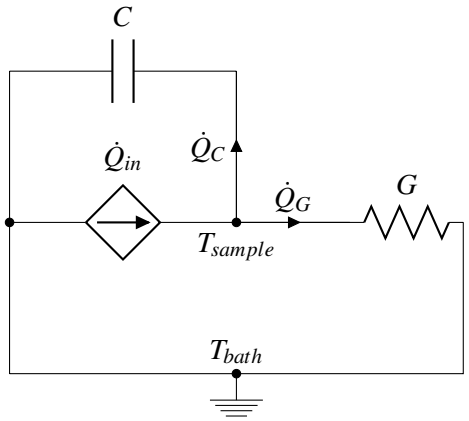


Figure 2.3 Basic thermal circuit representing the heat capacity measurement.

charges a capacitive load C (the heat capacity of the sample and addenda). The capacitor discharges via a thermal resistance connected to the thermal bath at T_{bath}. The thermal resistance is determined by a helium exchange gas which is present in the sample chamber. To a first approximation, we can describe the thermal link by a constant heat exchange parameter G in units of W/K.

Consider the heat flow through junction T_{sample}. The heat flux from the heater ($\dot{Q}_{in}$) may be either absorbed by the capacitive load or dissipated into the thermal bath via the helium exchange gas:

$$\dot{Q}_{in} = \dot{Q}_C + \dot{Q}_G. \tag{2.1}$$

A heat influx of the form $\dot{\mathbf{Q}}_{in} = P_H(1 + e^{i\omega t})$ can be achieved by applying a sinusoidal ac voltage to the heater (bold font is used to denote a complex quantity, italics refer to its magnitude). P_H is then the average power input given by the product of RMS voltage applied to the heater and the RMS current passing through it. Note that the frequency of the power oscillations ($f = \omega/2\pi$) is double the frequency of the voltage oscillations.

The heat flux into the capacitive load is related to the change of its temperature, $\dot{\mathbf{Q}}_C = C\dot{\mathbf{T}}_{sample}$. The heat flux through the thermal resistance is proportional to the temperature difference between the central region of the membrane and the bath, $\dot{\mathbf{Q}}_G = G(\mathbf{T}_{sample} - T_{bath})$.

Thus we arrive at a first order differential equation:

$$P_H(1+e^{i\omega t}) = C\dot{\mathbf{T}}_{sample} + G(\mathbf{T}_{sample} - T_{bath}). \tag{2.2}$$

The complementary solution yields a transient:

$$T_{sample} = Ae^{-\frac{G}{C}t}, \tag{2.3}$$

where A is a constant of integration dependent on the boundary conditions. The transient can be used to evaluate the intrinsic response time (or time constant) of the experiment. For the measurement of heat capacity, the stationary solution given by the particular integral is of interest. It can be obtained by using a trial solution,

$$\mathbf{T}_{sample} = T_{bath} + T_{dc} + \mathbf{T}_{ac}e^{i\omega t}, \tag{2.4}$$

yielding

$$T_{dc} = \frac{P_H}{G} \tag{2.5}$$

and

$$\mathbf{T}_{ac} = \frac{P_H}{G + i\omega C}. \tag{2.6}$$

The complex nature of the amplitude implies that the temperature oscillations acquire a phase lag with respect to the driving power input. This is due to the capacitive load on the membrane, which is linked to the imaginary component of the amplitude. The temperature oscillations can be measured via the thermopile, with the thermopile voltage given by:

$$\mathbf{V}_{th} = K(\mathbf{T}_{hot} - T_{cold}) + V_{offset}, \tag{2.7}$$

where K is the Seebeck coefficient; $\mathbf{T}_{hot}$ and T_{cold} are the temperatures of the hot and cold thermopile junctions, respectively. Assuming that the hot junction is at the sample temperature and cold junction is at the bath temperature, we get:

$$\mathbf{V}_{th} = V_{offset} + \frac{KP_H}{G} + \frac{KP_H}{G + i\omega C}e^{i\omega t} = V_{th,dc} + V_{th,ac}e^{i(\omega t+\phi)}, \tag{2.8}$$

where $V_{th,dc}$ is the dc offset of thermopile voltage, $V_{th,ac}$ is the amplitude of the ac component and ϕ is the phase of the ac signal with respect to the heater power. The latter two can be measured with great precision using a lock-in amplifier. By comparing the time dependent terms:

$$V_{th,ac}(\cos\phi + i\sin\phi) = \frac{KP_H}{G + i\omega C}. \tag{2.9}$$

Heat capacity can be isolated from the imaginary part:

$$C = \frac{KP_H}{\omega V_{th,ac}} \sin(-\phi), \tag{2.10}$$

where P_H, ω, $V_{th,ac}$ and ϕ can be controlled/measured directly during the experiment. The Seebeck coefficient, K, has to be determined in a separate calibration run (section 2.3.3).

2.3.2 Deviations from Simple Model

The most significant assumptions in the simple model are:

- the description of the helium exchange gas as a simple thermal resistance
- perfect thermal contact between the heater and the sample with no internal temperature gradients
- negligible thermal conductance through the membrane
- perfect thermal contact between the sample and the hot thermopile junctions

All of the above are considered in greater detail in Minakov et al. (2005) and the findings are summarised here.

Thermal link to bath via helium exchange gas

The thermal link can be described more accurately by considering the propagation of a spherical thermal wave from a central heated region with radius r_0 (heater and the sample) through a gas with a wavenumber $\mathbf{k}_g$. The wavenumber is given by the dispersion law for thermal waves: $\mathbf{k}_g^2 = i\omega c_g/\lambda_g$, where c_g is the specific heat capacity per unit volume and λ_g

is the thermal conductivity of the gas. With these considerations, the complex amplitude of the thermal oscillations of the sample becomes:

$$\mathbf{T}_{ac} = \frac{P_H}{G(1+\mathbf{k}_g r_0) + i\omega C}, \tag{2.11}$$

where $G = 4\pi r_0 \lambda_g$. Note that the dc temperature offset (T_{dc}) remains unaffected.

In general, **k** can have two values — the positive and negative root. Here the positive root describes the thermal wave propagating away from the heater, while the negative root corresponds to the reflected wave, which may be neglected. Thus:

$$\mathbf{k} = (1+i)\sqrt{\frac{\omega c}{2\lambda}}. \tag{2.12}$$

A characteristic thermal exchange length may be defined for the helium gas, $l_g = \sqrt{2\lambda_g/\omega c_g}$, and equation 2.11 may be rewritten as:

$$\mathbf{T}_{ac} = \frac{P_H}{G + G\frac{r_0}{l_g} + iG\frac{r_0}{l_g} + i\omega C}. \tag{2.13}$$

Thus the heat exchange coefficient may "contaminate" the imaginary part of the oscillation amplitude which is used to measure the capacitive load on the gauge. This, however, is negligible if $r_0 \ll l_g$. r_0 is physically limited by the size of the heater, thus $r_0 \sim 50\ \mu$m and the sample size should not be larger than this. Since l_g is frequency dependent, it can be tuned by changing the operating frequency. Typical values of the thermal length based on thermal properties of helium gas are shown in Table 2.1. At the usual operating frequency (10 Hz) the thermal length is significantly larger than r_0 near room temperature but reduces with decreasing temperature. This can be somewhat slowed down by filling the vacuum can with helium gas at room temperature and sealing it before cooling to lower temperatures, which is the usual operating procedure.

Note, however, that the description is truly valid only for l_g smaller than 0.5 mm, which is the minimal distance from the centre of the membrane to the metallic chip housing. For larger thermal lengths the thermal wave should be affected by the chip housing. A more detailed consideration of this shall be a subject of future work.

Table 2.1 Typical values of l_g estimated from thermal properties of helium gas. Atmospheric pressure values at 0.1 Hz and 100 Hz are reproduced from Minakov et al. (2005). The constant volume values are calculated assuming atmospheric pressure at 300 K and pressure-independent thermal conductivity.

	l_g [mm]					
Temperature [K]	atmospheric pressure			constant volume		
	f = 0.1 Hz	10 Hz	100 Hz	0.1 Hz	10 Hz	100 Hz
10	1.4	0.14	0.04	7.7	0.77	0.22
20	2.4	0.24	0.08	9.3	0.93	0.31
50	5	0.5	0.16	12.2	1.12	0.39
100	9	0.9	0.3	15.6	1.56	0.52
300	23	2.3	0.7	23	2.3	0.7

Thermal oscillations within the sample

Minakov et al. (2005) consider also the thermal oscillations within the membrane/Apiezon grease/sample stack. A thermal wave along the direction perpendicular to the membrane is considered assuming negligible radial temperature gradients and good and stable thermal contacts between the layers. Each layer is characterised by a wave number, $\mathbf{k}_n^2 = i\omega c_n/\lambda_n$. The product of the wave number and the layer thickness, d_n, forms a dimensionless effective thermal thickness of the layer, $\alpha_n = \mathbf{k}_n d_n$.

If $\alpha_n \ll 1$, there is no difference in the phase and amplitude of thermal oscillations between the opposite sides of the layer. It has been shown (Minakov et al., 2005) that this is the case for the membrane and a thin layer of Apiezon grease (5 μm thickness). Thus, no additional correction should be necessary to their heat capacity contribution, C_0 and C_A, respectively.

If, however, the thermal thickness of the sample, $\alpha_\mathbf{s}$, is non-negligible, there is a factor

$\tanh(\alpha_s)/\alpha_\mathbf{s}$ in the expression for the sample's effective heat capacity. The total effective heat capacity for temperature oscillations at the sample surface closest to the membrane (e.g. in equation 2.13) is then:

$$C = C_0 + C_A + C_s \frac{\tanh(\alpha_s)}{\alpha_s}. \tag{2.14}$$

Membrane contribution

Although the radial temperature gradients may be negligible for Apiezon grease and the sample (their radial size should be comparable with the heater region), the membrane spreads beyond the heater and therefore the thermal wave propagates through it radially (similarly to the propagation in helium exchange gas). Note that while globally the heat transfer from the central region occurs predominantly through the helium exchange gas, the temperature profile across the membrane is determined mostly by the conduction through the membrane itself. Thus it is dependent on the membrane wave number, $\mathbf{k}_0 = \sqrt{i\omega c_0/\lambda_0}$.

In a correction similar to the addition to the heat exchange coefficient (the difference between $\mathbf{T}_{ac}$ in equations 2.6 and 2.11), there is an additional contribution from the membrane:

$$i\omega\mathbf{C}_{0,eff} = i\omega C_0 + G_0\mathbf{k}_0 r_0 = i\omega C_0 + G_0 r_0 \sqrt{\frac{i\omega c_0}{\lambda_0}}. \tag{2.15}$$

Since ω is the only variable, a parameter ω_0 may be introduced, simplifying the above to:

$$\mathbf{C}_{0,eff} = C_0 \left(1 + \sqrt{\frac{\omega_0}{i\omega}}\right). \tag{2.16}$$

Note that both, ω_0 and C_0, are physically related to the combination of the membrane heat capacity and thermal conductivity. They act as formal parameters and can be measured for an empty gauge.

Thermometer lag

The final major correction to the simple model stems from the spatial separation between the heater (sample) and the hot thermopile junction, $d_0 \sim 50\ \mu$m. The heat transfer to the

hot thermopile junction is dominated by the membrane with a wave number $\mathbf{k}_0$, yielding an effective thermal distance $\alpha_0 = d_0\mathbf{k}_0$. The thermal oscillations at the hot junction should be:

$$\mathbf{T}_{hot,ac} = \frac{\mathbf{T}_{ac}}{\cosh\alpha_0}. \tag{2.17}$$

Overall considerations

Taking into account all of the corrections, the amplitude of thermopile voltage oscillations becomes:

$$\mathbf{V}_{th,ac} = \frac{KP_H}{\cosh\alpha_0\left(G(1+\mathbf{k}_g r_0) + i\omega C_0\left(1+\sqrt{\frac{\omega_0}{i\omega}}\right) + i\omega C_A + i\omega C_s\frac{\tanh\alpha_s}{\alpha_s}\right)}. \tag{2.18}$$

The sample heat capacity is no longer simply related to the imaginary part of the thermal oscillations. Nevertheless, the effect of the sample thermal thickness is usually negligible for samples with high thermal conductivity, which is the case in this work as only metallic samples are studied.

The membrane parameters, α_0, C_0 and ω_0, can be determined from the frequency dependence of an empty gauge measurement. Minakov et al. (2005) showed that for operating frequencies of up to 100 Hz the effect of thermometer lag is insignificant (i.e. the value of the hyperbolic cosine in equation 2.17 is real and close to 1 to within 1 %).

Without the effect of thermometer lag and thermal thickness of the sample, equation 2.18 may be simplified and rearranged to the form:

$$G + G\mathbf{k}_g r_0 + C_0\sqrt{i\omega\omega_0} + i\omega\left(C_0 + C_A + C_s\right) = \frac{KP_H}{V_{th,ac}}\left(\cos\phi + i\sin-\phi\right), \tag{2.19}$$

which is very close to the simple model (equation 2.9) with the sample heat capacity measured fully by the imaginary part of this equation.

For the measurement of the absolute heat capacity of the sample, other contributions to the imaginary part must be subtracted. C_A can be measured separately. The Apiezon N-grease undergoes a glass transition at ~ 230 K with a characteristic change in heat capacity. The magnitude of this change can be used to estimate the actual amount of grease during

a sample measurement (Morrison, 2010). Unfortunately, this is not possible if GE varnish is used as the adhesive.

The removal of the membrane contribution (which also has to be done for the grease-only measurement) also needs to take into account its frequency dependence (due to the $C_0\sqrt{i\omega\omega_0}$ term in equation 2.19). As already mentioned, the parameters C_0 and ω_0 can be determined from the empty gauge measurement. Nevertheless, an accurate determination of the ω_0 parameter may be affected by the $G\mathbf{k}_g r_0$ term which has the same frequency dependence (effectively adding to ω_0). Since the initial helium exchange gas pressure is not strictly controlled, the $G\mathbf{k}_g r_0$ term (and the effective ω_0) may differ between measurements as the vacuum can has to be refilled every time the gauge is manipulated.

In order to evaluate the significance of the $C_0\sqrt{i\omega\omega_0}$ and $G\mathbf{k}_g r_0$ terms (and in fact any other deviation from the simple model), a so-called G_{ratio} concept has been developed.

G can be calculated independently from the dc temperature offset of the central heated region. From equation 2.8:

$$V_{th,dc} = V_{offset} + \frac{KP_H}{G}, \tag{2.20}$$

where V_{offset} is the voltage measured across the thermopile when there is no temperature difference between the hot and cold junctions. It can be compensated for by measuring V_{th} at $P_H = 0$. Thus, we may define a "dc heat exchange coefficient":

$$G_{dc} = \frac{KP_H}{V_{th,dc} - V_{th}(P_H = 0)}. \tag{2.21}$$

An "ac heat exchange coefficient" may be derived from the real part of equation 2.19:

$$G_{ac} = \frac{KP_H}{V_{th,ac}}\cos\phi = G_{dc} + \Re(G\mathbf{k}_g r_0 + C_0\sqrt{i\omega\omega_0}). \tag{2.22}$$

While G_{ac} contains the heat exchange coefficient, it also includes the real part of $C_0\sqrt{i\omega\omega_0}$ and $G\mathbf{k}_g r_0$ (which both have an equal real and imaginary part). Thus we may define a G_{ratio}:

$$G_{ratio} = \frac{G_{ac}}{G_{dc}} = \frac{V_{th,dc} - V_{th}(P_H = 0)}{V_{th,ac}}\cos\phi. \tag{2.23}$$

The magnitude of the G_{ratio} can be monitored when setting up the measurement. The operating frequency can be adjusted to yield $G_{ratio} \approx 1$. At that point the $C_0\sqrt{i\omega\omega_0}$ and $G\mathbf{k}_g r_0$ terms are minimised relative to G (minimising $G\mathbf{k}_g r_0$ effectively ensures that the exchange gas thermal length is larger than r_0). Since both these terms are proportional to $\sqrt{\omega}$, G_{ratio} should get closer to one as the operating frequency is reduced, which it does in practice.

The use of G_{ratio} leads to the usual operating frequency of 10 Hz. At this frequency G_{ratio} is typically ~ 0.9. Reducing the frequency any further, however, requires the use of prohibitively large time constants on the lock-in amplifier.

Unfortunately, the reasoning behind the G_{ratio} is partially flawed with respect to optimising the measurement frequency for C_s. Consider the imaginary part of equation 2.19:

$$\omega(C_0 + C_A + C_s) + \Im(G\mathbf{k}_g r_0 + C_0\sqrt{i\omega\omega_0}) = \frac{KP_H}{V_{th,ac}} \sin -\phi. \tag{2.24}$$

To clearly illustrate the frequency dependence of each term, the wave number definition can be used (equation 2.12). The above can then be rewritten:

$$\omega\left(C_0 + C_A + C_s + Gr_0\sqrt{\frac{c_g}{2\lambda_g\omega}} + C_0\sqrt{\frac{\omega_0}{2\omega}}\right) = \frac{KP_H}{V_{th,ac}} \sin(-\phi). \tag{2.25}$$

It can be seen that the effective addenda to C_s coming from the $C_0\sqrt{i\omega\omega_0}$ and $G\mathbf{k}_g r_0$ terms actually increases with decreasing ω. This is because the contribution of C_s to the imaginary part changes linearly with ω whereas the $C_0\sqrt{i\omega\omega_0}$ and $G\mathbf{k}_g r_0$ terms are proportional to $\sqrt{\omega}$ and reduce more slowly with decreasing ω. Thus, although the real part of these terms becomes insignificant relative to G (frequency independent), their imaginary contribution increases relative to C_s.

Hence, rather than ensuring that the $G\mathbf{k}_g r_0$ term is negligible by increasing the thermal length, l_g, via reducing the operating frequency, one may be more successful by controlling the exchange gas pressure. In fact, the current practice of thermal length optimisation by frequency reduction makes the effective heat capacity addenda more sensitive to the sample size and shape (the effective r_0) and to the exchange gas pressure, which, at the

moment, is not controlled and may vary from measurement to measurement. This may compromise any attempt to remove the addenda accurately using an empty gauge measurement.

While the exchange gas pressure can potentially be controlled for a reproducible effect, the effective r_0 is bound to be different between the empty gauge and a sample measurement. Thus, it may be more accurate to determine the $C_0\sqrt{i\omega\omega_0}$ and $G\mathbf{k}_g r_0$ terms (or, more correctly their sum) from the frequency dependence of the sample measurement rather than the empty gauge measurement. This could be done during a calibration of the Seebeck coefficient, which is discussed in the next section.

Note, however, that for the purposes of this thesis, we are concerned only with the field-induced changes in heat capacity rather than the absolute heat capacity of the sample. Provided that C_s is the only field-dependent variable on the left-hand side of equation 2.19, addenda removal is not necessary. Thus, the use of the simple model and equation 2.10 is sufficient for evaluation of field-induced heat capacity changes.

2.3.3 Seebeck Coefficient Calibration

The Seebeck coefficient, which is necessary to convert the thermopile voltage to temperature difference, is determined in a separate calibration run. It requires an independent measure of temperature of the central region of the membrane. For this purpose the temperature dependence of the heater resistance is utilised.

During the calibration run, the amplitude of the ac voltage signal applied to the heater is ramped while the heater voltage ($V_{H,rms}$), current ($I_{H,rms}$) and the dc offset of the thermopile voltage ($V_{th,dc}$) are measured. Thus we can plot the (average) heater resistance ($R_H = V_{H,rms}/I_{H,rms}$) as a function of heater power (figure 2.4 a). The average temperature of the membrane central region with respect to the bath increases linearly with heater power (equation 2.5) and a corresponding increase in the heater resistance is observed. By extrapolation to zero heater power, one can obtain the heater resistance at the bath temperature. In order to obtain the temperature dependence of the heater resistance (figure 2.4 b), the

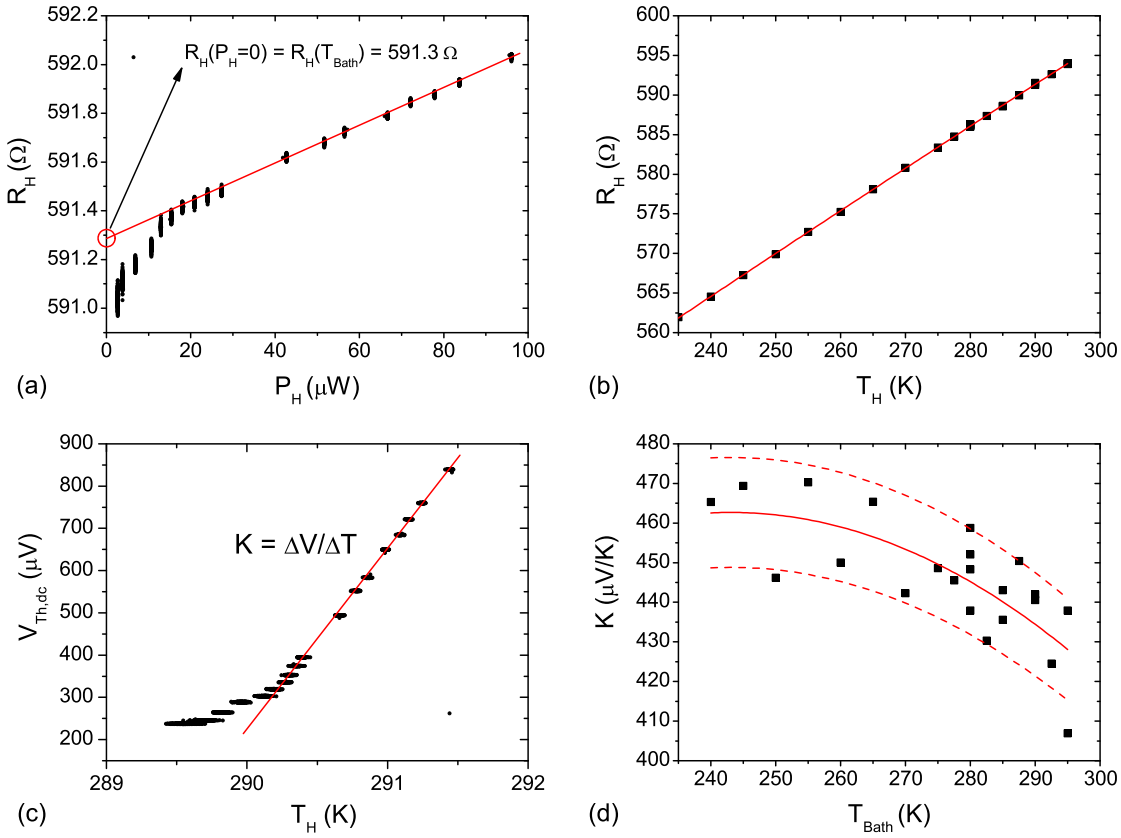


Figure 2.4 Plots for Seebeck coefficient calibration. (a) R_H as a function of P_H. Extrapolation to $P_H = 0$ gives R_H at T_{bath} since at $P_H = 0$, $T_H = T_{Bath}$ (low power data points are disregarded as they are affected by DAQ resolution limit). (b) Temperature dependence of R_H as given by $R_H(P_H = 0)$ at different bath temperatures. (c) $V_{th,dc}$ as a function of T_H yields the Seebeck coefficient. (d) Seebeck coefficient as a function of bath temperature with a polynomial fit and 3% error bands.

procedure is repeated at different bath temperatures and the data points are fitted with a polynomial function (up to second order).

The measured heater resistance can then be converted to heater temperature (T_H). Hence, $V_{th,dc}$ can be plotted as a function of T_H (figure 2.4 c). Assuming that the heater temperature is the same as the temperature of the hot thermopile junctions (T_{hot}), it follows from equation 2.7 that the Seebeck coefficient is given by the slope of the plot. Again, by repeating the procedure at the different bath temperatures, the temperature dependence of the Seebeck coefficient is obtained and fitted with a polynomial function (figure 2.4 d).

It is worth noting that, due to the spatial separation between the heater and the hot thermopile junctions, their temperature is not the same. Thus, an effective Seebeck coefficient (between the heater and cold thermopile junctions) is measured rather than the actual Seebeck coefficient (between the hot and the cold junctions). While the latter should be fully determined by the properties of the thermopile, the former is a subject to the actual temperature profile across the membrane. This varies with the sample size, position, as well as operating frequency. Thus, the calibration has to be repeated for every measurement and it should be performed at the operating frequency of the measurement.

2.3.4 Measurement Setup

The experimental setup for the heat capacity measurement is shown in figure 2.5. A Stanford Research System Digital Lock-in Amplifier (LIA) SR830 is used. The gauge heater is driven directly by the LIA sine output. As already mentioned, the drive frequency is half the frequency of the power oscillations and the corresponding temperature oscillations. Hence, the LIA has to be detecting the 2nd harmonic of the drive signal.

If the drive signal is of the form $\sin(\omega t/2)$, the power oscillations from the heater are of the form $\frac{1}{2}(1+\sin(\omega t-\frac{\pi}{2}))$. Nevertheless, the sine wave used for the phase-sensitive detection is simply the drive signal with double the frequency, i.e. $\sin(\omega t)$. As a result, a signal which is in phase with the power oscillations leads the LIA reference by $\pi/2$, which is what the LIA measures. Since we are interested in the phase of the thermopile

oscillations with respect to the power oscillations (ϕ), this additional phase difference has to be compensated for. Thus, if the output of the LIA (traditionally in degrees) is θ, then:

$$\phi = (\theta - 90)\frac{\pi}{180}. \tag{2.26}$$

Also, the LIA always reports the rms magnitude of an ac signal, $R_{rms} = \sqrt{X_{rms}^2 + Y_{rms}^2}$. Thus:

$$V_{th,ac} = \sqrt{2}R_{rms}. \tag{2.27}$$

There is currently a capacitor across the thermopile output ($C_{filter} = 22$ nF). Together with the thermopile resistance, R_{th}, it acts as a low-pass filter to reduce high-frequency noise. Its impact on the measurement will be discussed in greater detail in the next section.

In order to measure the heater power, P_H, we measure the voltage across the heater, V_H, using a DAQ card. The heater current, I_H, is calculated from the voltage measured across a shunt resistor, $R_{shunt} \approx 6750$ kΩ. These are also used to determine the heater resistance, R_H, which is required in the Seebeck coefficient calibration.

Finally, the dc offset of the thermopile voltage ($V_{th,dc}$), which is used in the calibration as well as G_{ratio} calculation, is also measured using the DAQ card. Nevertheless, for this purpose the thermopile signal is pre-amplified with a gain 200, using RS VIP20 pre-amp.

The data acquisition and processing is controlled using LabVIEW (see figure 2.6).

2.3.5 High Accuracy Considerations

Thermopile Voltage Transfer

The thermopile resistance is 52.5 kΩ at room temperature and although it decreases with temperature, it remains large even at much lower temperatures (45.1 kΩ at 100 K). Thus, the thermopile resistance forms a significant source impedance in comparison with the input impedance of the measurement instruments, 1 MΩ and 10 MΩ for the pre-amplifier and LIA, respectively. Since they are connected in parallel, their total input impedance is ~ 0.91 MΩ. Hence, only about 95 % of the thermopile voltage is transferred to the measurement instruments.

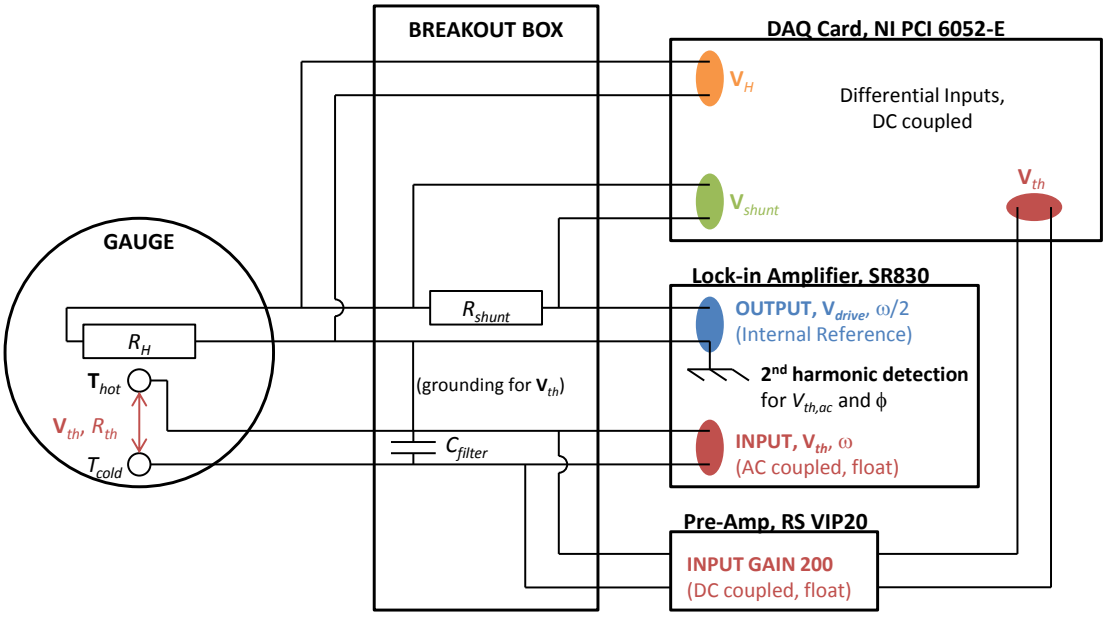


Figure 2.5 Schematic of the experimental setup for heat capacity measurement.

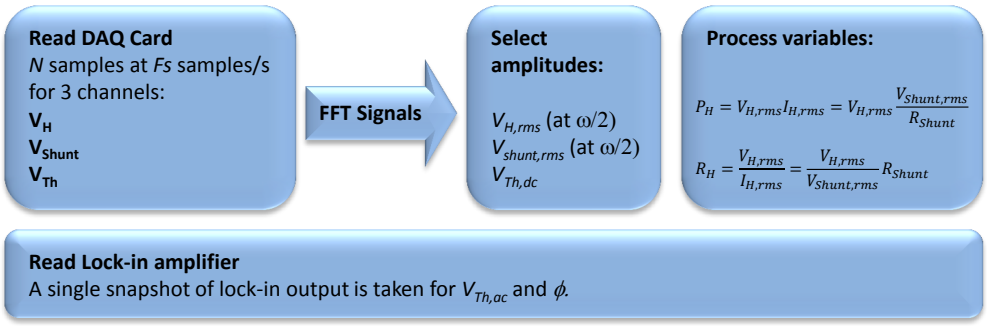


Figure 2.6 Flow chart of the core of the LabVIEW data acquisition loop. The loop clock is determined by the number of samples read on the DAQ card (per loop) and the sampling rate. Only one lock-in reading is taken per loop.

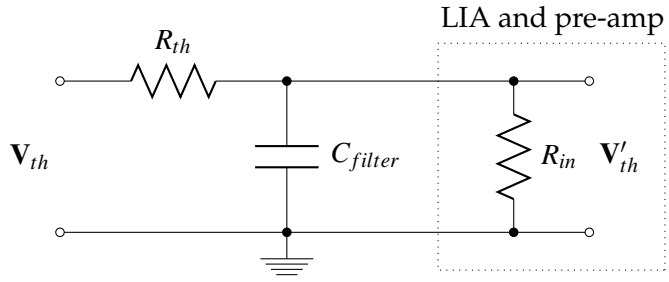


Figure 2.7 Low-pass filter on the thermopile output.

The imperfect voltage transfer can be self-compensated. The $V_{th,ac}$ (used in the heat capacity measurement) and $V_{th,dc}$ (used in the Seebeck coefficient calibration) are both equally affected. As a result, the $K/V_{th,ac}$ ratio, which is the only factor in the heat capacity calculation dependent on the thermopile voltage, is unaffected.

Nevertheless, for this to hold, the measurement setup during the calibration and the actual measurement must remain the same. Note, that the pre-amplifier (figure 2.5) is technically necessary only during the calibration run and for the determination of the G_{ratio} when setting up the measurement. If it were, however, removed for the actual measurement, the voltage transfer would be improved to about 99.5 %. In that case, the measured values of heat capacity would be underestimated by about 4.5 %.

Thermopile Voltage Low-Pass Filter

Figure 2.7 shows the schematic of the effective low-pass filter applied to the thermopile output, including the input impedance of the measurement instruments, R_{in}. Note that a prime is used to denote the physical variables as seen and measured by the instruments. The transfer function for the thermopile voltage is then:

$$\frac{\mathbf{V}'_{th}}{\mathbf{V}_{th}} = \frac{1}{1 + R_{th}/R_{in} + i\omega R_{th} C_{filter}}. \tag{2.28}$$

Note that the real part of the denominator deviates from 1 due to the finite input impedance of the instrumentation. As discussed above, this is compensated for by the measured See-

beck coefficient, which is also affected:

$$K' = \frac{\Delta V'_{th,dc}}{\Delta T} = \frac{\Delta V_{th,dc}}{\Delta T} \cdot \frac{1}{1 + R_{th}/R_{in}} = K \frac{R_{in}}{R_{in} + R_{th}}. \tag{2.29}$$

Thus, the effective transfer function of the low-pass filter is:

$$\frac{\mathbf{T}'}{\mathbf{T}} = \frac{\mathbf{V}'_{th}/K'}{\mathbf{V}_{th}/K} = \frac{1}{1 + i\omega C_{filter} \frac{R_{th}R_{in}}{R_{th}+R_{in}}}. \tag{2.30}$$

The effective time constant of the low-pass filter is then:

$$\tau = C_{filter} \frac{R_{th}R_{in}}{R_{th} + R_{in}}, \tag{2.31}$$

which is aprroximately 1.1 ms at room temperature (cut-off frequency of about 146 Hz). The time constant decreases with measurement temperature due to the thermal dependence of thermopile resistance.

Figure 2.8 shows the gain and phase change due to the filter as a function of operating frequency (at room temperature). At the usual operating frequency of 10 Hz, which is more than a decade below the filter cut-off frequency, the effect on the signal amplitude is negligible (gain ~ 0.998). Nevertheless, the phase lag introduced by the filter ($\sim 3.9^\circ$ at 10 Hz) is still significant and affects the measured values.

The relative impact of the filter phase lag is dependent on the value of the real signal phase lag, due to the capacitive load on the gauge (ϕ). Assuming the simple model (equation 2.10), the erroneous addition to the heat capacity due to an additional phase lag of 3.9° may be expressed as:

$$\frac{\Delta C}{C} = \frac{C' - C}{C} = \frac{\sin(\phi - 3.9^\circ)}{\sin\phi} - 1. \tag{2.32}$$

The G_{ac} given by equation 2.22 is also affected by the additional phase lag:

$$\frac{\Delta G_{ac}}{G_{ac}} = \frac{G'_{ac} - G_{ac}}{G_{ac}} = \frac{\cos(\phi - 3.9^\circ)}{\cos\phi} - 1. \tag{2.33}$$

These two functions are plotted in figure 2.9. Depending on size of the sample, the real phase lag is typically between 30° and 60° at 10 Hz. Thus, due to the filter phase lag the measured heat capacity is artificially increased by 4% to 12%. The measured G_{ac}, however,

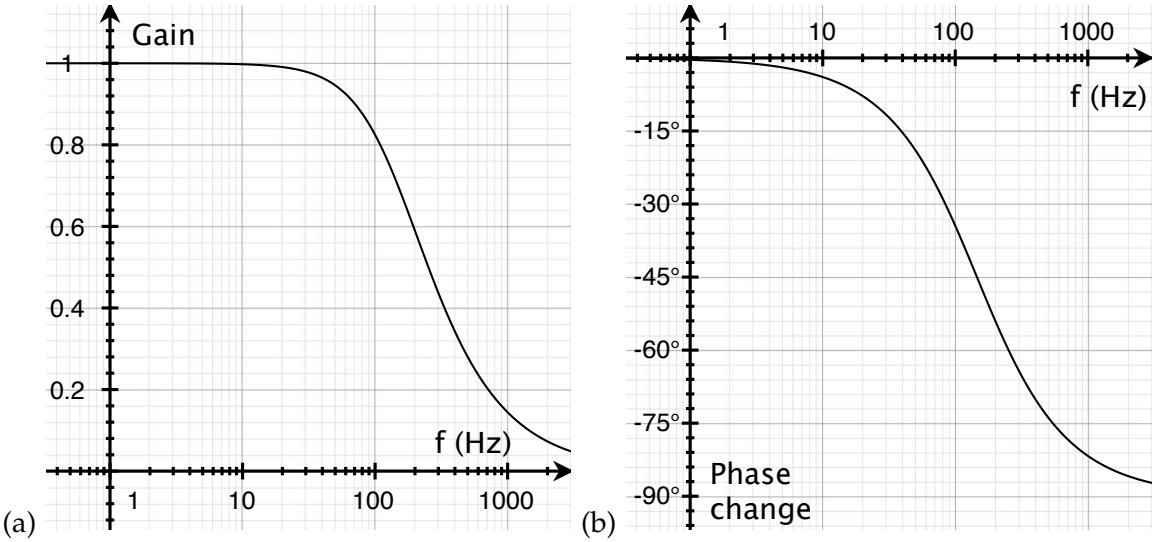


Figure 2.8 Low-pass filter transfer properties at room temperature. Gain (a) and phase change (b) are given by the modulus and argument of the effective transfer function (equation 2.30), respectively. $C_{filter} = 22$ nF, $R_{th} = 52.5$ kΩ, $R_{in} = 909$ kΩ.

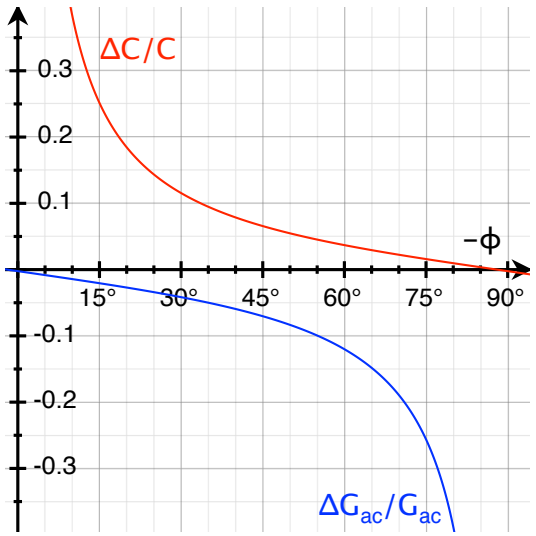


Figure 2.9 Erroneous addition to the measured values of heat capacity (C) and heat exchange coefficient (G_{ac}) due to the low-pass filter as a function of the real signal phase. Operating at 10 Hz, room temperature.

is reduced by 4% to 12%. Note, that this is the reason why we observe $G_{ratio} < 1$, typically ~ 0.9 at 10 Hz).

To see the impact of the filter at any operating frequency, one can apply the filter transfer function to the thermopile signal. By combining equations 2.6, 2.30 and 2.31 we obtain:

$$\frac{\mathbf{V}'_{th,ac}}{K'} = \frac{P_H}{G + i\omega C} \cdot \frac{1}{1 + i\omega\tau} = \frac{P_H}{\underbrace{G - \omega^2\tau C}_{G'_{ac}} + i\omega \underbrace{(C + \tau G)}_{C'}}. \tag{2.34}$$

As is consistent with figure 2.9, the addition to the measured heat capacity depends on the relative magnitude of the heat exchange coefficient (their ratio determines the real phase lag) and vice versa.

The impact of the filter on the measured heat exchange coefficient ($-\omega^2\tau C$) varies with the square of the operating frequency. More importantly, it decreases with decreasing frequency and so the G_{ratio} approaches 1 as the frequency is decreased. Qualitatively similar behaviour was expected from the effect of thermal wave propagation (as discussed in section 2.3.2, equation 2.22 in particular).

Without a full consideration of the filter impact, when observed in practice, the reduction of G_{ratio} with increasing frequency was attributed to the thermal wave propagation. Note, however, that due to the difference in signs, in case of the filter impact the G_{ratio} approaches 1 from below and in case of the thermal wave propagation it approaches 1 from above. The former was observed experimentally. Thus, the low-pass filter was the dominant effect in determining our operating frequency, pushing it towards unnecessarily low values.

For the heat capacity measurement the filter results in an additional addendum of τG. This addendum should vary from measurement to measurement due to the real heat exchange coefficient being dependent on the sample size and shape, as well as the pressure of the helium exchange gas. This may result in errors in the absolute values of heat capacity (which require subtraction of addenda measured in a separate measurement). The effect of the filter can be compensated if all the relevant quantities necessary to determine

the filter time constant are measured (equation 2.31). Of these, R_{th} is most complicated as it is currently not monitored, it changes with temperature and may also vary from gauge to gauge. The accuracy of any compensation for the filter would be subject to how accurately the time constant could be determined. Moreover, the filter compensation would have to be done for each sample measurement as well as addenda measurement, further increasing the overall error introduced by the filter.

As a result, an appropriate future action would seem to be the removal of the filter capacitor, C_{filter}. The dynamic reserve of the LIA as well as the pre-amp (and DAQ) is sufficient to handle the noise levels without the low-pass filter.[1] High-frequency noise can be filtered more easily on the LIA output rather than the input, without distorting the measurement. Note, however, that one needs then to consider the stray (shunt) capacitance of the wiring (instrumentation input), which may be of the order of hundreds of pF and acts the same way as C_{filter}. While it was neglected thus far (being two orders of magnitude smaller than C_{filter}), it may become significant if the filter capacitor is removed and the operating frequency is increased. Nevertheless, while the cut-off frequency of the effective low-pass filter is likely to increase by two orders of magnitude, the operating frequency is still limited to below 100 Hz by the impact of thermometer lag.

For the measurements described here, the measured field-induced heat capacity changes are unaffected by the filter (since τG should be field independent). Thus, the effect of the filter does not need to be explicitly considered.

Sensitivity to R_{shunt}

The shunt resistor (located in a breakout box, figure 2.5) is used to determine the current passing through the heater for heater power and resistance:

$$P_H = V_{H,rms} I_{H,rms} = V_{H,rms} \frac{V_{shunt}}{R_{shunt}} \tag{2.35}$$

[1] Sheilding was improved during rewiring of the probe which may have reduced the overall noise level.

and

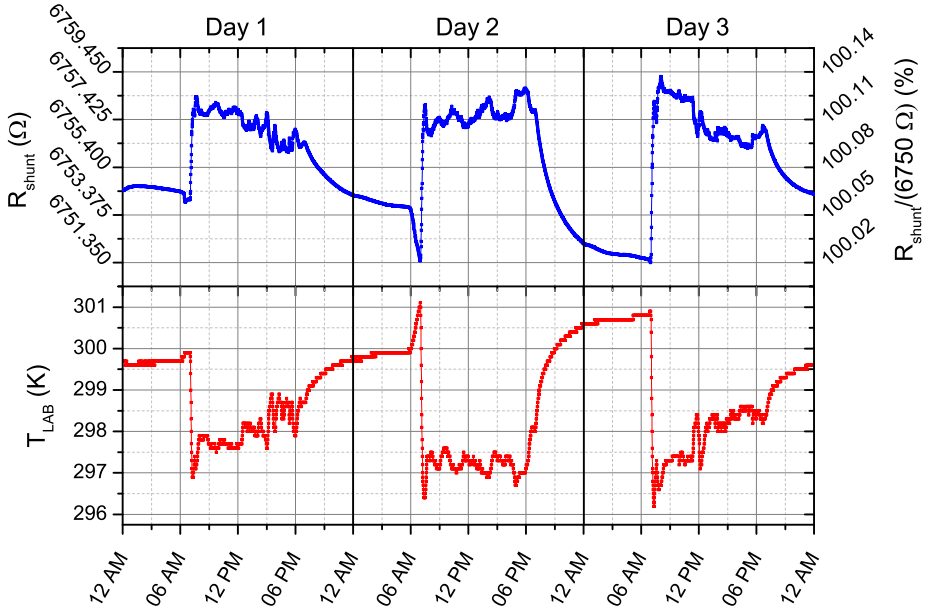
$$R_H = \frac{V_{H,rms}}{I_{H,rms}} = V_{H,rms}\frac{R_{shunt}}{V_{shunt}}. \tag{2.36}$$

The shunt resistor currently used is NEOHM type ROX1S with a nominal resistance of 6.8 kΩ, 5% tolerance and a maximum temperature coefficient of resistance (TCR) ±300 ppm/K (0.03% or 2 Ω per K).

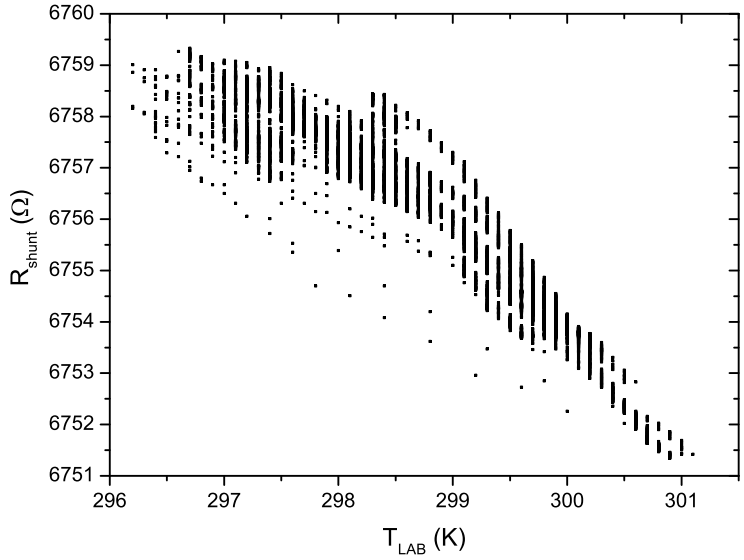
At room temperature the resistance of the shunt resistor (as measured using a digital multimeter) is ∼ 6750 kΩ. This value is assumed to be constant and it is used throughout the measurement and calibration procedure. Nevertheless, with a rather large TCR, this may not be the case. To investigate the impact of temperature fluctuations in the lab, the shunt resistance was measured in the same setup which is used to measure the heater resistance, however, a secondary high precision resistor was used as a shunt (402 Ω, 0.1% tolerance, maximum TCR of 15 ppm/K). The shunt resistance measured as a function of time over 3 days is plotted in figure 2.10 a. The lab temperature was also measured using a Pt1000 sensor connected to Oxford Instruments ITC4 controller. The resistance changes are clearly correlated with temperature fluctuations in the lab and they are consistent with the quoted TCR (figure 2.10 b).

It can be seen that the shunt resistance appears to deviate by up to $(0.14 \pm 0.06)\%$ from the assumed value (6750 kΩ). More importantly, it fluctuates by as much as $(0.1200 \pm 0.0002)\%$ throughout a day.[2] The largest changes are observed at 7am and 8pm every day, which is when the lab temperature control is switched on and off, respectively. This uncertainty in R_{shunt} may affect two variables that are used in the heat capacity calculation (equation 2.10), P_H and K, both of which are simple factors in the heat capacity formula. Thus, a relative error in either of the two translates directly into relative error in the heat capacity.

[2]The error in the deviation from an absolute value is determined by the relative accuracy of the DAQ measurement (∼ 0.04%, a ratio of two DAQ measurements is used to determine R_{shunt}). The error in fluctuations, however, is given by the measurement precision determined by noise and quantisation. The precision is enhanced vastly by averaging (in this measurement an FFT is performed on a waveform of 100 000 points).



(a)



(b)

Figure 2.10 (a) R_{shunt} and lab temperature as a function of time. (b) R_{shunt} as a function of lab temperature shows a clear correlation equivalent to a TCR of approximately -250 ppm/K.

P_H is measured directly during the measurement. Since R_{shunt} is a simple factor in the determination of the heater power, any relative deviation from the assumed value of 6750 Ω results in the same relative error in P_H and consequently also in heat capacity (and heat capacity changes). The above measurement shows that this error is rather small (below 0.2%). It may, however, become important for the accuracy of very small field-induced heat capacity changes if R_{shunt} drifts significantly during the field ramp. For instance, a 0.03% drift in R_{shunt} could result in a 3% error in a 1% heat capacity change.

The impact of R_{shunt} error on the Seebeck coefficient, K, which is determined in the calibration procedure, is somewhat more complex. Throughout the procedure, the R_{shunt} has significant impact only on R_H (a linear factor within). Since R_H is used only as a measure of local temperature change, a constant relative error in R_{shunt} would have no effect on the Seebeck coefficient, whereas a time varying error would. Constant error acts as a scaling factor in the determined $R_H(T)$ (figure 2.4 b). This scaling factor is cancelled when (the scaled) R_H is converted to T_H (figure 2.4 c).

Nevertheless, R_{shunt} does fluctuate with time. On the timescale of the driving amplitude ramp (around 10 minutes), the R_{shunt} fluctuations should be mostly negligible (except perhaps for the times when the lab temperature control is switched on/off), but the ramps at different bath temperatures are typically an hour apart (due to the settling and equilibration time at a new temperature setpoint). During this time the R_{shunt} could drift by 0.03%. As can be seen in figure 2.4 b, the $R_H(T)$ has a typical slope of 0.1% per K. For a pair of calibration bath temperatures 5 K apart, the drift of R_{shunt} (and consequently R_H) would affect the slope of $R_H(T)$ by 6%. It is this slope that determines the conversion of ΔR_H to ΔT_H, which then determines the measured Seebeck coefficient ($K = \Delta V_{th,dc}/\Delta T_H$). Thus, a drift in R_{shunt} as small as 0.03% may result in a Seebeck coefficient error of 6%.

This error may be somewhat reduced by the procedure of fitting $R_H(T)$ with a polynomial. The slope at any temperature is then effectively averaged over several neighbouring data points and corresponds to an average R_{shunt} over that time period. The Seebeck coefficient error at any given temperature is then given by the deviation from this average

R_{shunt} at any particular temperature. Thus, in figure 2.4 d we observe fluctuations in K of about 3% rather than 6%. Fitting of the Seebeck coefficients obtained at different temperatures with another polynomial function further averages over multiple data points and compensates for R_{shunt} fluctuations. Nevertheless, such fitting would not compensate for a monotonous drift in R_{shunt}, such as is observed at night-time after the laboratory temperature control is switched off. In that case, the slope of R_{shunt} with time should systematically affect the apparent slope of R_H with T_{bath} (provided that the calibration amplitude ramp is done at gradually increasing or decreasing bath temperatures).

Another potential source of a systematic error could be a finite slope in the R_{shunt} as a function of driving amplitude. Assuming a constant R_{shunt}, this would erroneosly add to the slope of R_H in figure 2.4 (a) and T_H in (c) and thus affect the Seebeck coefficient. Figure 2.11 shows the R_{shunt} as a function of heater power. In the relevant power region (above 20 μW), no systematic slope is observed.[3]

Considering the discussion above (especially the possibility of a systematic error), an error of 5% was assumed for all Seebeck coefficients determined for the measurements used in this thesis. For future measurements, it is proposed to replace the current shunt resistor with a high precision resistor. The secondary resistor used here with a tolerance of 0.1% would already improve all the relative errors discussed by a factor of 20. This would reduce the R_{shunt} related error in P_H to under 0.01% and the possible errors in Seebeck coefficient to around 0.3%. Precision resistors with tolerances as low as 0.01% are commercially available. Such a shunt resistor could improve both accuracies further by another order of magnitude.

An important conclusion to make from the above discussion is that the accuracy of the

[3]The slope at lower powers is most likely related to the fact that a very small signal is measured without adjusting the DAQ measurement scale. At the lowest power measured the expected precision on a single point measurement is of the order of 0.1%. The deviation we observe is below 0.01%. The improved precision is possible due to the use of FFT on a digital waveform which indirectly averages the measurement output over multiple points.

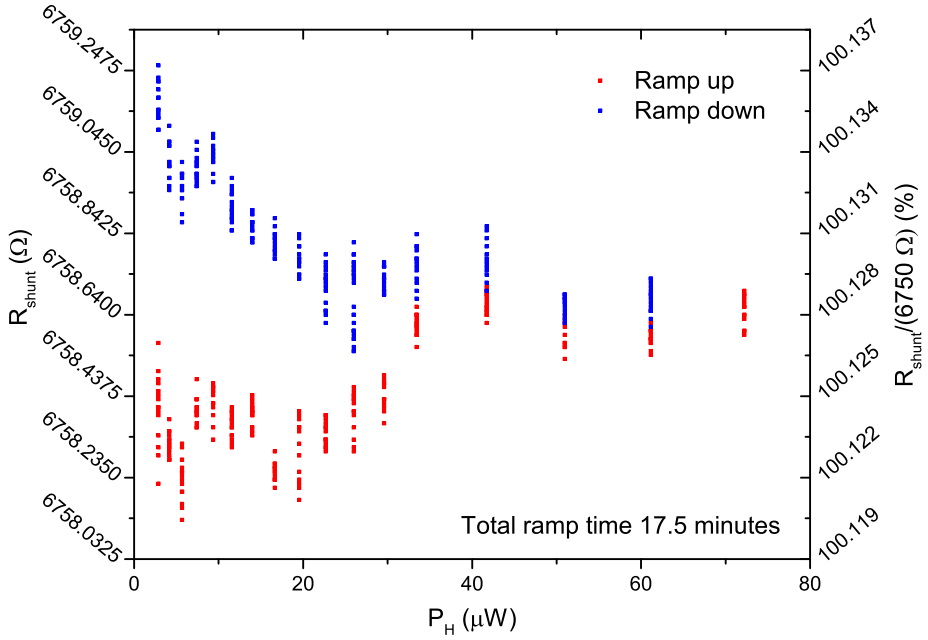


Figure 2.11 R_{shunt} as a function of heater power. The x-axis shows the approximate power that would be dissipated in the heater at the given current (for a direct comparison with figure 2.4). No systematic slope is observed at powers above 20 μW, the slope at lower powers is attributed to DAQ resolution limit.

Seebeck coefficient is determined by the precision (rather than accuracy) of the R_{shunt}. The same applies to V_{heater} and V_{shunt} which are also a factor in the determination of R_H. They are both measured using DAQ card, which will be discussed next.

DAQ Card Optimisation

The DAQ Card is used to measure three channels: V_{shunt}, V_H and V_{th}. Finite time signals are acquired and an FFT is used to determine the rms amplitude at the driving frequency for the former two and the dc offset for the latter.

When using DAQ for multiple-channel scanning it is essential to allow for a sufficient settling time per single measurement (and set the sampling rate accordingly). Important factors affecting the settling time are the source impedance and the scanning order with regards to the signal magnitude and measurement range.

National Instruments recommend (and quote settling times) for input impedances below 1 kΩ. Larger impedances result in a phenomenon called charge injection which, with an insufficient settling time, may result in the signal from the preceding channel to reflect in the output of the high impedance source measurement (so-called ghosting, or crosstalk). From this perspective the shunt resistor of 6750 kΩ is non-ideal and a lower resistance should be used.[4]

Also to avoid ghosting, the scanning order should be chosen so as to minimise steps from large signals to small signals (and large ranges to small ranges). Large changes require larger settling times for the same accuracy (and therefore lower scan rates).

Finally, for the best precision, an appropriate measurement range should be selected. For instance, measuring an 0.6 V signal on a 1 V range instead of 10 V improves the error due to noise and quantisation by an order of magnitude. The settling times for an equivalent accuracy are also much lower.

Currently, all channels are measured on a ± 5 V scale at a scanning rate of 2 kS/s (per

[4]The impedance of the thermopile is an order of magnitude larger, however, the impedance seen by the DAQ is much lower and given by the output impedance of the pre-amplifier.

channel) for operating frequencies up to 10 Hz and ∼10 kS/s for higher frequencies (settling time 167 and 33 μs per sample, respectively). Note that the (amplified) thermopile signal is typically of the order of hundreds of mV, as is the heater voltage. The shunt voltage, however, is an order of magnitude larger due to the ratio between the heater resistance (∼600 Ω) and the shunt. Given this particular setup, the scanning order used (V_{th}, V_{shunt}, V_H) is optimal. Measurement ranges could, however, be reduced for V_H and V_{th} by an order of magnitude.

A a more optimum setup could be achieved by using a shunt resistor comparable with the heater resistance (and reducing the driving voltages accordingly). The input impedance of the shunt would then be below 1 kΩ and all the measured signals would be in the same range (±0.5 V). The use of a smaller range should improve the precision on V_H and V_{th} by a factor of 10. Furthermore, at the ±0.5 V range the settling time for a *full-scale step accuracy* of ±1 LSB (least significant bit) is only 15 μs. Thus, the sampling rate of 20 kS/s could be used without any loss of accuracy due to settling times. Compared with the rate of 2 kS/s, the noise on an average over a fixed time interval could be reduced by a further factor of $\sqrt{10}$. Alternatively, an equivalent precision could be achieved while running at a much shorter period of the program loop clock (it is currently limited by the length of the DAQ signals acquired for the FFT).

A negative impact of the proposed change could be a relative increase of the common-mode signal on V_{shunt} (its potential low is at the potential high of the heater), which would become comparable with the signal itself (a relative increase of an order of magnitude). However, with the DAQ common-mode rejection ratio (CMRR) of 105 dB (DC to 60 Hz) on the relevant range, it is not significant.

An aspect to consider with regards to finite sampling of a time signal is aliasing of high frequency signals. Frequencies above half the sampling rate alias into the measured signal at a lower frequency. A possible way to avoid this is to apply a low-pass (anti-aliasing) filter at the DAQ input. These, however, limit the settling time by the time constant of the filter.

In the case of V_{shunt} and V_H, an anti-aliasing filter is not necessary thanks to the FFT being used to look at a particular frequency (the driving frequency). This is true provided that the base noise is examined and the chosen operating frequency is away from any significant noise frequencies (genuine or alias).

For V_{th} the DC offset is of interest. Any noise at an integer multiple of the sampling rate aliases in as an additional (spurious) DC signal. The pre-amplifier includes a low-pass filter with a cut-off frequency at 20 kHz which limits the aliasing potential. More importantly, the $V_{th,dc}$ is used only for the Seebeck coefficient calibration and the procedure looks at the slope of $V_{th,dc}$ with the heater temperature (i.e. the changes of $V_{th,dc}$ in response to heater power). The slope should by unaffected by any spurious DC offset, since such an offset should remain constant.

Finally, the following is summary of the influence of the DAQ measurement on the overall accuracy of the heat capacity measurement (with the current setup and settings). The DAQ outputs are used to compute P_H and calibrate K.

P_H is given by a product of two DAQ measurements. The relative accuracy of a DAQ measurement is about 0.04% (assuming no inaccuracies due to insufficient settling times). Thus, DAQ related uncertainty in P_H should be about 0.06%. Unlike the uncertainty in R_{shunt}, this is a systematic error affecting only the accuracy, not precision (i.e. it results in the same relative error for absolute heat capacity and heat capacity changes).

For the calibration of the Seebeck coefficient, the precision in V_{shunt}, V_H is important (as discussed in the previous section). It is far better than the current precision in R_{shunt} and therefore a negligible error is introduced by the DAQ measurement. In the last stage of the calibration (figure 2.4), the relative accuracy of the $V_{th,dc}$ measurement may be significant (1% - limited by the gain accuracy of the pre-amp) but in the current setup it is swamped by the uncertainty in K due to fluctuations in R_{shunt} ($\sim 5\%$).

Lock-in Optimisation

The lock-in amplifier (LIA) is an essential component in the heat capacity measurement. The gauge heater (in series with the shunt resistor) is driven by its internal reference signal (typically at 5 Hz and 1.5 V_{rms} magnitude). The thermopile response was detected at the second harmonic of the drive signal (10 Hz). A LIA time constant of 1 s is usually used. This time constant is rather large and it limits the LIA response time to signal changes to about 5 s. This can be significant in the heat capacity measurement which is performed dynamically, at a continuously ramped field (up to 0.5 T/min) or temperature ($\sim$2 K/min). Large and/or sharp changes in heat capacity could be affected by the large time constant.

The LIA output was studied in more detail in order to optimise the measurement. Figure 2.12 shows the LIA output at the usual settings, sampled at a maximum rate available directly through LIA (512 Hz). The output is dominated by (and therefore the large time constant is necessary because of) a well defined oscillatory noise signal as opposed to a random noise (the signal of interest correspond to the dc output). Figure 2.12 also includes an FFT of the LIA output signal. It shows that the noise is mostly a sum of signals at 5, 10, 15 and 20 Hz.

It is worth noting that during an actual measurement the LIA is sampled only once every program loop (see figure 2.6), which is typically of the order of seconds. At 5 Hz drive (and default settings) the program loop clock operates at 3.5 s period (i.e. an integer multiple of the period of 10 Hz signal and its harmonics), therefore the dominant 10 Hz noise aliases in as a spurious additional dc signal (dependent on the phase of the loop cycle with respect to the noise). As a result, the noise observed within the program or the recorded data would be smaller than that seen in figure 2.12 and not obviously periodic. At some other operating frequencies a low frequency noise (an alias) could be observed.

This output can be understood in the context of the basic operating principles of the LIA. The heart of a LIA is a phase-sensitive detector (PSD). Here, the LIA input signal $V_{th,ac}\sin(\omega t+\theta)$, where θ is the signal phase with respect to the reference, is multiplied by

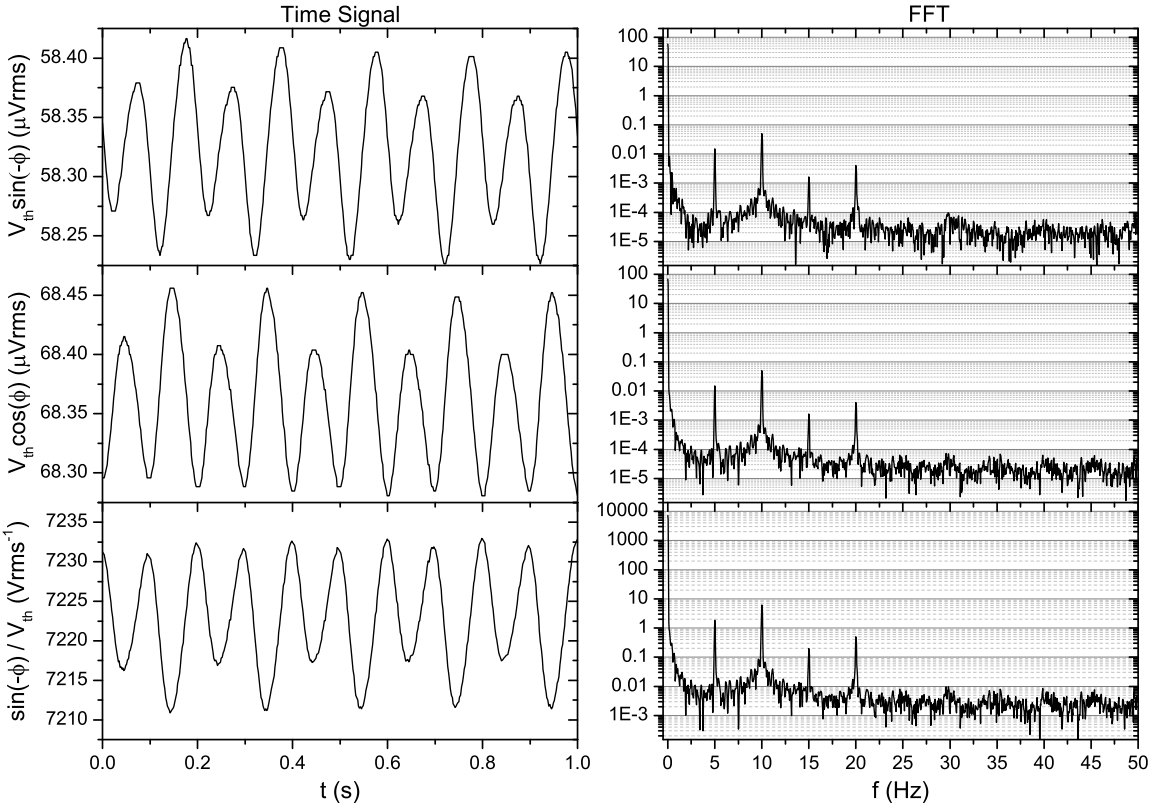


Figure 2.12 LIA output sampled at 512 Hz (1 s sample of a 20 s long signal) and FFT of the full signal. From top to bottom the figure shows the in-phase component, out-of-phase componet and the combination of the two which is proportional to the heat capacity as measured using equation 2.10. The gauge was loaded with a sample and typical measurement parameters were used (drive at 5 Hz, 1.5 V_{rms}, 1 s time constant with 12 dB/oct roll-off). The output is dominated by noise at 5, 10, 15 and 20 Hz. This, however is negligible (only 0.3% noise in the heat capacity) due to the large time constant.

a sine wave at the detection frequency ($V_{ref}\sin\omega t$). The PSD output is then:

$$\begin{aligned} V_{th,ac}\sin(\omega t+\theta)V_{ref}\sin\omega t = \\ = \frac{1}{2}V_{th,ac}V_{ref}\cos(\omega t+\theta-\omega t)+\frac{1}{2}V_{th,ac}V_{ref}\cos(\omega t+\theta+\omega t) = \\ = \frac{1}{2}V_{th,ac}V_{ref}\cos(\theta)+\frac{1}{2}V_{th,ac}V_{ref}\cos(2\omega t+\theta). \end{aligned} \tag{2.37}$$

The signal which is at a detection frequency results in a dc output proportional to the in-phase component of the signal amplitude (measurement objective).[5] There is also an ac output at twice the detection frequency (usually referred to as 2f component). Any other (noise) signal, e.g. $V_n\sin(\omega_n t+\theta_n)$ at a frequency other than the detection frequency will result in two ac output signals, at the sum frequency ($\omega_n+\omega$) and the difference frequency ($\omega_n-\omega$):

$$\begin{aligned} V_n\sin(\omega_n t+\theta_n)V_{ref}\sin\omega t = \\ = \frac{1}{2}V_nV_{ref}\cos((\omega_n+\omega)t+\theta_n)+\frac{1}{2}V_nV_{ref}\cos((\omega_n-\omega)t+\theta_n). \end{aligned} \tag{2.38}$$

Thus, only the signal of interest results in a dc output. Any other input signal results in an ac output. This is attenuated by a low-pass filter applied to the PSD output. The LIA time constant refers to the time constant of this filter and it determines the measurement bandwidth. The LIA used here allows for up to 4 stages of low-pass filtering. All the filters have the same time constant and have a roll-off of 6 dB/oct. Two-stage filtering was usually used (i.e. 12 dB/oct roll-off). The time constant needs to be large enough to attenuate any noise to a sufficient level, however, there is a trade-off between the noise and the LIA response time.

The 20 Hz noise observed in the LIA output can be attributed to the 2f component of the PSD output (detection at f = 10 Hz). From equation 2.38 it follows that a noise directly at the detection frequency can be caused by a dc offset in the LIA input. While it should be minimised by the ac coupling of the LIA input, the dc offset of the thermopile voltage

[5]The LIA also has a second PSD where the reference wave is phase shifted by 90° in order to detect the out-of-phase component of the signal. The total signal amplitude and phase can then be computed.

is comparatively large. It has to be larger than the thermal oscillation amplitude which we are trying to measure.

The 5 Hz and 15 Hz noise in output corresponds to the sum and difference frequency of an input noise at 5 Hz. The presence of a large 5 Hz noise is caused by the cross-talk between the heater (driven at f/2) and the thermopile. Note that rather than within the probe wiring, the cross-talk seems to occur directly on the gauge. It is present even when the gauge is connected directly to the LIA with short and spatially separated leads. *Thus, at any operating frequency we necessarily observe a LIA output noise at f/2 and 3f/2.*

To minimise the cross-talk it is essential to keep the heater and thermopile at a similar potential. Therefore both heater and the thermopile are connected to ground on one side. The cross-talk increases significantly if the shunt resistor is connected to the ground instead of the heater as this results in a large common-mode voltage with respect to the ground being applied to the heater despite the voltage across the heater being unaffected.

The difficulties in attenuation of the 2f component at low operating frequencies are well-known. For this reason the LIA has a so-called synchronous filter, which is available (useful) for detection frequencies below 200 Hz. It averages the LIA output over a full detection period and thus notches out any noise at the detection frequency and its harmonics (including 2f). Unfortunately, because the filter averages over the detection period rather than the drive period, it does not remove the output noise at f/2 and 3f/2.

This is illustrated in figure 2.13. Here the time constant was reduced to just 30 ms, however, with the use of maximum roll-off and, most-importantly, the synchronous filter a relatively stable output could be achieved. With these setting the LIA response time is reduced by an order of magnitude to hundreds of ms.[6] The output is, however, dominated by the f/2 noise which is of the order of 1% of the signal.

The f/2 noise can be eliminated by modifying the data acquisition from LIA. Currently

[6]The use of synchronous filter results in transients of the length of the detection period (here 100 ms). For time constants much smaller than the period, the transient limits the LIA response. For a time constant smaller but comparable with the period, the transient is magnified.

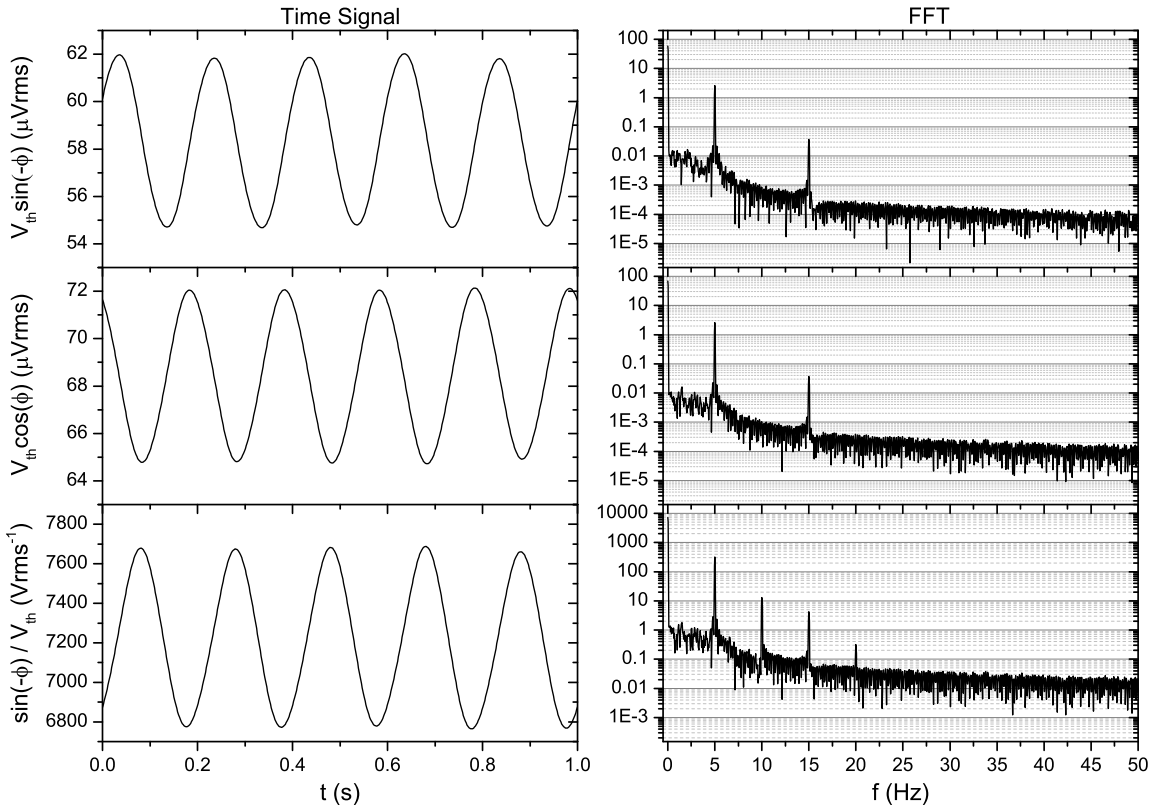


Figure 2.13 Equivalent to figure 2.12 obtained at 5 Hz, 1.5 V_{rms} drive but with reduced time constant (30 ms), maximised roll-off (24 dB/oct) and with the use of synchronous filter.

a single reading is requested per program loop. An alternative communication protocol allows to store precisely timed samples at rates in powers of 2 per second, up to 512 Hz (this was already utilised for figures 2.12 and 2.13). These can then be read out in bulk rather than a point per request. Crucially, averaging over samples equally spaced in time allows us to notch out frequency with the period equal to the total length of the signal AND all its harmonics (up to half the sampling rate). Thus, averaging over 512 samples acquired at 512 Hz removes signals at all integer frequencies up to 256 Hz.

At the maximum sampling rate, it takes almost as long to read out the samples as it does to acquire them. Thus, running the loop clock at 1 s, one can acquire 256 samples (0.5 s signal) per loop and average out frequencies at multiples of 2 Hz. In order to be able to average out the f/2 noise, the operating frequency (twice the heater driving frequency) has to be a multiple of 4 Hz.

Overall, with similar LIA settings and measurement protocol each data point represents an average of 256 readings over 0.5 s and the consecutive data points are separated by another 0.5 s. Thus, there is no information overlap between the data points — a unique data point is produced every second.

Also, the discussion of the G_{ratio} has shown that the usual operating frequency may have been unnecessarily low, which is unfavourable especially considering the general 1/f noise background. With regards to the noise at f, 2f, f/2 and 3f/2 it should be advantageous to increase the operating frequency for easier attenuation of the noise. However, increasing the frequency inevitably reduces the thermal oscillation amplitude while the driving signal (i.e. the f/2 and 3f/2 noise) and the dc offset (f noise) remain unaffected and become relatively more significant. Thus, the frequency increase may not necessarily allow to reduce the time constant without utilising the concepts discussed above.

2.3.6 Measurement Error Summary

The section summarises the errors affecting the measurements presented here and how they are processed. For calculation of heat capacity the simple model was assumed, using

equation 2.10:

$$C = \frac{KP_H}{\omega V_{th,ac}} \sin(-\phi).$$

As discussed, some spurious addenda from various sources may be included, however, it should not effect the field-induced heat capacity changes which are of interest here.

Precision

The measurement precision is essential for determination of small heat capacity changes. It was limited by the noise which was dominated by the noise in LIA output. An error in heat capacity change was estimated based on the noise level in any particular measurement. Due to large time constant, there was a possibility of underestimating sharp changes in heat capacity. Some precision error could arise also due to drift in R_{shunt}, however, it could be identified in the dataset if it was significant.

Relative Accuracy

The accuracy of the heat capacity measurement was determined by the uncertainty in the Seebeck coefficient ($\sim 5\%$), arising most likely due to fluctuations in R_{shunt}. The error was added when comparing/adding heat capacity changes measured at different temperatures.

Finally, an error in mass (up to 10%) was included for comparison with other samples and when specific values were of interest.

Correction factor

An introduction of a correction factor of 2 was necessary for consistency with other data. The need for this factor is argued in figures 4.19 and 5.10 and the related discussion. Since it seems required in two different samples/materials, it is unlikely that this error would arise due to error in mass or that it would be related to the physics of the material studied.

Every effort was made to identify all possible sources of error within the measurement, however, the source of this error was not identified.

Although the factor appears to be an exact factor of 2, that may not be the case. Possible reasons for the correction include:

- Error in signal processing/data analysis
- Error in the thermodynamic description of the system
- Error in the determination of Seebeck coefficient

It is worth noting that the manufacturer of the measurement gauge quotes a nominal thermopile sensitivity of 24 mV/K (as given by the physics of the thermopile leads) and an effective sensitivity of 13 mV/K — the effective sensitivity is said to be reduced by the spatial separation between the heater and the hot thermopile junctions (van Herwaarden, 2010). Using our calibration procedure (section 2.3.3) thermopile sensitivity (the Seebeck coefficient) below 7 mV/K is measured.

An error in the Seebeck coefficient calibration may be due to the heater resistance not yielding the sample temperature accurately. This may arise if the heater has a different temperature dependence of its resistance in an active and passive mode (for example due to internal temperature gradients). The passive mode resistance is obtained when extrapolating heater resistance as a function of power to zero power (figure 2.4 a), whereas $V_{th,dc}$ is measured and the corresponding T_H is determined in an active mode.

2.4 Quasi-adiabatic Temperature Probe for Latent Heat Measurement

As already stated, due to the use of an ac lock-in technique the heat capacity probe cannot measure irreversible heat release such as the release of latent heat at a first order phase transition. The probe was therefore adapted to capture the latent heat in a separate measurement (Miyoshi et al., 2008).

2.4.1 Principle of operation

In the latent heat measurement the thermopile voltage is measured in a dc mode in order to detect a sudden temperature change of the sample (and the addenda) as it is driven through a first order phase transition by an external magnetic field and the latent heat is released. The gauge response to the temperature change is given by the transient (equation 2.3). Thus, with the release of latent heat a sharp change in thermoelectric voltage is expected which then decays exponentially as the heat dissipates into the bath. Assuming that the temperature change is proportional to latent heat (i.e. the heat capacity of the sample plus addenda is constant), the height of the exponentially decaying spike is proportional to the latent heat. In order to convert the height of the spike into latent heat, the thermopile response is calibrated directly by a heat pulse of known energy. This can be supplied by the heater.

The time constant of the decay is given by C/G, where C is the heat capacity of the sample and the addenda, G is the heat exchange parameter describing the thermal link between the sample and the bath. In the ac heat capacity mode the thermal link is dominated be the helium exchange gas. The corresponding time constant is, however, too short ($\sim$20 ms)[7] to allow to detect the latent heat related spike in the thermopile voltage. In order to reduce the thermal link, the sample space is evacuated to pressure of the order of 10^{-2} mbar or less. In these conditions a time constant of about 1 s is achieved and the latent heat related spike can be reproducibly captured provided that its height is above the noise floor of the thermopile voltage.

Note, that because of the reduced thermal link to bath, the probe can be operated only in an isothermal mode. The usual practice is to flush the sample space with helium gas for setting a temperature (with a reasonable equilibration time) and then evacuate the sample space for the measurement.

[7] A quick estimate based on the fact that in the ac heat capacity probe we typically observe a phase lag of around 45° (at driving frequency 10 Hz). Thus $2\pi(10\text{ Hz})C \approx G \rightarrow C/G \approx 20$ ms.

2.4.2 Measurement Setup

The measurement setup for the latent heat measurement is quite simple (figure 2.14). The thermopile signal is pre-amplified using a low-noise analogue dc amplifier (Keithley 140). The amplifier output is then measured using a digital multimeter (HP 3458A) interfaced with a LabVIEW program.

The amplifier uses a minimum rise time setting (0.05 s) yielding a nominal bandwidth of 10 Hz. The actual rise time is increased by the large source impedance of the thermopile, in affect reducing the bandwidth.

For accurate capture of the peak height the emphasis is on fast data sampling. For this reason during a field ramp the magnetic field is not queried simultaneously with the thermopile voltage but it is inferred indirectly from the elapsed time and field ramp rate. Sampling time of approximately 40 ms can thus be achieved.

For the calibration a square voltage pulse as applied to the heater by TTi TG1010 Function Generator. The pulse length, t_{pulse}, is 100 ms, height, V_{pulse}, is typically 2 V. Taking into account the in-series shunt resistor (R_{shunt}) and the output impedance of the function generator ($R_{out} = 50\ \Omega$), the heat of the calibration pulse is:

$$\Delta Q_{cal} = \frac{V_h^2}{R_h} t_{pulse} = \left(\frac{V_{pulse} R_H}{R_H + R_{shunt} + R_{out}} \right)^2 \frac{1}{R_H} t_{pulse} = \left(\frac{V_{pulse}}{R_H + R_{shunt} + R_{out}} \right)^2 R_H t_{pulse}, \quad (2.39)$$

where $R_H(T)$ is known from the calibration run for the ac heat capacity probe.

By using the thermopile voltage change corresponding to the calibration pulse, V_{cal}, (figure 2.15) a voltage change due to a latent heat release, V_L, can be converted directly to latent heat:

$$\Delta Q_L = \frac{V_L}{V_{cal}} \Delta Q_{cal}. \quad (2.40)$$

Note that multiple latent heat spikes can be observed in a single latent heat measurement. V_L is the linear sum of individual spikes.

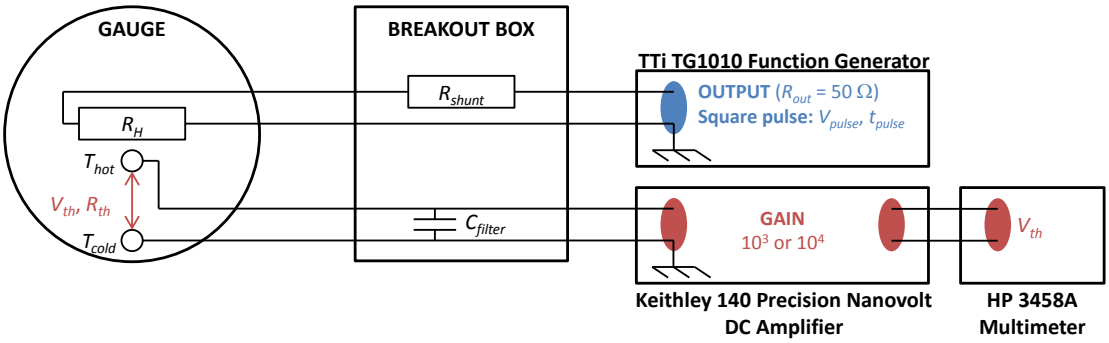


Figure 2.14 Schematic of the instrumentation used for the latent heat measurement.

2.4.3 Measurement Error

The calibration by a heat pulse generated directly at the sample avoids many potential sources of error. For instance, it intrinsically compensates for the spatial separation between the sample/heater and the hot thermopile junction. Any systematic relative inaccuracies (e.g. an imperfect voltage transfer due to large source impedance, relative accuracy of the amplifier gain and voltmeter calibration) are also compensated in this way (provided that the calibration and measurement are performed with the same settings).

The following errors in the variables that are used to determine ΔQ_L were considered:

- According to specifications, the accuracy of the pulse amplitude, V_{pulse}, is 3%.
- The error in t_{pulse} was assumed to be negligible since the rise time of the the function generator for a square wave is only 25 ns, i.e. much smaller than the length of the pulse (100 ms).
- Following the discussion of R_{shunt} in section 2.3.5, an error of 0.2% was assumed in R_{shunt} and R_H. Since R_{shunt} is much larger than R_H and R_{out}, the relative error in $(R_{shunt} + R_H + R_{out})$ was also assumed to be 0.2%.
- The absolute error in V_L and V_{cal} (due to noise and accuracy of the peak height capture due to finite sampling) was estimated by measuring V_{cal} repeatedly for the same heat

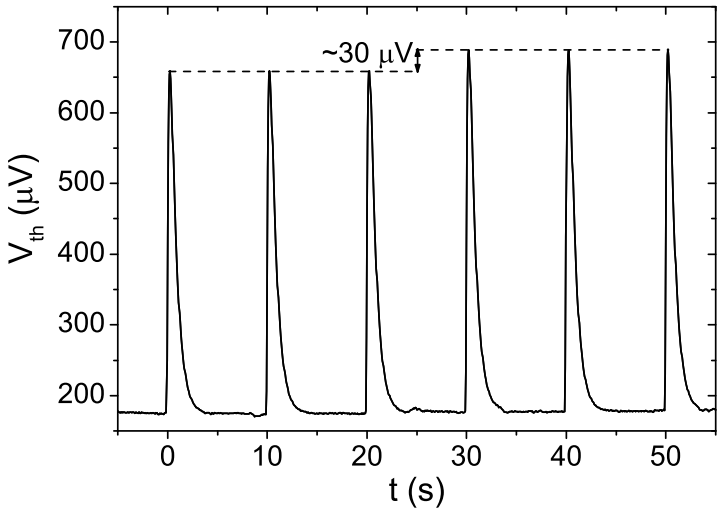


Figure 2.15 Thermopile response to thermopile calibration pulses at 290 K. Three peaks correspond to a positive calibration pulse (+2 V) and another three to a negative calibration pulse (-2 V). The calibration voltages (peak heights) differ by 30 μV due to heater-thermopile cross-talk.

pulse and estimating a standard deviation. It is typically around 0.5 μV, which is about 0.1% of V_{cal} at $V_{pulse} = 2$ V.

- The cross-talk between the heater and thermopile was found to affect the height of V_{cal}. It can be shown by changing the sign of the calibration pulse (figure 2.15). Since the heat evolved by Joule heating is always positive, the parasitic signal from the heater adds on to V_{cal} either constructively or destructively, depending on the sign of the driving pulse. It was assumed that this error can be compensated for by averaging V_{cal} over an equal number of positive and negative driving pulses.[8]

[8]This was not done for some early measurements. As it could not be corrected retrospectively, the V_{cal} error was increased by half the difference of peaks observed for positive and negative driving pulses.

Table 2.2 Typical errors considered in the latent heat calculation.

Factor	Error
t_{pulse}	-
V_{pulse}	3%
R_H	0.2%
$R_H + R_{shunt} + R_{out}$	0.2%
V_{cal}	0.1%
sample mass	up to 10%

Precision

Out of the above the precision (at a fixed temperature) is affected by the error in V_L due to baseline noise and finite sampling. Thus, the precision decreases with the number of latent heat peaks observed in the system as an absolute error is added for each peak.

It is important to note that a systematic underestimation of latent may occur when individual latent heat peaks fall beneath the noise floor of the instrument. Such an error was not reflected in the error bars presented (as it could not be judged objectively).

Relative Accuracy

The relative accuracy and the error therein was included when comparing measurements at different temperatures or adding heat capacity contribution. The accuracy-affecting errors are summarised in table 2.2. Other than sample mass the accuracy is limited by the error in V_{pulse}. The error in sample mass is only included when comparison with other samples is done or the specific values are of interest.

Suggested Improvements

In order to improve the measurement precision the thermopile voltage could be measured using DAQ card which allows for much faster continuous sampling.

Other than sample mass, the accuracy is limited by the uncertainty in calibration pulse driving voltage, V_{pulse}. This could be reduced by employing a simultaneous measurement of the heater voltage and current (as it is done in heat capacity probe) for more accurate determination of calibration pulse energy.

Chapter 3

Analysis

This chapters explains how the isothermal entropy change can be determined from the measured heat capacity and latent heat. The separate measurement of the two quantities allows us to distinguish the first and higher order contributions to the entropy change. While the first order contribution is given directly by latent heat, the determination of the higher order contribution from heat capacity is somewhat more complex. An analysis method has been developed here to appreciate the history dependence of this contribution in very hysteretic systems and to avoid an erroneous inclusion of latent heat-related entropy change. Furthermore, in some cases, an inversion of the method can be used to calculate the latent heat solely from heat capacity data. This provides an independent measure of latent heat to complement the latent heat probe.

3.1 Latent Heat Contribution to Entropy Change

In a reversible process the entropy change of the sample is given by equation 1.6:

$$dS = \frac{đQ}{T},$$

where $đQ$ is the heat flow into the sample and T is the temperature of the sample.

In the latent heat measurement the heat expelled/absorbed by the sample at the first order phase transition (FOPT) is measured directly. Thus, it can be simply converted into

an entropy change yielding the **first order contribution** to the isothermal entropy change:

$$\Delta S_{LH}(T_{iso}) = -\frac{\Delta Q_L}{T_{iso}}. \tag{3.1}$$

It is important to keep in mind that equation 1.6 applies to a reversible process and therefore it is not strictly applicable at a hysteretic first order phase transition. The effects related to this issue are the focus of chapter 5.

3.2 Heat Capacity Contribution to Entropy Change

The link between sample heat capacity and entropy is given by its definition,

$$C = \frac{đQ}{dT}. \tag{3.2}$$

Combined with equation 1.6 it yields

$$dS = \frac{C}{T}dT. \tag{3.3}$$

Note that an integral over temperature is necessary to relate heat capacity to entropy. In the microcalorimeter the heat capacity is usually measured isothermally, as a function of external magnetic field (although it can be measured as a function of temperature). Heat capacity measured at a constant temperature has no simple link to the heat flux (and therefore the entropy change) associated with the change of magnetic field. For a field variation from H_1 to H_2 at a temperature T_{iso} the isothermal entropy change can be calculated as

$$\begin{aligned} \Delta S_{HC}(T_{iso}) = S(H_2,T) - S(H_1,T) = \\ = S(H_2,T_{ref}) - S(H_1,T_{ref}) + \int_{T_{ref}}^{T_{iso}} \frac{C(H_2,T) - C(H_1,T)}{T} dT. \end{aligned} \tag{3.4}$$

where T_{ref} is a reference temperature at which the entropy is known. The usual reference temperature is absolute zero where for most thermodynamic systems the entropy is zero. Thus, the heat capacity (at the initial and final field) has to be measured from 0 K up to the temperature of interest. This approach is not practical for isothermal measurement of heat

capacity as a function of field due to the settling times required at each measurement temperature and the integration error associated with the discrete sampling over temperature.

Alternatively, rather than the absolute entropy of the sample states at H_1 and H_2 (at T_{ref}), the entropy difference between the two states can be used as the reference. It can be determined from a quick magnetisation measurement via a Maxwell relation (only two M(H) loops are required for an estimate of field-induced entropy change at a particular temperature). It is essential though that the reference temperature is chosen such that any field induced changes are fully reversible and the Maxwell relation can be applied reliably (i.e. away from a first order phase transition). An advantage of this approach is the reduction of the integrated error in heat capacity. At an ideal reference point the entropy change would be very small or zero to minimise the absolute error in the reference entropy change due to uncertainty in the mass of the magnetometry sample and, more importantly, the mass of the very small microcalorimetry sample.

Consequently a simplified version of the above equation was generally used before the study presented here was undertaken:

$$\Delta S_{HC}(T_{iso}) = \Delta S(T_{ref}) + \int_{T_{ref}}^{T_{iso}} \frac{\Delta C_{H_1 \to H_2}(T)}{T} dT. \tag{3.5}$$

Just as in the case of the entropy reference point, a knowledge of absolute heat capacity of the sample is not actually required. The field-induced heat capacity *change* is sufficient. Hence the removal of addenda is not necessary provided that the heat capacity of addenda is field-independent. Thanks to the high precision of the isothermal measurement, relative heat capacity changes much smaller than the relative accuracy of the measurement (at any given temperature) can be measured.

When using the ac heat capacity probe to study materials with a first order phase transition (applying equation 3.5), it became apparent that some entropy change was missing. This was understood in the context of an ac measurement being unable to capture the irreversible latent heat evolved at T_{iso} and it stimulated the development of the latent heat measurement.

It was assumed that the heat capacity probe (and equation 3.5) measures only **the second and higher order (continuous)** changes of entropy. The discontinuity in the field-induced entropy change could be recovered through the latent heat measurement. The total isothermal entropy change should then be given by the sum of the two contributions:

$$\Delta S_{tot}(T_{iso}) = \Delta S_{HC}(T_{iso}) + \Delta S_{LH}(T_{iso}). \tag{3.6}$$

It will now be demonstrated that the origin of the missing entropy change was partially misunderstood and a more complex analysis approach is necessary for an accurate separation of the two contributions.

3.2.1 Integral of Heat Capacity Change across a First Order Phase Line

The effect of equation 3.5 is to reconstruct (and immediately subtract) the entropy curves of the sample state at H_1 and H_2. This is illustrated in figure 3.1 in a system with a first order phase transition. The phase diagram shows the integration paths for the two states. The corresponding entropy curves are also shown. As the low-field C/T integral crosses the first order phase line, the discontinuity in the entropy due to latent heat is omitted since the ac heat capacity probe cannot measure it. It can be seen that at the temperature of interest for isothermal entropy change (T_{iso}) we actually obtain:

$$\Delta S_{tot}(T_{iso}) = \Delta S_{HC}(T_{iso}) + \Delta S_{LH}(T_1), \tag{3.7}$$

where T_1 is the temperature at which the low-field heat capacity data crosses the first order phase line.

Thus the $\Delta C/T$ integral is missing the latent heat-related entropy change evolved along the integration path rather than that evolved at T_{iso}. The latter was assumed in equation 3.6. That equation actually measures:

$$\Delta S'_{tot}(T_{iso}) = \Delta S_{tot}(T_{iso}) + \Delta S_{LH}(T_{iso}) - \Delta S_{LH}(T_1). \tag{3.8}$$

The measurement deviates from the actual entropy change by the difference between the first order (latent heat) contribution at T_{iso} and T_1. The entropy change of a first order

material (dominated by the first order contribution) usually varies only very little with temperature resulting in the characteristic plateau in entropy change where the first order phase line can be crossed within the field range. Thus it is not surprising that this error was not obvious.

In fact, a discrepancy was first observed in a melt-spun $LaFe_{11.6}Si_{1.4}$, which has a first order Curie transition at zero field. The latent heat associated with the metamagnetic transition reduces linearly with increasing temperature (Morrison et al., 2010). Due to the large difference in the latent heat contribution for the high field and low field integration paths, the entropy change from heat capacity displayed a large offset (compared with what was expected from magnetometry) when the integral fully crossed the phase line. A correction was applied, however, since the origin of the discrepancy was not fully understood at the time, it did not account for the full extent of the problem.

3.2.2 An Accurate Separation of Entropy Change Contributions

An obvious correction to compensate for the aforementioned effect would be to measure the total entropy change at T_{iso} using equation 3.7. This would require the direct measurement of $\Delta S_{LH}(T(H_1, T_1)$. The first and higher order contributions could still be separated by subtracting the first order (latent heat) contribution measured directly at T_{iso}.

Nevertheless, $\Delta S_{LH}(H_1, T_1)$ is, to a certain extent, an arbitrary variable to use in the determination of an isothermal entropy change at a different temperature (it is given only by *choice* of the lower bound for field variation). Its first order nature, the associated hysteresis and therefore the limited applicability of equilibrium thermodynamics makes the measurement of entropy change at T_{iso} convoluted with any errors/effects related to the measurement of $\Delta S_{LH}(H_1, T_1)$.[1]

An alternative analysis approach has been developed. It is illustrated in figure 3.2.

[1] Furthermore, a conventional/practical lower bound for field variation is at 0 T. This would be particularly difficult to measure in the latent heat measurement which is designed to operate isothermally and drive the FOPT by applying field.

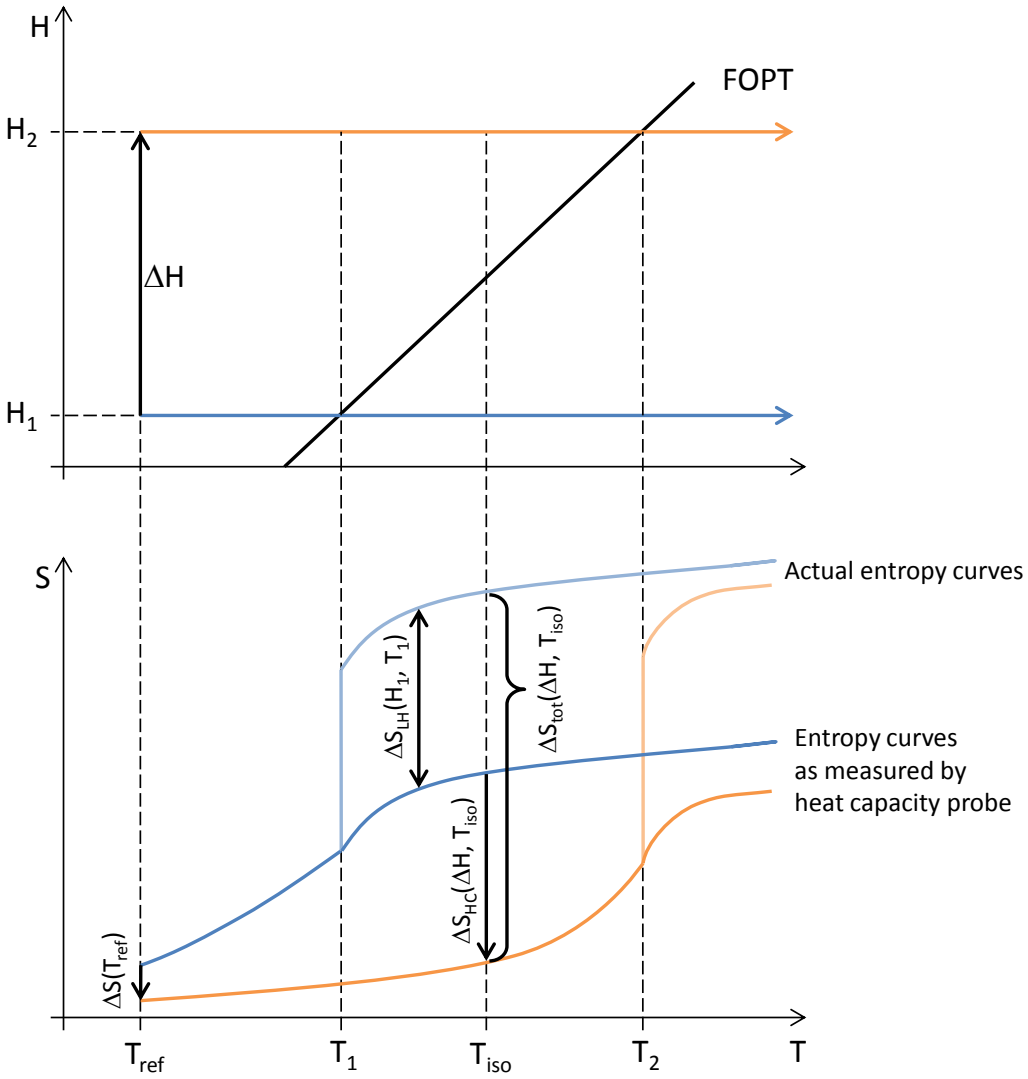


Figure 3.1 Schematic of an isothermal entropy change as measured using the ac heat capacity probe in use with equation 3.5. The phase diagram (top) depicts the integral paths for C/T at high field and low field. The integral fully reconstructs the sample entropy curves (bottom) until the first order phase line is crossed. Due to the use of an ac measurement and finite hysteresis, the heat flux associated with the discontinuity in entropy is not measured. The integrated entropy curve becomes offset with respect to the actual entropy curve (shown in lighter shade). The offset corresponds to the discontinuous (first order) entropy change at the particular point where the integral crosses the phase line. Thus, at T_{iso} the entropy change measured by equation 3.5 is $\Delta S_{tot} - \Delta S_{LH}(H_1, T_1)$; NOT $\Delta S_{tot} - \Delta S_{LH}(T_{iso})$

In order to avoid the heat capacity integral crossing the first order phase line, the heat capacity contribution of the low field state and the high field state (e.g. pre- and post-FOPT on field application) is evaluated separately. They are integrated from a high and low temperature reference point, respectively. Thus the total entropy change on a field application is given by:

$$\Delta S_{tot}(T_{iso}) = \Delta S_{HC,LF}(T_{iso}) + \Delta S_{LH}(T_{iso}) + \Delta S_{HC,HF}(T_{iso}), \tag{3.9}$$

where $\Delta S_{HC,LF}(T_{iso})$ is the low field heat capacity contribution,

$$\Delta S_{HC,LF}(T_{iso}) = \Delta S(T_{ref2}) + \int_{T_{ref2}}^{T_{iso}} \frac{\Delta C_{H_1 \to H_C}(T)}{T} dT, \tag{3.10}$$

and $\Delta S_{HC,LF}(T_{iso})$ is the high field heat capacity contribution,

$$\Delta S_{HC,HF}(T_{iso}) = \Delta S(T_{ref1}) + \int_{T_{ref1}}^{T_{iso}} \frac{\Delta C_{H_C \to H_2}(T)}{T} dT. \tag{3.11}$$

This approach directly tracks the process of an isothermal field application and the entropy change associated with it. Any heat capacity data within a single integral are wholly on one side of a first order phase line where it should be possible to consider any path taken as fully reversible.

This approach adds a level of complexity to the analysis. In order to characterise a material the isothermal entropy change as a function of temperature should be measured. The H_C is different at any chosen T_{iso} and a different heat capacity change has to be measured for each temperature of interest. Experimentally, the isothermal heat capacity measurement (with a continuous sampling in field) is well suited. C_H can be measured for a selection temperatures (sampled densely enough for numerical integration). The critical fields of interest (and corresponding heat capacity changes) can be identified and extracted after the measurement.

Also, the analysis relies on a digital-like FOPT with a well-defined critical field. This is important for being able to measure the heat capacity at the critical field on either side of the FOPT accurately. It is particularly important in systems showing a critical behaviour in

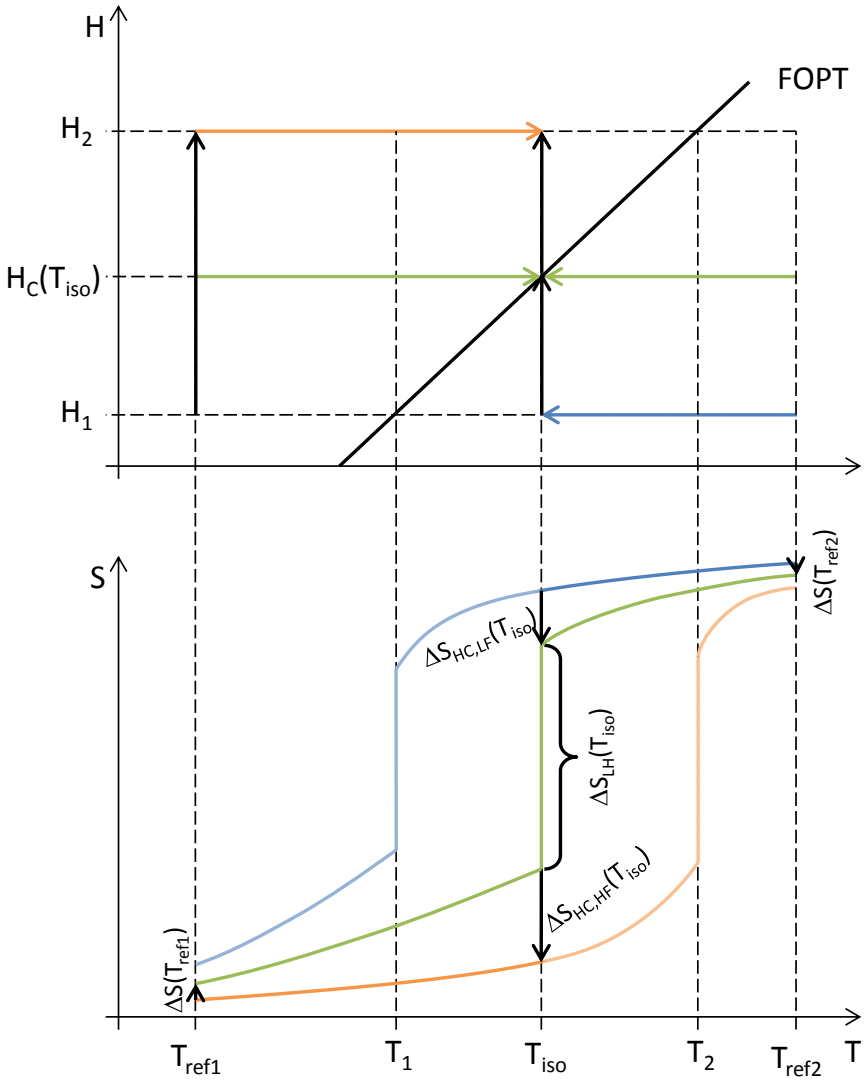


Figure 3.2 An alternative analysis method for determining the heat capacity contribution. Low field and high field states (and the field variation within) are considered separately. The heat capacity integration approaches but does not cross the first order phase line. Thus, it is in not affected by any entropy change related to latent heat.

heat capacity near the FOPT. This may have a dominant effect on the heat capacity integral over a very small temperature range when approaching the FOPT.

From this point of view, the measurement of tiny fragments as advantageous. While in bulk most systems display a *smearing* of the FOPT (for instance due to inhomogeneity, internal strains or temperature gradients), the transition in the small fragments studied in the microcalorimeter is usually much more digital. In fact, the latent heat measurement relies on the instantaneous release of latent heat.

3.2.3 Treatment of hysteretic systems

So far in this chapter only a single phase line has been considered. However, due to hysteresis a system with an FOPT is typically characterised by two phase lines: that for a phase transition from low field state to a high field state and that for the reverse transition which occurs at a lower field. The analysis discussed above can be applied directly by identifying the two critical fields, $H_{C\uparrow}$ and $H_{C\downarrow}$ for field application and removal, respectively. The corresponding integral paths are illustrated in figure 3.3.

Assuming a digital FOPT at the phase lines, two states (heat capacity values) are possible anywhere within the hysteresis region set by the two phase lines. When probing the entropy change on field application (and the phase line associated with it), the sample heat capacity integrated through the hysteresis region should be that of the low field state. This is usually true for an isothermal heat capacity measurement on field application provided that the sample is outside the hysteresis region at the initial field (H_1). If it is not, a low field initial state can be ensured by approaching the initial measurement point from outside the hysteresis region (on the side of the low field state) in a way that does not cross the low field to high field state phase line. An equivalent concept applies on field removal.

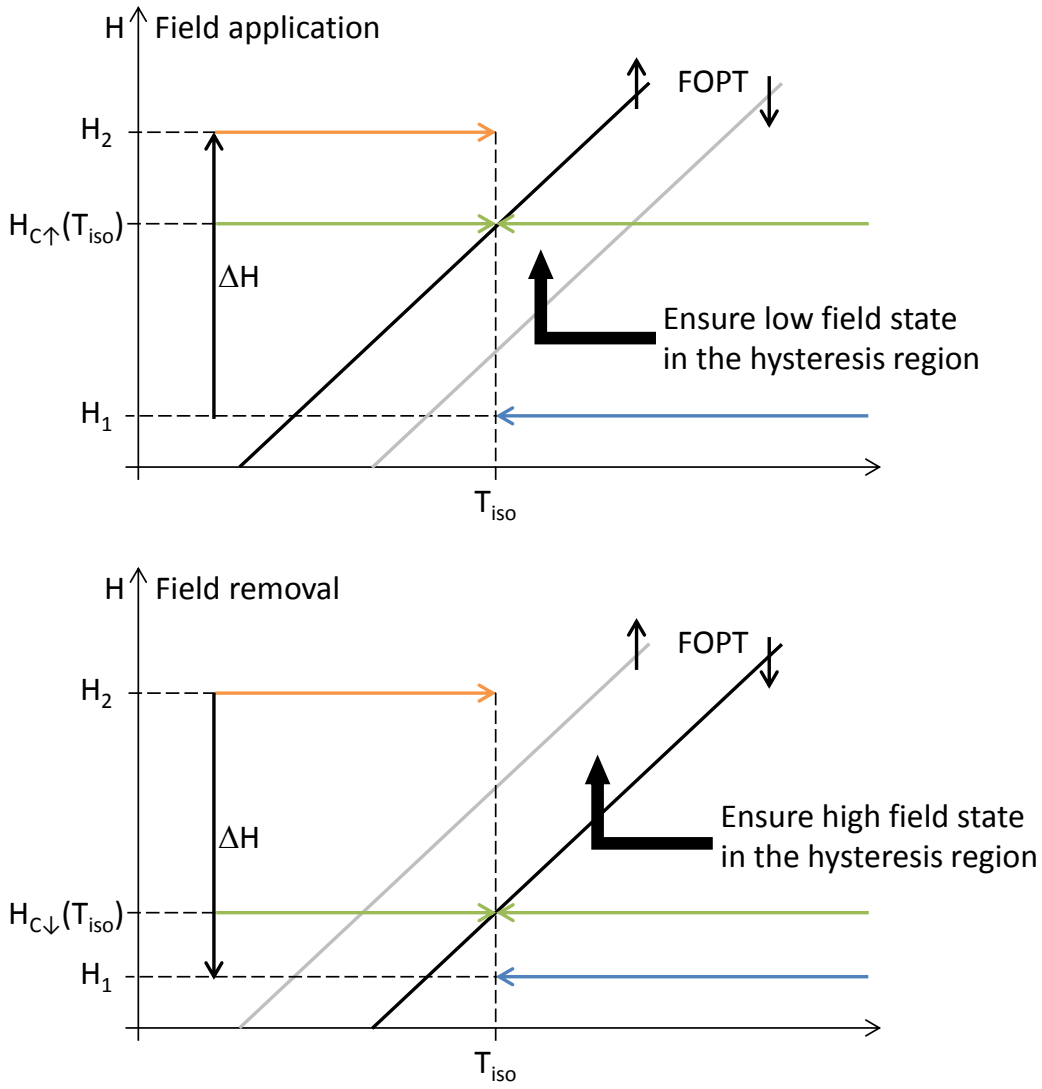


Figure 3.3 Integration paths for the heat capacity contribution in case of a hysteretic first order phase transition.

3.3 Utilising the interplay between latent heat and heat capacity

The information about latent heat contained within the heat capacity data can be used to one's advantage, as described in one of the key publications for this thesis (Morrison et al., 2012).

Consider an extension of figure 3.1, where the integral of $\Delta C/T$ fully crosses the first order phase line (figure 3.4). Since the integral begins and ends in a reversible region of the phase-space (away from the first order phase transition) the actual entropy change on either side ($\Delta S(T_{ref1})$ and $\Delta S(T_{ref2})$) can be estimated independently from magnetisation measurements. From figure 3.4 it follows that:

$$\Delta S(T_{ref1}) + \int_{T_{ref1}}^{T_{ref2}} \frac{\Delta C_{H_1 \to H_2}(T)}{T} dT = \Delta S(T_{ref2}) - \Delta S_{LH}(H_1) + \Delta S_{LH}(H_2). \tag{3.12}$$

Thus, using both reference points and the integral of *heat capacity-only* data, the difference in latent heat between H_1 and H_2 can be measured indirectly.

Such an approach can be particularly useful in weakly first order materials and materials where the latent heat is too distributed (even within a small fragment) to be measured by the latent heat probe directly. This may occur when an individual latent heat spike falls beneath the noise floor of the instrument. A quick succession of such spikes may result in a fluctuation in the baseline that appears continuous and therefore it cannot be distinguished from the higher order contribution.

Provided that the latent heat at, say H_1, is either **well-defined** (i.e. it can be measured directly using the latent heat probe) or **non-existent** (for instance, in a system with a tricritical point where a first order phase transition becomes second order), equation 3.12 can be used to measure the latent heat at H_2 where it may be to weak or too distributed for the latent heat probe.

Quite often, the actual nature of the phase transition (first vs. higher order) may be disputed (in a particular field range). Equation 3.12 can be used to look for a presence of any latent heat and thus identify the nature of the phase transition.

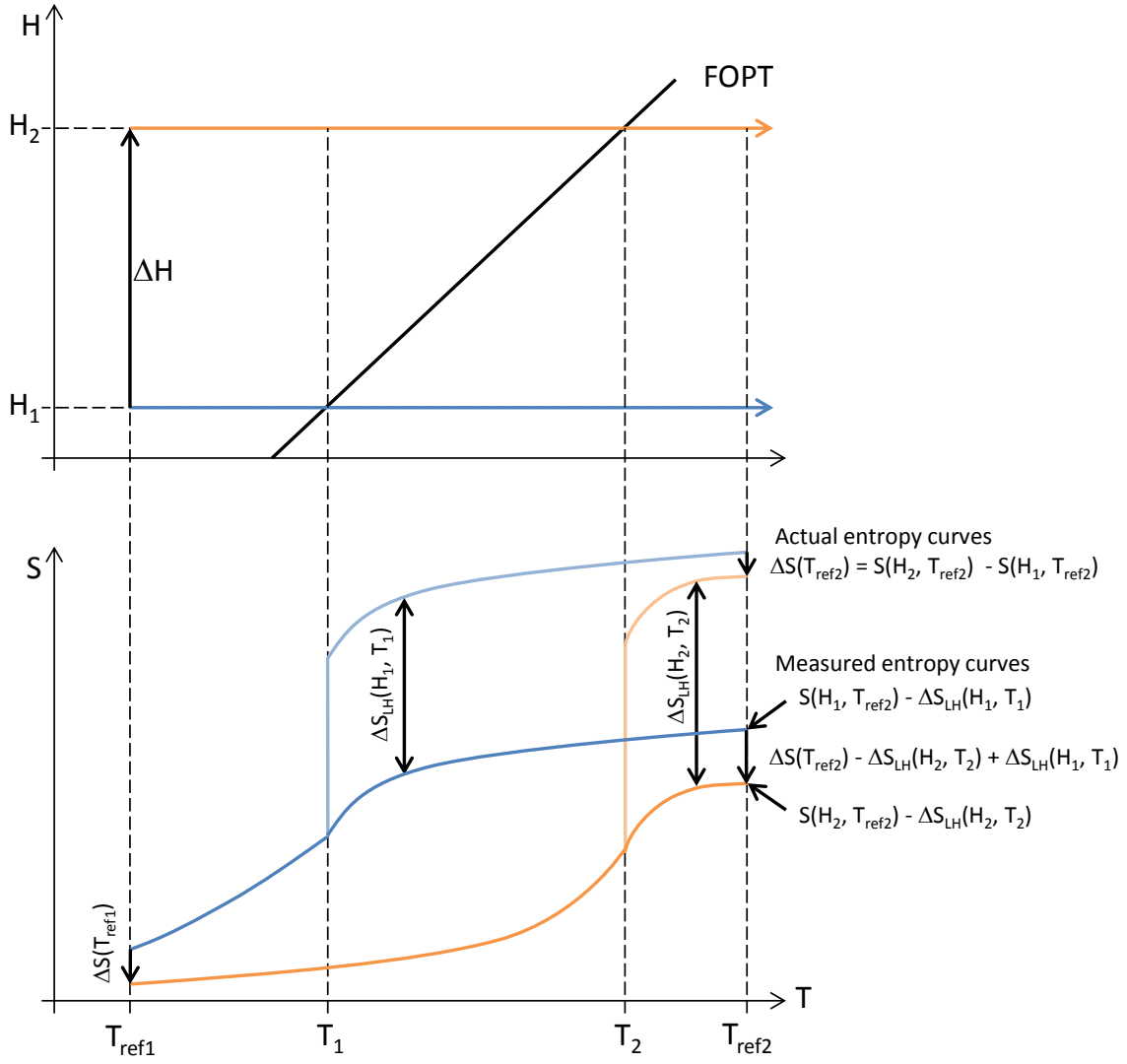


Figure 3.4 Heat capacity integral fully crossing a first order phase line. Despite measuring only heat capacity without any latent heat, the integral of heat capacity change (given by the difference between the depicted entropy curves) includes information about the difference in latent heat between H_1 and H_2.

3.3.1 Measuring the Equilibrium Entropy Change of a First Order Phase Transition

An interesting concept arises in a material with tricritical point where an FOPT becomes second order. An example is shown in figure 3.5. The figure shows an integration path which measures the full entropy change at T_{iso}, however, the first order phase line is not crossed throughout the process. Thus, the measurement corresponds to a fully reversible path on the phase diagram and thus measures the reversible (equilibrium) entropy change at T_{iso}. This could be compared with the actual isothermal equilibrium change at T_{iso} (measured using the approach in section 3.2.2) which is inevitably affected by the hysteresis. The effects of hysteresis could be directly compared with an experimentally measured equilibrium entropy change.

3.4 Propagation of Errors

In the direct measurement of the latent heat contribution to the isothermal entropy change (equation 3.1), the relative error is determined by the error in the latent heat. The error in isothermal temperature is assumed to be negligible. For a given heat capacity contribution (equations 3.10 and 3.11), the integral is performed over heat capacity changes determined from isothermal measurements with a discrete sampling in temperature. Thus a trapezium rule is used to approximate the integral over temperature. The error of the integral is calculated by propagating the relevant errors in heat capacity change through the trapezium formula.

An underestimation (overestimation) of the integral is possible if the temperature dependence of $|\Delta C/T|$ is systematically concave down (up). Such an error is not reflected in the error bars presented here.

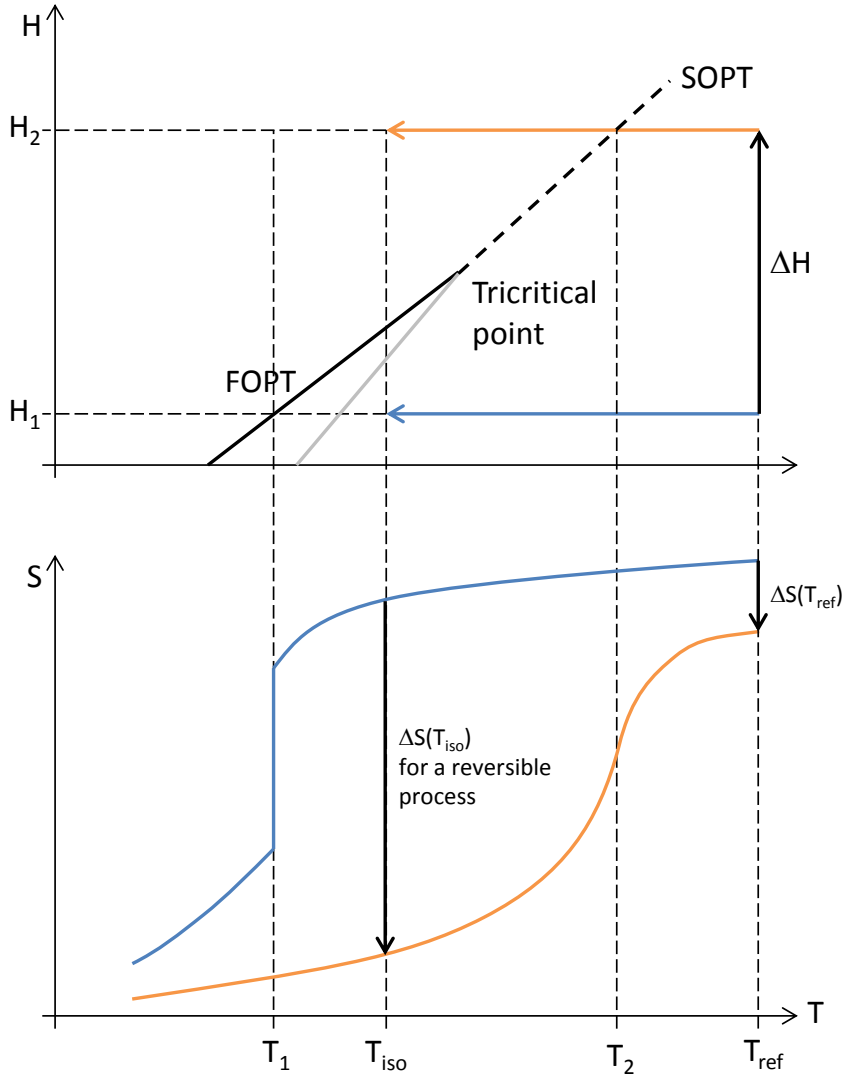


Figure 3.5 Schematic for a system with a tricritical point. An integration of $\Delta C/T$ from a high temperature reference point fully reconstructs the entropy curves and therefore yields the full entropy change (no first order phase line is crossed). The reference points as well as integration paths correspond to a fully reversibly process and thus measure an equilibrium entropy change at T_{iso}.

Chapter 4

'Colossal' magnetocaloric effect: Is it an artefact or history-dependent effect?

This chapter is concerned with one of the most controversial topics within the magnetocalorics community. The application of Maxwell relation in very hysteretic first order systems has led to reports of 'colossal' MCE, which were later widely disputed. It was shown that a non-colossal estimate can be achieved by following a different magnetisation protocol. Here the different thermomagnetic histories were reproduced and studied in a direct measurement using the field-sweeping capability of the microcalorimeter.

4.1 Review of the 'colossal' magnetocaloric effect in MnAs and other compounds

At room temperature MnAs is a ferromagnet with hexagonal NiAs-type structure. It undergoes a magnetostructural transition at around 315 K to a paramagnetic state with orthorhombic MnP-type structure. The first order transition has a thermal hysteresis of about

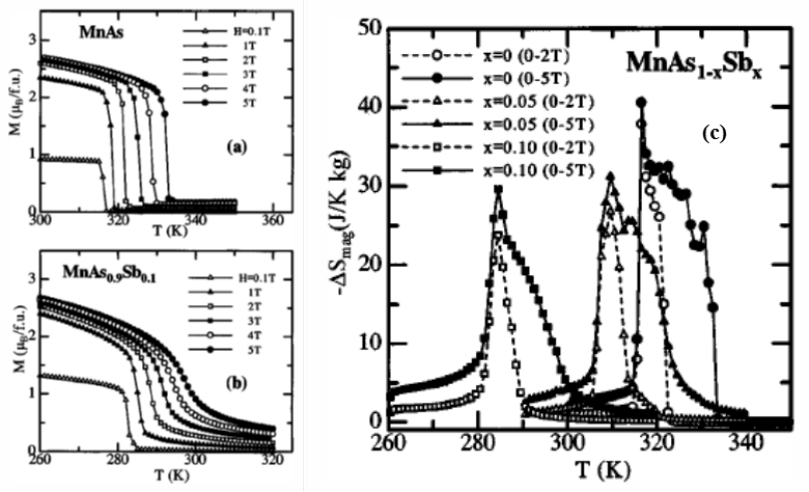


Figure 4.1 Isofield magnetisation data for (a) MnAs and (b) $MnAs_{0.9}Sb_{0.1}$ at various magnetic fields. (c) The isothermal entropy change was calculated from the magnetisation data using the Maxwell relation. Reprinted with permission from Wada and Tanabe (2001). Copyright 2001, AIP Publishing LLC.

10 K (Menyuk et al., 1969).

A giant MCE in MnAs was first reported by (Wada and Tanabe, 2001). The entropy change was as large as 30 J K^{-1} kg^{-1}. In reaction to the unfavourably large thermal hysteresis of the transition, they studied the series $MnAs_{1-x}Sb_x$ with x = 0, 0.05 and 0.10, expecting to reduce the hysteresis with increasing antimony content. They reported vanishing thermal hysteresis for $x \geq 0.05$. Furthermore, the transition temperature was lowered from 318 K to 280 K for x = 0.10 yet the giant magnetocaloric effect was preserved. The entropy change was calculated from isofield magnetisation measurements using the Maxwell relation. Figure 4.1 shows their magnetisation data and the calculated isothermal entropy changes.

Tegus et al. (2002) reported a giant MCE in $MnFeP_{0.45}As_{0.55}$ which crystallises in the Fe_2P-type structure and has a Curie temperature of about 300 K. The magnetoelastic transition has thermal hysteresis of under 1 K. The isothermal entropy changes are comparable

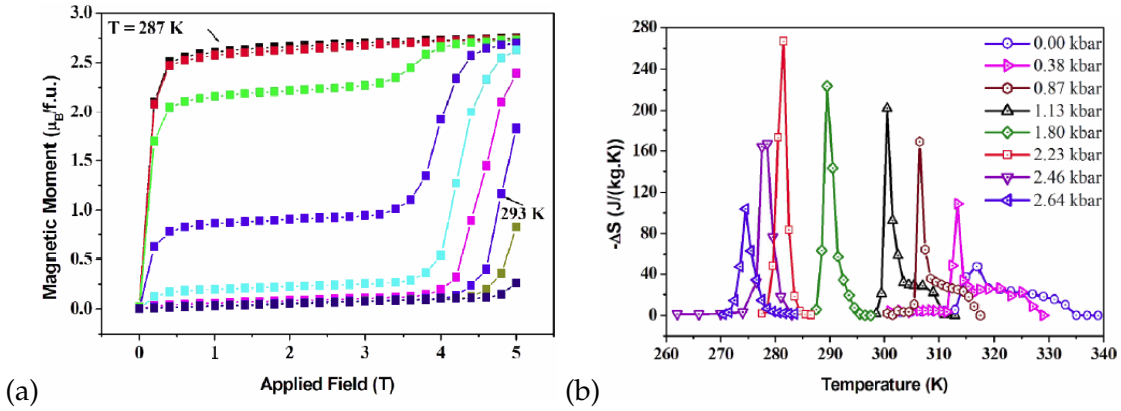


Figure 4.2 (a) Isothermal magnetisation data of MnAs at a pressure of 1.80 kbar taken on field increase and with increasing temperature. (b) Isothermal entropy change of MnAs for field variation 0 to 5 T at different pressures calculated using the Maxwell relation. Reprinted figures with permission from Gama et al. (2004). Copyright 2004 by the American Physical Society.

to $Gd_5Si_2Ge_2$ reaching 18 $J\,K^{-1}\,kg^{-1}$, however, a large MCE above room temperature is attainable. The Curie temperature is tuneable with the P/As ratio between 3/2 and 1/2 in the temperature range from 200 K to 350 K.

In 2004, Gama et al. reported the 'colossal' MCE in MnAs under pressure. The measured entropy changes reached unprecedented values of up to 267 $J\,K^{-1}\,kg^{-1}$ at 2.23 kBar. What is more, for the first time the isothermal entropy change surpassed the magnetic entropy limit, as given by equation 1.2. For MnAs the maximum magnetic entropy change is only 103 $J\,K^{-1}\,kg^{-1}$. The discrepancy was attributed to a large lattice entropy change contributing to the total entropy change in the coupled magnetostructural phase transition. The isothermal entropy change in this last case was again calculated using Maxwell relation. The magnetisation data were taken in isothermal mode *"with both field and temperature increasing"*. Figure 4.2 shows an example of the isothermal magnetisation data and the calculated entropy changes at different pressures.

It can be noticed that the MCE increases with pressure until 2.23 kbar when it starts

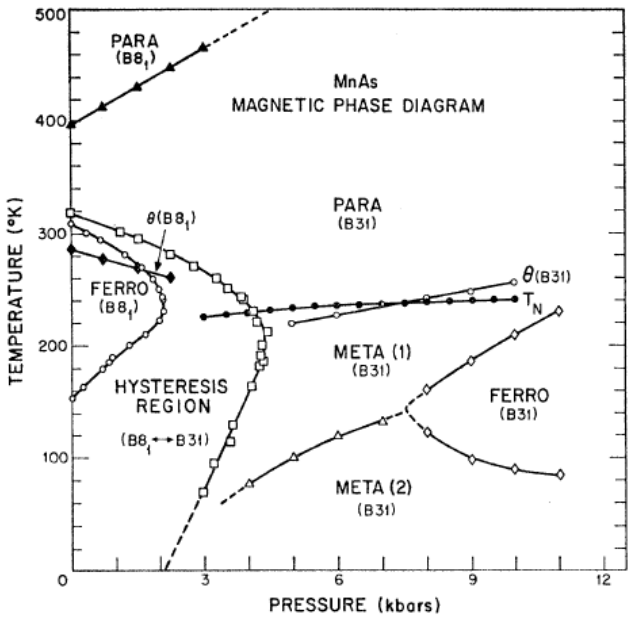


Figure 4.3 *P-T* magnetic phase diagram of MnAs. Reprinted figure with permission from Menyuk et al. (1969). Copyright 1969 by the American Physical Society.

dropping. As can be seen from the phase diagram of MnAs (figure 4.3), this corresponds to the pressure when the first order magnetostructural transition (hexagonal ferromagnet to orthorhombic paramagnet) gives way to second order magnetic phase transition (antiferromagnet to paramagnet). It is also worth noting that with increasing pressure the thermal hysteresis of the magnetostructural transition increases.

The same group then focused on study of MnAs derivatives, aiming to reduce hysteresis and obtain the 'colossal' MCE at lower or even ambient pressure. They soon reported the 'colossal' MCE at ambient pressure, at a temperature that was tuneable by composition in $Mn_{1-x}Fe_xAs$ (de Campos et al., 2006). They expected that the substitution of Fe for Mn should emulate the pressure based on the slight difference of atomic radii of the two atoms. Indeed, the effect of positive pressure induced by substituting Fe on the Mn site has been reported before (Zieba et al., 1987; Fjellvåg et al., 1988). Figure 4.4 shows the magnetic and structural phase diagram of this composition which is very similar to

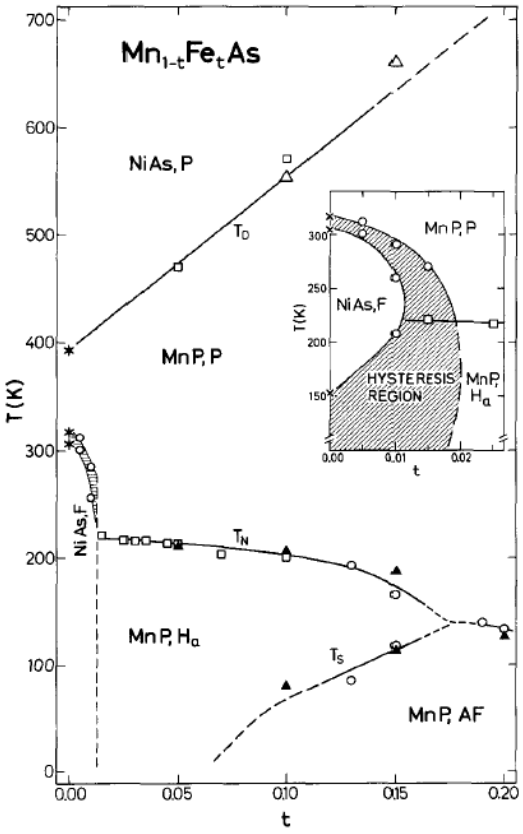


Figure 4.4 Structural and magnetic phase diagram for $Mn_{1-t}Fe_tAs$. Reprinted from Fjellvåg et al. (1988), copyright 1988, with permission from Elsevier.

that of MnAs under pressure. In the relevant region with a magnetostructural transition the hysteresis increases with increasing iron content. This is consistent with the report of de Campos et al. (2006) showing a linear increase of thermal hysteresis from 10 K to about 30 K for x = 0.015.

The measurement procedure was the same as for MnAs under pressure, i.e. the entropy change was determined using a Maxwell relation from isothermal magnetisation measurements for increasing field and temperature. Figure 4.5 shows an example of isothermal magnetisation data, similar to that of MnAs under pressure. The reported isothermal entropy changes are shown in figure 4.6. Again, the MCE dies away for $x \geq 0.015$ for the same reasons as in the case of MnAs under pressure.

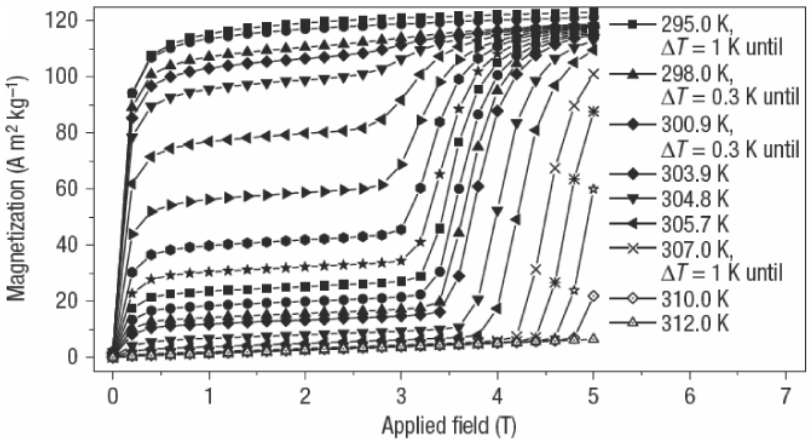


Figure 4.5 Isothermal magnetisation data on $Mn_{1-x}Fe_xAs$ for x = 0.006. Reprinted by permission from Macmillan Publishers Ltd: Nature Materials (de Campos et al., 2006), copyright 2006.

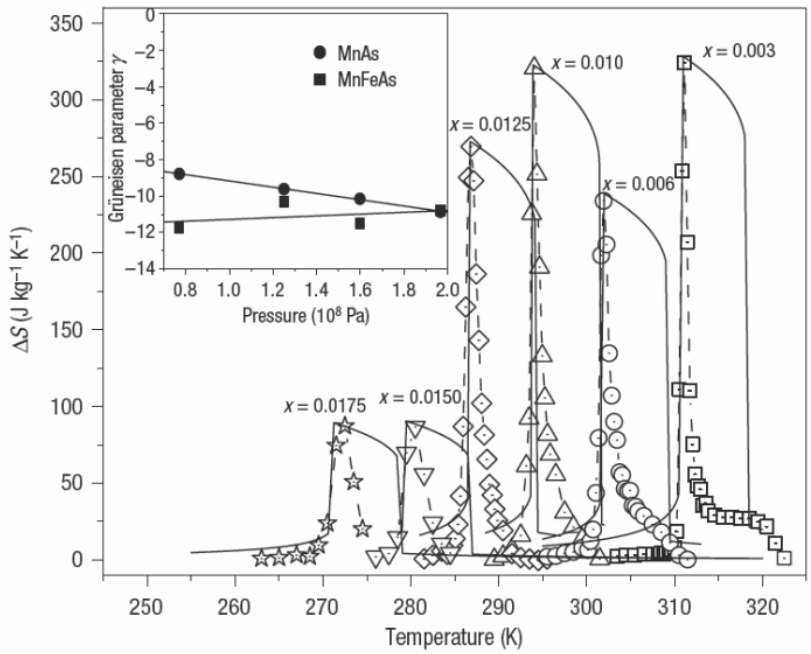


Figure 4.6 The 'colossal' isothermal entropy change reported for $Mn_{1-x}Fe_xAs$ for field variation of 5 T. Reprinted by permission from Macmillan Publishers Ltd: Nature Materials (de Campos et al., 2006), copyright 2006.

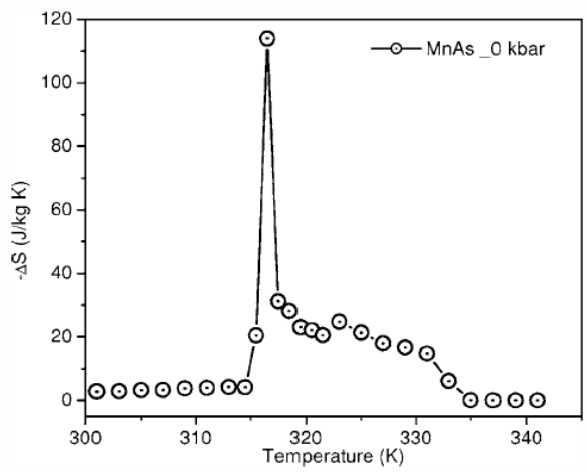


Figure 4.7 'Colossal' MCE in MnAs at ambient pressure measured by applying Maxwell relation to isothermal magnetisation data. Reprinted figure with permission from von Ranke et al. (2006). Copyright 2006 by the American Physical Society.

In a paper concerning the theoretical description of the 'colossal' MCE (von Ranke et al., 2006) the authors also reviewed the measurement of MCE in MnAs at ambient pressure, since the entropy change reported by Gama et al. (2004) was significantly lower than the average behaviour obtained for the other pressures (figure 4.2). They repeated the measurement using the isothermal magnetisation procedure confirming the 'colossal' MCE even at ambient pressure (figure 4.7). This result conflicted with the report of Wada and Tanabe (2001), nevertheless, the capture of 'colossal' MCE was attributed to finer temperature and field variations.

Nonetheless, the presence of the 'colossal peak' is very spurious. As already discussed in section 1.2, from a thermodynamic consideration of first order phase transitions, a plateau is expected in the plots of entropy change vs. temperature. This can be observed in most of the 'colossal' MCE measurements (figure 4.2, figure 4.6, figure 4.7), however, its height is not colossal at all. There is usually only a 'colossal peak' which cannot be accounted for within the framework described in section 1.2, unless there is a spike in one of the total entropy curves.

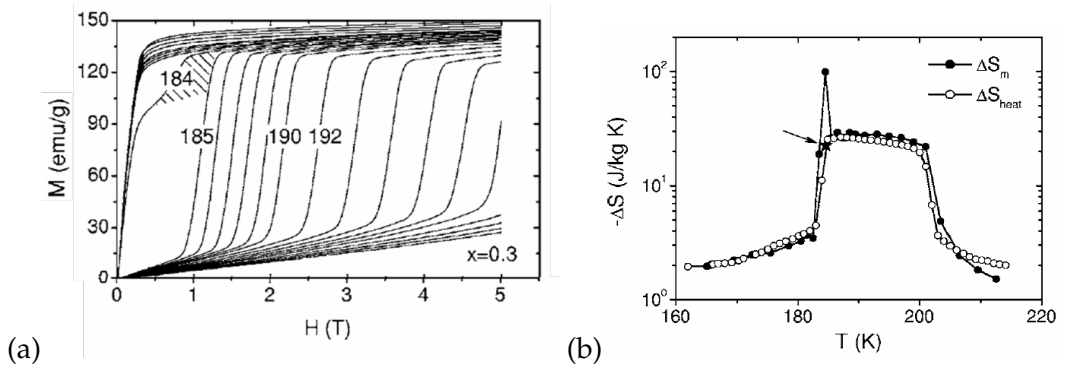


Figure 4.8 (a) Isothermal magnetisation data of $La_{0.7}Pr_{0.3}Fe_{11.5}Si_{1.5}$. (b) Isothermal entropy change of the same material for field variation of 5 T as determined using Maxwell relation (closed symbols) and calorimetry (open symbols). Arrow points at a data point corrected for the contribution from metamagnetic transition only. Reprinted with permission from Liu et al. (2007). Copyright 2007, AIP Publishing LLC.

Similar peaks were observed also in other systems. Liu et al. (2007) measured such a 'colossal peak' in $La_{1-x}Pr_xFe_{11.4}Si_{1.4}$ which is a system with hysteretic first order magnetoelastic phase transition. Again, the peak was derived using Maxwell relation on isothermal magnetisation data. Liu et al. also performed a calorimetric measurement (in temperature-sweeping mode), which showed no 'colossal peak' (figure 4.8).

A common feature of the materials displaying 'colossal' MCE is a plateau in magnetisation before the occurrence of the field-induced transition, as can be seen in all the relevant isothermal magnetisation data. In a paramagnetic (PM) to ferromagnetic (FM) transition this is an indication of phase-coexistence of the PM and FM state, where the FM fraction saturates, resulting in the intermediate plateau, before the PM fraction undergoes field-induced transition. More importantly, the temperature region in which this occurs coincides with the position of the 'colossal peak' in entropy change. This led Liu et al. to conclude that Maxwell relation cannot be used in the vicinity of Curie temperature where there is a coexistence of PM and FM phase. Liu et al. proposed a graphical method to correct for the error in entropy calculation. As follows from the Maxwell relation, the en-

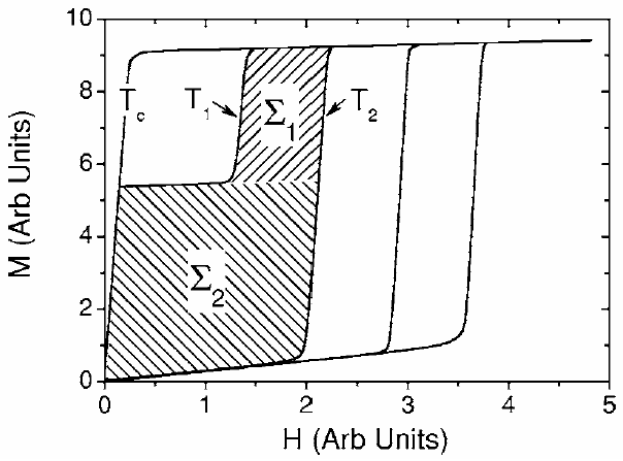


Figure 4.9 Schematic diagram showing the calculation of entropy change in case intermediate saturation due to phase coexistence. Reprinted with permission from Liu et al. (2007). Copyright 2007, AIP Publishing LLC.

tropy change at a temperature between two magnetisation isotherms is given by the area enclosed by the two isotherms normalised by the temperature step between them. For the case of mixed-phase state depicted in figure 4.9 this gives

$$\Delta S \frac{T_1 + T_2}{2} = \frac{\Sigma_1 + \Sigma_2}{T_1 - T_2} \tag{4.1}$$

The authors said that since the transition takes place in the PM phase, only Σ_1 should contribute to ΔS. The huge ΔS spike arises due to inadequate inclusion of Σ_2 in the calculation. Using this correction, the spike in entropy change disappears (Figure 4.8).

Several other, very similar treatments of the situation have been proposed. Balli et al. (2009) suggested the use of Clausius-Clapeyron equation (1.15) to the transition region only. Although simpler than graphical method, this approach is essentially the same, since by using the Clausius-Clapeyron equation in the transition region, one calculates the area that corresponds to Σ_1. Nevertheless, as already stated in section 1.2, the use of Clausius-Clapeyron equation neglects the second order contributions to entropy change.

Cui et al. (2010) elaborated on the method proposed by Liu et al.. The FM phase fraction usually increases gradually with temperature (and between consecutive magnetisa-

tion isotherms). In order to obtain a more realistic estimate, they used the FM fraction as a function of temperature to scale the FM and PM fractions of consecutive isotherms and calculate the entropy change of FM fraction (second order effects) as well as PM fraction (first order magnetic transition and related second order effects). A similar but numerical method using phase fractions was proposed by Das et al. (2010a,b).

Tocado et al. (2009) performed calorimetric measurement on MnAs (in the temperature-sweeping mode) confirming that such measurement shows no 'colossal' entropy change. The authors of that study used the heat capacity data to construct a comprehensive phase diagram of MnAs (figure 4.10), clearly showing the thermal and field hysteresis and point out that the magnetisation measurements in the hysteretic region are strongly path dependent. They attributed the 'colossal peak' to an extra contribution coming from the phase transformation of a FM fraction to PM on the heating between consecutive isotherms in zero field ($O \rightarrow O'$, figure 4.10). This is consistent with the statement of Liu et al. (2007). They formed their own model to calculate the extra contribution to entropy change based on heat capacity on heating and magnetisations of the coexisting phases. In order to avoid the extra contribution, they suggested taking isofield magnetisation measurements instead of isotherms. In that case, the state points in the hysteretic region of phase space are always PM on cooling or FM on heating. This approach was explored further by Caron et al. (2009).

The validity of making isofield measurements instead of isothermal ones can be justified by comparison of entropy change in MnAs measured by Wada and Tanabe (figure 4.1, using magnetisation isofields, no 'colossal' MCE) and von Ranke et al. (figure 4.7, using magnetisation isotherms, resulting in 'colossal' MCE). Caron et al. (2009) showed that 'non-colossal' MCE can be recovered when the isothermal magnetisation measurements are taken following a special protocol.

As an example, consider the phase diagram of $MnFeP_{0.8}Ge_{0.2}$ in figure 4.11. Usually, the magnetisation isotherms are taken at gradually increasing temperatures, starting in the low temperature FM state ('standard process'). Thus the sample is FM in the hysteresis

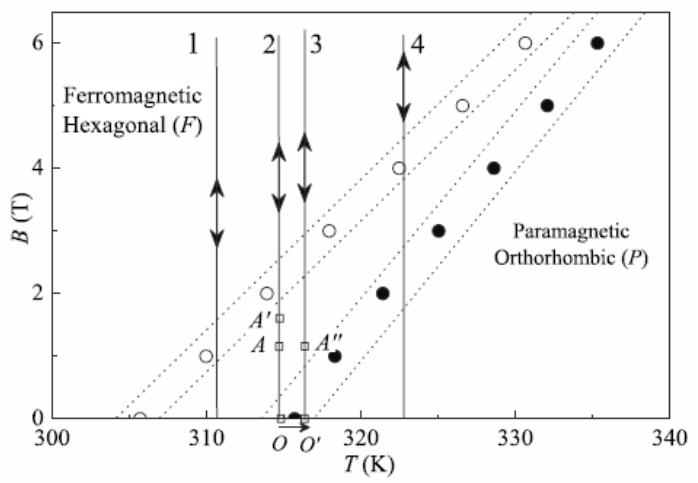


Figure 4.10 Magnetic phase diagram determined from heat capacity data of MnAs. Full circles show the FM to PM transition on heating, open circles show the PM to FM transition on cooling. The discontinuous lines show the finite width of the phase transition bands. Reprinted with permission from Tocado et al. (2009). Copyright 2009, AIP Publishing LLC.

region and does not transform upon field application until the isotherms reach the FM to PM phase line. The sample then becomes PM and transforms to FM state upon field application when reaching the PM to FM line, i.e. at very high fields. This results in a sudden large slope of the phase line constructed from the isotherms (stars in figure 4.11). Consistent with the Clausius-Clapeyron equation, an extremely large entropy change is deduced. The standard isotherms and corresponding entropy change as calculated using Maxwell relation are shown in figure 4.12.

Caron et al. proposed a so-called 'loop process' when the sample is heated to paramagnetic state before every isotherm. Thus, equivalent to the isofield process on cooling, the sample is always PM in the hysteresis region of the phase space (on increasing field). The sample can undergo the phase transition even at temperatures below the FM to PM phase line and a consistent slope of PM to FM phase line can be obtained from the isotherms ('+' signs in figure 4.11) down to low fields/temperatures. As follows from the Clausius-Clapeyron equation, a smaller entropy change is deduced in a wider temperature range.

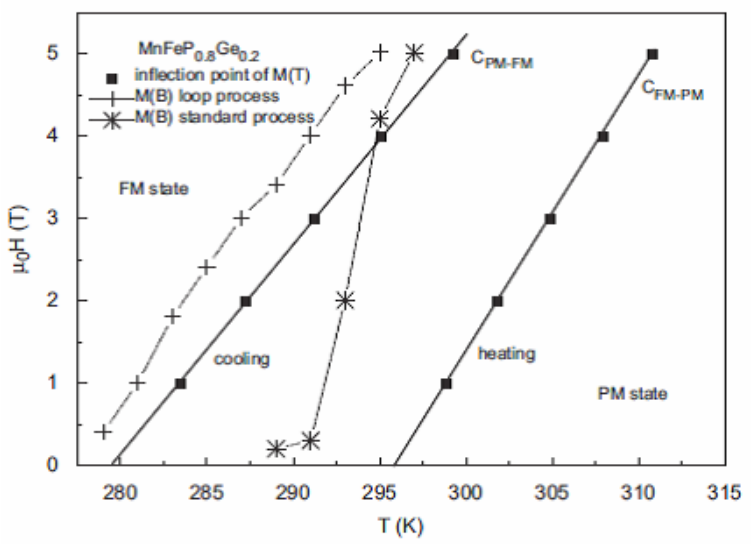


Figure 4.11 Magnetic phase diagram of $MnFeP_{0.8}Ge_{0.2}$. Phase lines derived from isofield magnetisation measurements (transition temperature set at half the maximum magnetisation value). (+) show the transition fields derived from isotherms in the 'loop process' and and (*) show the transition fields derived from isotherms in the 'standard process'. Reprinted from Caron et al. (2009), copyright 2009, with permission from Elsevier.

Isotherms for the same system measured using the loop process and the corresponding entropy change from Maxwell relation are shown in figure 4.13.

An important point to make is that, according to Caron et al., the entropy change in the 'colossal peak' is real, however, due to inconsistent probing of the PM to FM transition on increasing field, the entropy change over the full width of thermal hysteresis is artificially concentrated in a narrow region around the FM to PM transition in zero field. Furthermore the height of the spike is dependent on temperature step between isotherms. The spike is significant only when the temperature step is smaller than the thermal hysteresis.

This is consistent with the observation of 'colossal' MCE only in materials with large thermal hysteresis. As a matter of fact, a sign of this phenomenon can be seen even in the first report of giant MCE (see figure 1.7). However, the spike there is significantly smaller since the thermal hysteresis is only 2 K compared with 10 K in the case of MnAs.

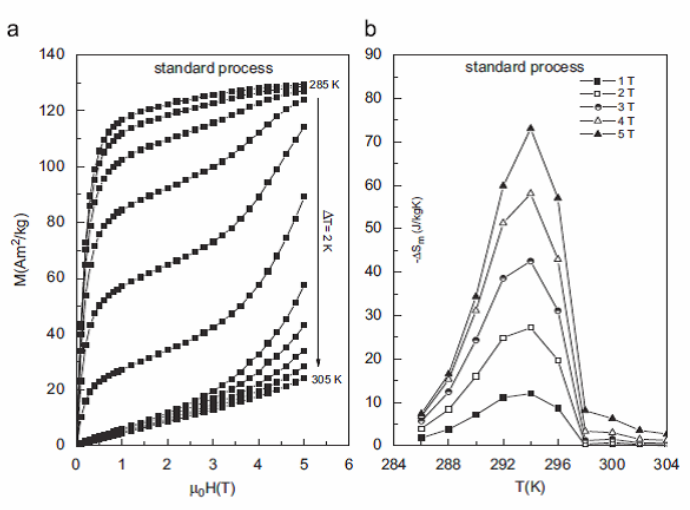


Figure 4.12 (a) Isothermal magnetisation curves of $MnFeP_{0.8}Ge_{0.2}$ on increasing field in the vicinity of the Curie temperature (standard process). (b) Magnetic entropy changes for different field variations as given by the Maxwell relation. Reprinted from Caron et al. (2009), copyright 2009, with permission from Elsevier.

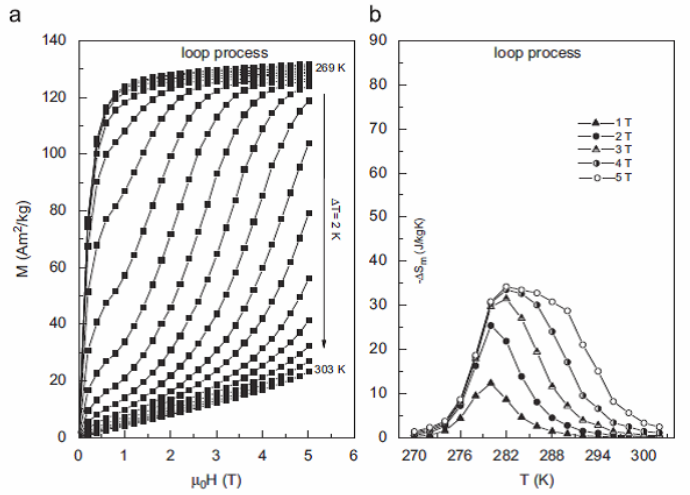


Figure 4.13 (a) Isothermal magnetisation curves of $MnFeP_{0.8}Ge_{0.2}$ on increasing field in the vicinity of the Curie temperature (loop process). (b) Magnetic entropy changes for different field variations as given by the Maxwell relation. Reprinted from Caron et al. (2009), copyright 2009, with permission from Elsevier.

These results also suggest that any data manipulation proposed to remove the 'colossal peak' does not reproduce the true shape of ΔS vs. T plot on increasing the field, losing the entropy change in the hysteresis region.

Nevertheless, it can be noted that even for the isofield magnetisation measurement there is a small spike in the entropy change estimated using Maxwell relation (figure 4.1). Although not 'colossal', this spike is not seen in calorimetric measurements of MnAs (Tocado et al., 2009). (Liu et al., 2007) considered this to be demonstration of the same phenomenon as the 'colossal spikes', however, in the light of what was said, this does not seem to be the case. Amaral and Amaral (2009, 2010) ascribed this to intrinsic limitations of Maxwell relation in application to hysteretic first order transitions.

Amaral and Amaral took into account the irreversibility of the phase transition and the existence of metastable states (stable states not corresponding to ground state) and their effects on the use of Maxwell relation, which by definition should not be valid. They used the Landau model of Gibbs free energy for first order magnetic phase transitions. The region of metastability, giving rise to hysteresis, arises due to two free energy minima. By considering the two minima, they defined limits of the metastability region, which can be considered as a kinetic limit in terms of observing the metastable states. They defined equilibrium states as the absolute minimum of free energy. The metastable limits were presented in analogy to increasing and decreasing field measurements (figure 4.14). They used the magnetisation isotherms determined from the model to calculate the isothermal entropy change and compare it with the entropy change as calculated using the temperature derivative of Gibbs free energy for the same paths (figure 4.15).

The results indicated that the Maxwell relation would underestimate the entropy change on increasing field (or cooling), and overestimate it on decreasing field (or heating). Similar results were obtained from a molecular mean-field model (Amaral and Amaral, 2010). The authors suggested that this could explain, for example, the small peak in entropy change measured by Wada and Tanabe, which was determined from isofield magnetisation data on heating (figure 4.1). Unfortunately, the entropy change is usually calculated only for

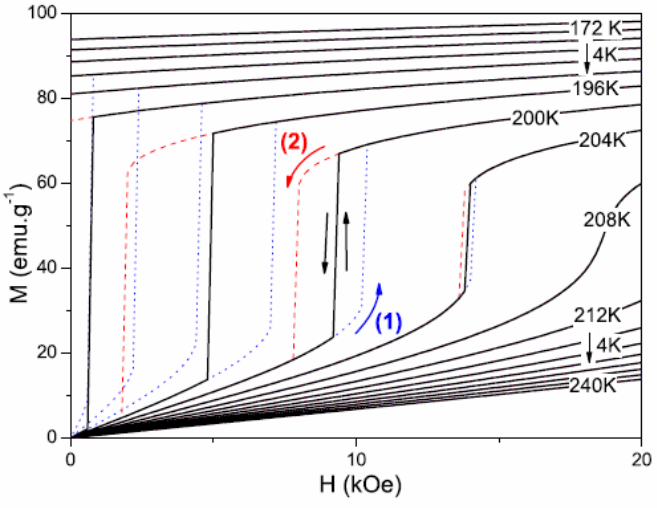


Figure 4.14 Magnetisation isotherms from Landau theory, for a first order transition through equilibrium states (solid lines) and through non-equilibrium (metastable) states on field increase and decrease (dotted and dashed lines respectively). Reprinted with permission from Amaral and Amaral (2009). Copyright 2009, AIP Publishing LLC.

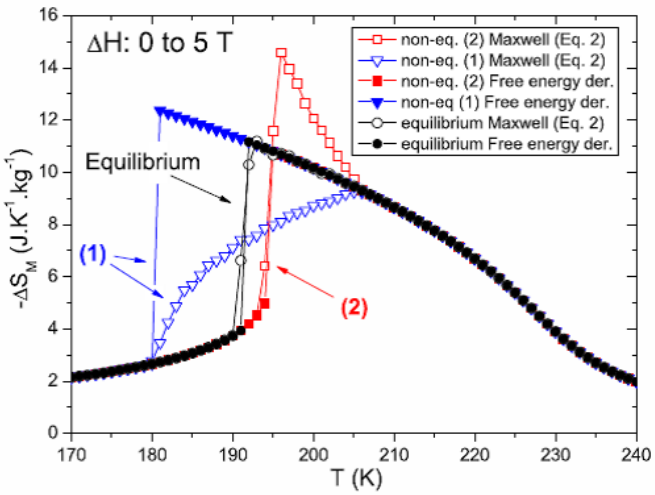


Figure 4.15 Isothermal entropy change for equilibrium and nonequilibrium solutions from Maxwell relation (opensymbols) and from free energy derivative (full symbols) for Landau theory M vs H data from 0 to 5 T. Reprinted with permission from Amaral and Amaral (2009). Copyright 2009, AIP Publishing LLC.

field increase (or isofield heating) assuming that it is consistent with field decrease (or cooling). Therefore this effect was not clearly demonstrated yet.

To conclude, there are several potential pitfalls related to the measurement of MCE in materials with a first order transition. The 'colossal' entropy change deduced by applying Maxwell relation to isothermal magnetisation data was disputed in the literature, on the grounds of comparison with calorimetric measurements. It was subsequently shown that an entropy change fairly consistent with the calorimetric data can be calculated from isofield magnetisation data but also from isothermal magnetisation data following a special thermal treatment between the isotherms. Nevertheless, it is important to realise that that the calorimetry data is usually taken in temperature-sweeping mode and that the entropy change calculated from isofield magnetisation data is more or less consistent with it. The question arises whether the 'colossal' entropy change can really be achieved by following a specific magnetisation history, or whether the concentration of entropy change from the hysteresis region is just artificial, as claimed by Caron et al. (2009). Before the work presented in the next section was undertaken, it seemed that the magnetisation history leading to 'colossal' entropy change as given by the Maxwell relation had not yet been reproduced in a calorimetric measurement. There were attempts to compare the entropy change from isothermal magnetisation measurements with calorimetric data taken in the field-sweeping mode (Wang et al., 2010). However, while those authors used the standard procedure for the isothermal magnetisation measurements leading to'colossal' MCE; they adopted the 'loop process' for the calorimetric measurement.

Here, one of the very hysteretic $Mn_{1-x}Fe_xAs$ compounds was studied. The standard isothermal magnetisation history was studied using magnetometry as well as microcalorimeter.

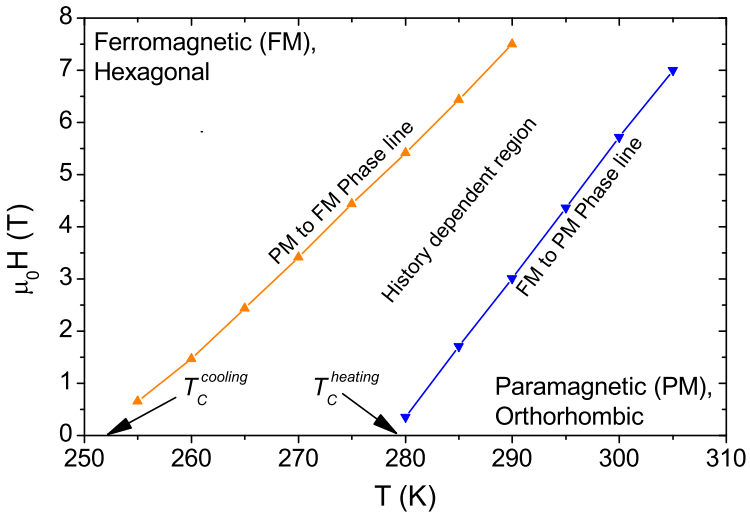


Figure 4.16 Phase diagram of $Mn_{0.985}Fe_{0.015}As$. The critical fields comprising the phase lines were determined from the peak in derivative of isothermal magnetisation measurements on field application for the PM to FM phase line and field removal for the FM to PM phaseline.

4.2 The sample — $Mn_{0.985}Fe_{0.015}As$

The choice of sample to study the 'colossal' MCE was determined by the temperature range of the microcalorimeter, which is limited to below 295 K. In order to make sure that the PM to FM transition can be reversed on heating, the only suitable candidate from the $Mn_{1-x}Fe_xAs$ series was the composition with $x = 0.015$. Figure 4.16 shows the $H-T$ phase diagram of the sample.

The sample was prepared by Ariana de Campos as described in de Campos et al. (2006):[1] *"First, a mother Fe-Mn alloy was arc melted under argon atmosphere. Each compound was then prepared with all the Fe coming from the mother alloy plus the appropriate amounts of pure Mn and As to complete the 1:1 'MnAs' stoichiometry. All materials were in pieces, and the total amount of each sample was 5 g. The materials sealed in a quartz tube under vacuum were heat treated in a resistive furnace at 1,070 °C for 2 h to assure the melting and thorough mixing of*

[1] Reprinted by permission from Macmillan Publishers Ltd: Nature Materials, copyright 2006.

the components, and were then quenched to room temperature. The tube containing the sample was then reheated to 800 °C for 48 h and subsequently water quenched to ambient temperature. Samples were characterized by metallographic analyses, X-ray diffraction and magnetic measurements before the measurements to determine the MCE were carried out. All Fe-doped samples formed a single phase, as shown by both metallography and X-ray diffraction, and confirmed by the magnetization as a function of temperature for a 0.02 T applied magnetic field."

From the temperature vs. composition phase diagram of the $Mn_{1-x}Fe_xAs$ (inset of figure 4.4) it can be seen that the chosen composition is in a very hysteretic region. According to Fjellvåg et al. (1988)[2] *"the sample with* $t = 0.015$ *is in a special position since the NiAs,F-type phase can be obtained close to* T_N *by exposing the sample to a strong magnetic field. On heating (in zero field) the thus induced NiAs,F-type phase transforms irreversibly into the MnP,P-type phase at* $T_{c,i} \approx 270$ *K,..."*

In the case of the particular sample studied here, an application of high field (8 T) at 220 K was necessary in order to fully convert the sample to the FM phase, however, the conversion to MnP-type PM phase on heating was then fully reversible by cooling. Presumably, the sample state in this composition range is very sensitive to the exact Fe content. The reversibility can be attributed to differences in sample preparation resulting in slight differences in composition and homogeneity. In order to ensure the FM ground state at low temperatures, all samples were pre-treated by applying 8 T at 220 K before any MCE measurements.

4.3 Magnetisation Measurements

Two magnetisation histories were studied — History A and History B. In History A the magnetic field (8 T) was applied and removed isothermally at temperatures starting from 295 K down to 265 K in 2.5 K steps. After each isothermal measurement the sample was cooled directly to the next measurement temperature. In History B the isothermal mea-

[2]Reprinted with permission from Elsevier, copyright 1988.

surements were performed from 295 K down to 230 K in steps of 5 K, however, after every magnetisation measurement the sample was reset to the PM state by heating it to 295 K before cooling to the next isothermal measurement temperature (in zero field). History B is equivalent to the loop process described in Caron et al. (2009) used to recover a non-colossal estimate of the isothermal entropy change from the Maxwell relation.

The magnetisation data for both histories are presented in figure 4.17a and 4.17b. History A features the characteristic plateaus around $T_C^{heating}$ and use of the Maxwell relation results in the 'colossal' MCE estimate in this temperature range (figure 4.17c). In History B, the entropy change concentrated in the 'colossal' peak for History A is distributed across the whole range of thermal hysteresis from $T_C^{cooling}$ to $T_C^{heating}$, yielding a non-colossal estimate of the MCE.

4.4 Measurements in Microcalorimeter

Since the microcalorimeter operates in a field-sweeping mode it can be used to reproduce both magnetisation histories ('A' and 'B') and directly observe the associated entropy change. The two magnetisation histories were repeated for the separate measurement of the latent heat and the heat capacity.

The same fragment ('fragment 1') was used to reproduce History A and History B. As already mentioned in section 2.3.3, the effective Seebeck coefficient of the thermopile (used in heat capacity measurement) is very sensitive to sample position and orientation. Because of the violent nature of the first order magnetostructural phase transition, the sample had to be fixed to the SiN membrane with GE varnish and the sample mass could not be measured afterwards. The specific values were obtained by comparison with another, pre-weighed fragment ('fragment 2').

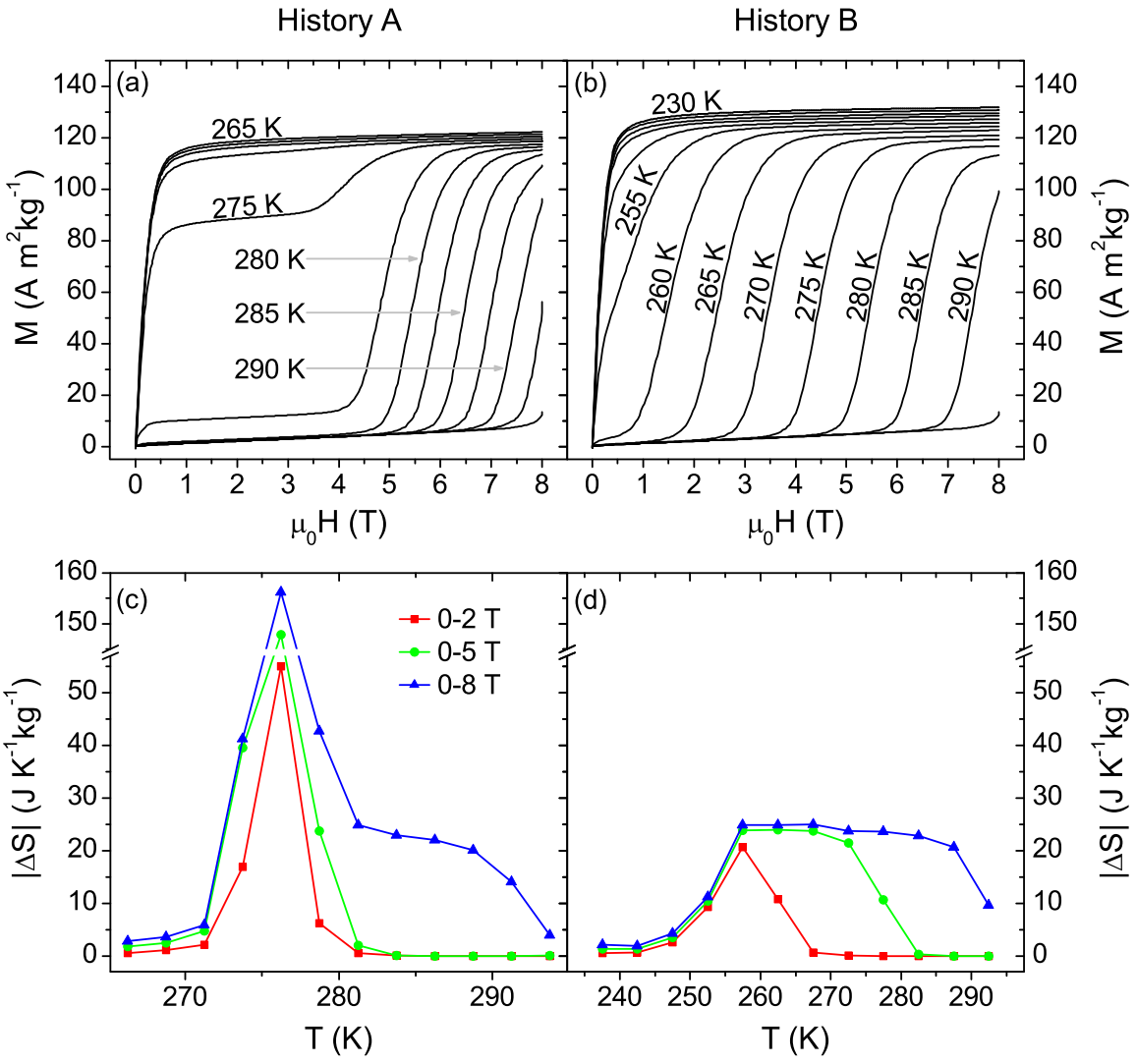


Figure 4.17 $Mn_{0.985}Fe_{0.015}As$ — bulk magnetometry data on field application (a, b) and isothermal entropy changes (c, d) as estimated by the Maxwell relation for History A and B, respectively. History A leads to the 'colossal' estimate of MCE, as indicated by the peak at ∼275 K.

4.4.1 Heat Capacity

Figure 4.18 shows a sample of the isothermal heat capacity measurements. A typical response of the FM and PM phase can be observed in the 287.5 K measurement. The PM state heat capacity appears field independent (within resolution), while the heat capacity of the FM state decreases with increasing field. Discontinuities in heat capacity are present at the FOPT (with some artefacts in form of randomly orientated spikes due to the release of latent heat). While there is a dominant step on field application (transition to the FM state), the reverse transition is more distributed in field. For the purposes of determining the heat capacity contributions (as described in section 3.2.2), a critical field was associated with the largest jump in heat capacity.

The measurements presented in figure 4.18 correspond to History A, in the temperature region where the 'colossal' effect has been reported. It can be noticed that on field removal at 285.0 K the sample reverts almost completely back to the PM state whereas at 282.5 K it seems to remain almost fully in the FM state. In calculating the heat capacity contribution it was assumed that the sample is fully paramagnetic on field application at 285.0 K and fully ferromagnetic on field application at 282.5 K. Importantly, the field dependence of heat capacity in History A does not display any unexpected features/critical behaviour that would be inconsistent with the analytical approach used.

The heat capacity contribution to isothermal entropy change from the low-field PM state is zero. This can be seen from the magnetometry estimates (figure 4.17c or d) at high temperatures and for small field variations (i.e. within the PM state). These estimates would form the high temperature reference point for the low field state in equation 3.10. Since there are no measurable field-induced changes in heat capacity (within the PM state), the integral in equation 3.10 also yields zero in the whole temperature range studied.

Thus, any second order contributions to entropy change come from the FM state only. These are given by equation 3.11:

$$\Delta S_{HC,HF}(T_{iso}) = \Delta S(T_{ref1}) + \int_{T_{ref1}}^{T_{iso}} \frac{\Delta C_{H_C \to H_2}(T)}{T} dT,$$

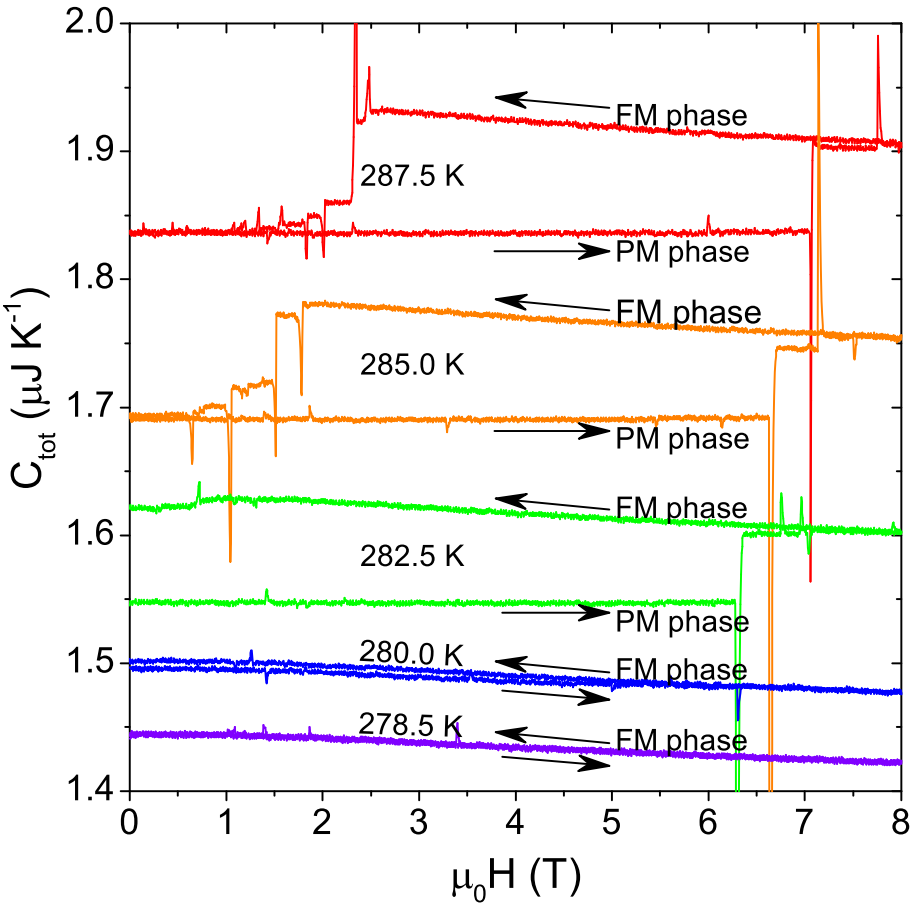


Figure 4.18 $Mn_{0.985}Fe_{0.015}As$ — selection of isothermal heat capacity measurements for History A (individual plots offset for clarity). At 287.5 K the phase transition can be induced and reversed within the maximum field range. A typical response of the PM and FM phase can be identified. While the PM heat capacity appears to be field independent (within instrument resolution), the heat capacity of the FM state reduces with increasing field. Randomly orientated spikes can be seen at discontinuities in heat capacity, which correspond to the FOPT. These are artefacts due to latent heat. The heat capacity itself shows no reproducible critical behaviour when approaching the FOPT. As one progresses along History A, a very small fraction of the sample appears to remain trapped in the FM state upon field removal at 285.0 K, where as this is the case for majority of the sample at 282.5. At 280.0 the sample exhibits predominantly FM response already on field application. No critical behaviour seems to be associated with History A compared with History B (e.g. at 280 K the heat capacity on field application and removal at for History A is equivalent to heat capacity on field removal for History B).

where H_C is the critical field at which the sample transforms to FM state (or the initial field of the initial sample state is FM) and H_2 is the maximum field applied. The reference entropy change, $\Delta S(T_{ref1})$, should be determined from magnetometry estimates at low temperature away from the FOPT. It should be possible to use any reference temperature provided that the field-induced changes are reversible within the relevant field range.

In order to maximise the accuracy of the reference point, the integral of $\Delta C/T$ (as a function of T) was fitted (by y-offset only) to multiple entropy change estimates from the magnetisation measurements. **It was the use of this procedure that revealed the necessity of a correction factor of 2 for the heat capacity measurement (first mentioned in section 2.3.6).** Figure 4.19 shows the fits for a selection of field variations. The integral without the correction factor is also plotted but cannot fit the temperature dependence of the isothermal entropy change.

The estimates from magnetisation measurement and the heat capacity contribution to entropy change should agree where the entropy change is not first order and therefore reversible (Maxwell relation can be used reliably). This is the case where the magnetometry estimates agree well on field application and removal. Technically the field induced changes can be considered reversible even within the hysteresis region up to the onset of the FOPT (provided a well defined initial state). Therefore, an agreement between the heat capacity and magnetometry can be observed in a wider temperature range for magnetometry estimates on field removal when the sample is ferromagnetic in the hysteresis region.

4.4.2 Latent Heat

An example of latent heat measurement is shown in figure 4.20. In a manner consistent with the observation in heat capacity measurement, the sample transforms to the FM state in fewer steps than to the PM state. In the former, one major latent heat peak can be observed. It splits into several smaller peaks on the reverse transition.

Note that the heat pulse calibration is usually performed for every single latent heat

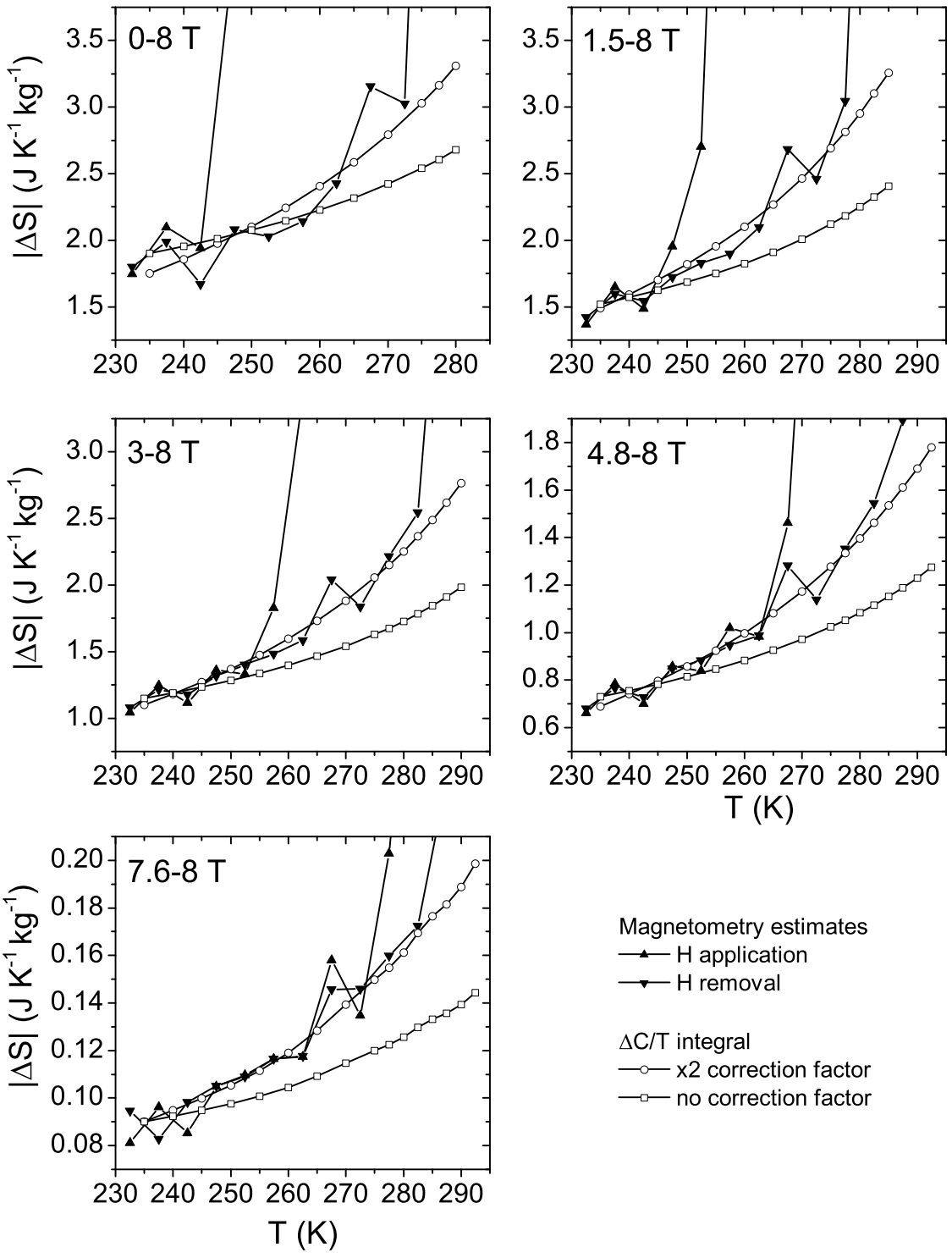


Figure 4.19 $Mn_{0.985}Fe_{0.015}As$ — reference point fitting for the heat capacity contribution to entropy change. A correction factor of 2 is necessary in order to fit the temperature dependence of the isothermal entropy change.

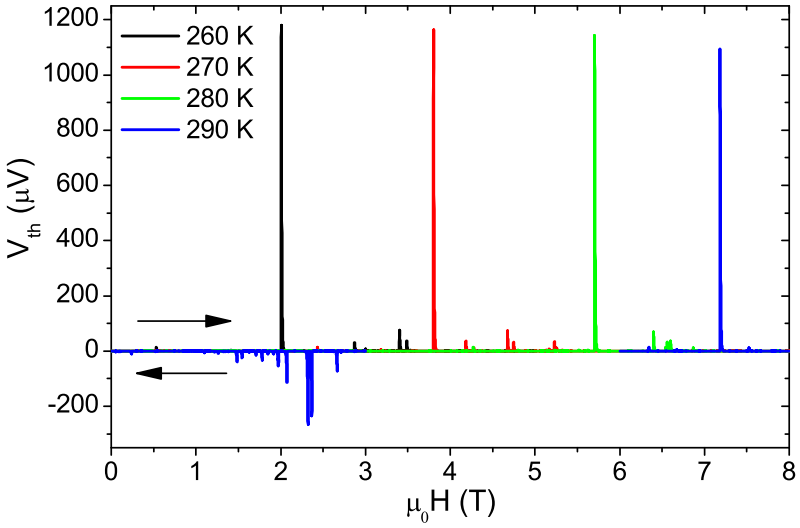


Figure 4.20 Latent heat measurement at various temperatures in $Mn_{0.985}Fe_{0.015}As$. Due to large hysteresis only the transition at 290 K is reversible.

measurement. It was avoided in the measurement of History A in order to accurately reproduce the thermomagnetic history, where the sample should be cooled from one isothermal measurement directly to the next. Heat pulse calibration would comprise an effective heating between the isothermal measurements. The calibration coefficients from the measurements for History B in the relevant temperature range were averaged and used instead.

4.4.3 Total Isothermal Entropy Change

The resulting total entropy changes for both histories (on field application) are shown in figure 4.21. The entropy change is dominated by latent heat (over 90%), as expected for a material with a strong first order phase transition. **No 'colossal' effect is observed in the direct calorimetric measurement.** History A simply restricts the entropy change to a temperature range above $T_C^{heating}$ where the phase transition is reversible upon field removal. Thus, the apparent entropy change concentration around $T_C^{heating}$ in History A is artificial.

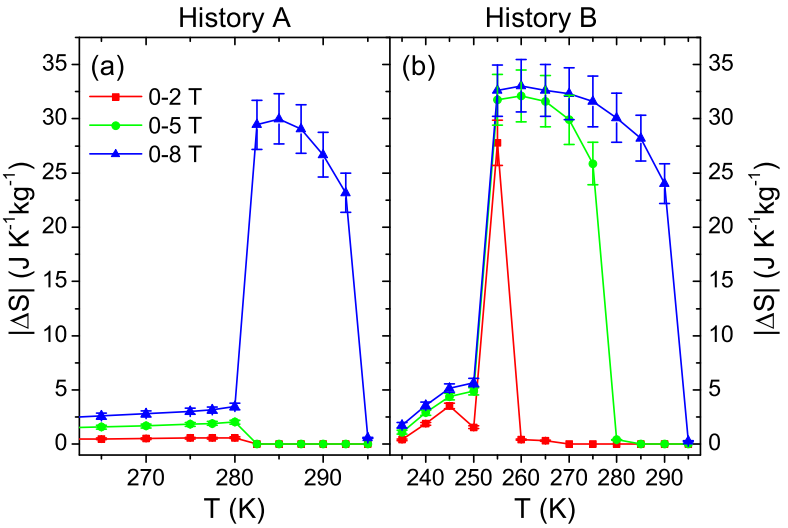


Figure 4.21 Total isothermal entropy change on field application as observed by microcalorimetry on fragment 1. History A (a) shows non-colossal MCE and simply restricts the large entropy change to a narrower temperature range when compared with History B (b).

4.4.4 Latent Heat in a Mixed-phase State

It is worth noting the sudden drop of entropy change from 282.5 K to 280.0 K in History A. This is due to no latent heat being observed at the lower temperature. It is consistent with a behaviour already inferred from the heat capacity measurements in figure 4.18 — while the sample starts from a mostly PM state at 282.5 K, it remains trapped in a fully FM state upon field removal at this temperature and no latent heat is observed on the next field application at 280.0 K. Thus, at these measurement temperatures, no significant mixed-phase state was induced in the sample.

While this observation is consistent with the analysis method used (assuming a digital FOPT/sample state), one might wonder whether that the 'colossal' entropy change is necessarily associated with the mixed-phase state (as it is a common feature in the magnetisation measurements in the temperature range with 'colossal' MCE estimates). To eliminate this possibility, a third magnetisation history was studied where the mixed-phase fraction

Table 4.1 Latent heat component of isothermal entropy change in a mixed-phase state at 295 K (fragment 2).

Step	ΔS_{LH} **[J K^{-1} kg^{-1}]**	**Relevant ratio [%]**
1: 0 to 8 T	+16.7 $\pm$ 1.1	
2: 8 to 0 T	-13.5 $\pm$ 0.9	
3: 0 to 8 T	+16.4 $\pm$ 1.1	
4: 8 to 3.27 T	-8.2 $\pm$ 0.5	61 $\pm$ 3 (of 2)
5: 3.27 to 8 T	+10.0 $\pm$ 0.7	61 $\pm$ 3 (of 3)
6: 8 to 0 T	-13.2$\pm$ 0.9	

was varied deliberately.

A measurement was performed on the pre-weighed fragment 2 at 295 K, at which temperature the PM state is well-defined at 0 T. Due to the slightly lower critical fields of this fragment, we observed one dominant latent heat spike just below 8 T even at 295 K. To vary the mixed-phase fraction, the fact that the reverse transition occurs in a cascade of smaller spikes can be utilised. At first the latent heat was observed upon field application (just below 8 T) and removal (at $\sim$3 T). The mixed-phase state was then set on the second — partial — field removal where the field removal was stopped roughly in the middle of the cascade (3.27 T). The fraction of the FM state converted back to the PM state was determined by comparing the latent heat with the previous (full) field removal. In the subsequent field application back to the maximum field the sample was driven through the first order phase transition in the mixed-phase state.

The measurement is summarised in Table 4.1. In step 4 a mixed-phase state was set by reverting only 61% of the FM phase induced in step 3. Upon the subsequent field application (step 5) 61% of the latent heat was observed as compared with the full field

application in step 3. Thus, **the latent heat on field application scales simply with the PM phase fraction**. No 'colossal' latent heat (entropy change) was observed when inducing the phase transition in a mixed-phase state.

Note that there is a large difference in the latent heat on field application and removal in a full magnetisation cycle (e.g. steps 1 and 2 in Table 4.1). This is a consequence of the large hysteresis and it is the subject of next chapter. The reproducibility of latent heat in steps 1 and 3 confirms that the transition is fully reversed in step 2. For phase fraction determination the change in the latent heat relative to a comparable process (e.g. partial field removal with respect to full field removal) was considered.

4.5 Summary

It this chapter it has been shown that while there are differences in the directly observed MCE due to thermomagnetic history, they do not amount to a 'colossal' MCE. This confirms that the concentration of entropy change resulting in the 'colossal' MCE, as given by the Maxwell relation, is artificial. It has also been shown that 'colossal' MCE cannot be observed by driving the sample through the phase transition in a mixed-phase state, as it has been confirmed quantitatively here that the first order contribution to the total entropy change scales with the phase fractions (Kuepferling et al., 2008). This validates various numerical and graphical approaches used to recover non-colossal MCE estimates from the magnetisation data using phase fractions, e.g. in Liu et al. (2007); Tocado et al. (2009); Balli et al. (2009); Cui et al. (2010); Das et al. (2010a).

Chapter 5

Further effects of hysteresis on the magnetocaloric effect

In this chapter more subtle issues related to irreversibility are studied. It will be shown that even if the 'colossal' artefact is avoided, other errors are present when using the Maxwell relation to estimate isothermal entropy change of a first order phase transition. These can be seen when comparing estimates on field application and removal as these yield a non-physical result upon field cycling. When the cycle is studied in the calorimetric measurement an entropy generation due to irreversible work is observed.

The effects of irreversibility were studied using a basic isothermal magnetisation/demagnetisation cycle fully crossing the hysteresis region. Outside of the hysteresis region the entropy and internal energy should be well-defined and single-valued functions of state. Thus, the isothermal entropy change of the sample should be equal but opposite in sign on field application and removal, irrespective of the fact that a region of irreversibility is crossed along the way.

Due to the hysteresis an irreversible magnetic work is done on the sample in the magnetisation/demagnetisation cycle. In order to maintain the sample entropy and internal energy as a function of state at the end of a cycle, the irreversible magnetic work has to be dissipated in form of heat, resulting in a positive heat flux from the sample into bath.

Thus, at the end of the cycle the entropy of the universe increases in the irreversible process while the entropy of the sample is maintained.

This should manifest itself differently in a material with conventional and inverse MCE. In the conventional MCE the entropy change is negative (heat expelled by the sample) on field application and positive (heat absorbed) on field removal. Thus, a heat flux due to irreversible work can superimpose constructively on field application and/or destructively on field removal. The opposite should be expected in a material with inverse MCE with a positive entropy change (heat absorbed) on field application and vice versa.

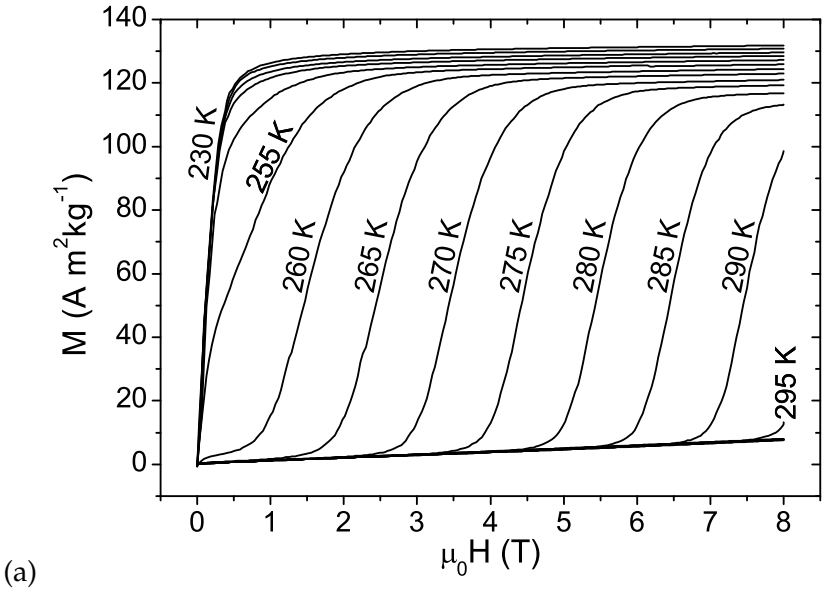
For this reason materials with conventional and inverse MCE were studied. For both, Maxwell estimates and calorimetric measurement on field application and removal were compared.

5.1 Irreversibility in conventional MCE

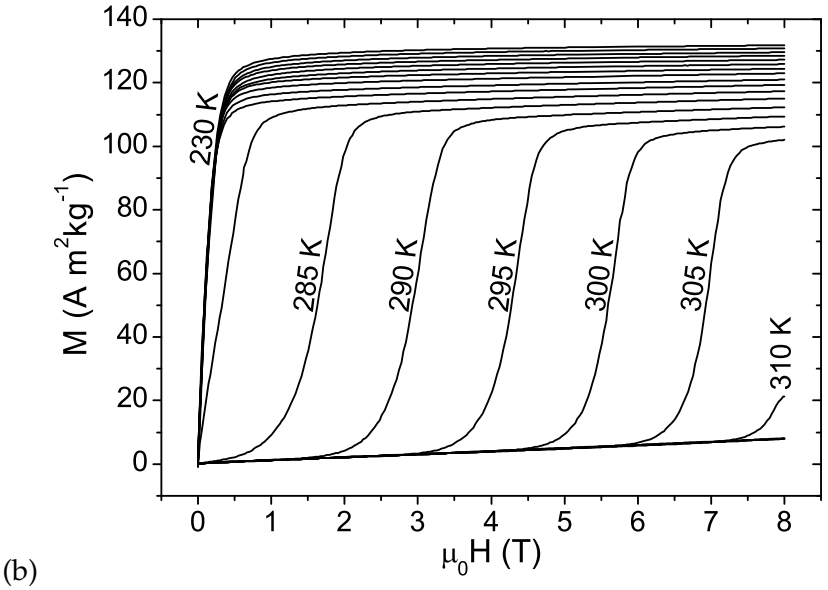
The sample used to study the 'colossal' artefact, $Mn_{0.985}Fe_{0.015}As$, was an ideal sample to study any other effects related to irreversibility simply due to the large thermal/field hysteresis. In fact, this study was triggered by the observation of a different latent heat on field application and removal, as already mentioned in the previous chapter.

5.1.1 Issues in magnetometry estimates beyond the 'colossal' artefact

The magnetisation measurements obtained for History B (avoiding the 'colossal' artefact on field application, see previous chapter) were extended to higher temperatures. The magnetisation data on field removal were taken in a manner so as to also avoid the 'colossal' artefact. On field removal the phase transition from FM to PM state is being probed. In order to probe the relevant phase line consistently, an initial FM state must be ensured within the hysteresis region at the maximum applied field (8 T). To do so the sample was always heated to the measurement temperature at the maximum field from a well defined FM state at 260 K.



(a)



(b)

Figure 5.1 Extended magnetisation data for $Mn_{0.985}Fe_{0.015}As$ on (a) field application and (b) removal. In order to avoid the 'colossal' artefact, a PM initial state was ensured on field application in the hysteresis region by cooling to the starting point from 295 K (at 0 T). Similarly, on field removal an initial FM state was ensured by heating to the measurement temperature from 260 K in the maximum field, 8 T.

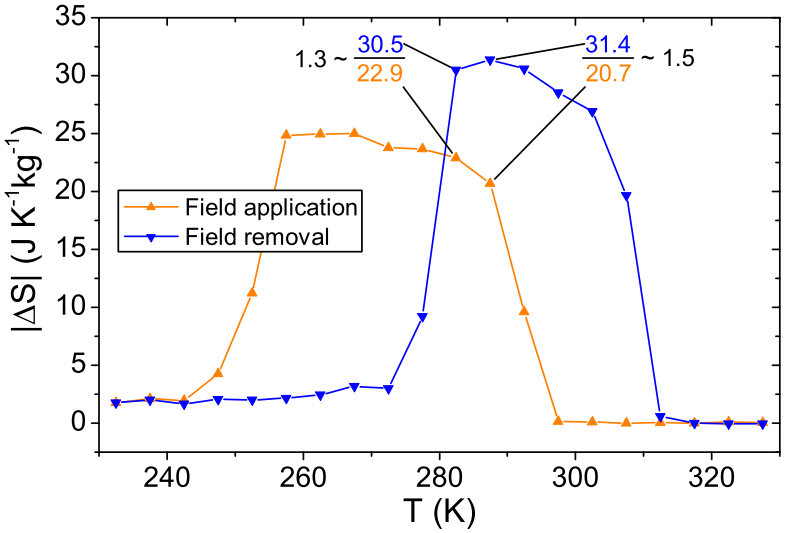


Figure 5.2 Isothermal entropy change estimates for from the magnetisation data presented in figure 5.1. The estimates correspond to a field variation between 0 and 8 T.

The resulting magnetisation data is presented in figure 5.1. The corresponding isothermal entropy change estimates via Maxwell relation are shown in figure 5.2. A large plateau characteristic of a FOPT can be observed on both field application and removal, however, due to the large thermal hysteresis they occur over different temperature ranges. Also, the two plateaus have significantly different heights. They overlap in a small window around ~ 285 K where the FOPT can be induced as well as reversed within the maximum applied field — the irreversibility region can be fully crossed.

Due to the differing heights of the plateaus, the entropy change estimate is significantly larger on field removal even within this window. This observation is consistent with the model of Amaral and Amaral (2009), figures 4.14 and 4.15. The model shows, however, that the actual entropy change (as given by the derivative of free energy) should be the same on field application and removal. The same result was implied by the simple thermodynamic consideration discussed in the beginning of this chapter.

The result given by Maxwell relation is completely non-physical. Consider a cyclical field application (up to 8 T) and removal at 285 K. Since the entropy change is negative

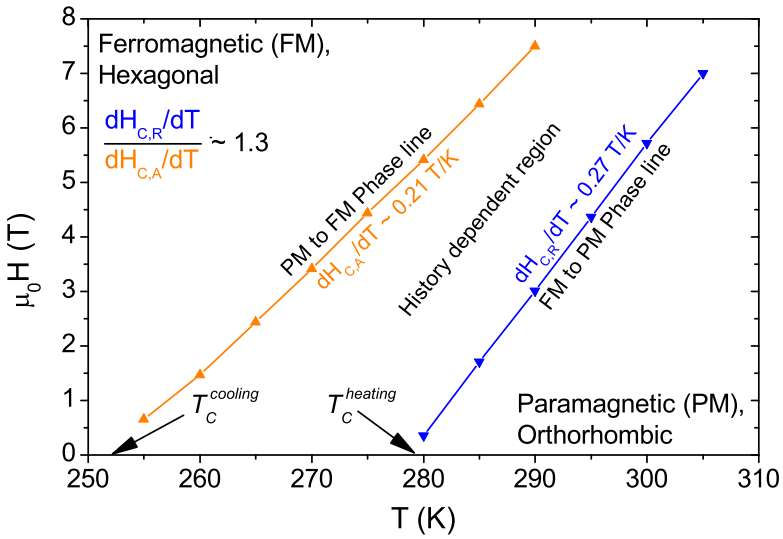


Figure 5.3 Phase diagram of $Mn_{0.985}Fe_{0.015}As$. The slopes of the phase lines indicate that the isothermal entropy change (as estimated using a Clausius-Clapeyron equation) should by 30% larger on field removal when the transition occurs at the steeper phase line.

on field application (heat flow out of the sample) and positive on field removal (heat flow into the sample), a larger entropy change on field removal corresponds to a net heat flux into the sample per each cycle. In an isothermal cycle this would imply a full conversion of heat into work in order to maintain the functions of state at the end of the cycle. This violates the *second law of thermodynamics*, reducing the entropy of the universe.

The same result is obtained via Clausius-Clapeyron equation (1.15)

$$\Delta S = -\Delta M \frac{dH_c}{dT},$$

where ΔM is the (discontinous) change in magnetisation at the FOPT and $\frac{dH_c}{dT}$ is the slope of the first order phase line. Since the difference in magnetisation change on field application and removal is negligible, the relative difference in entropy change estimated via Clausius-Clapeyron is given by the slopes of the relevant phase lines. The phase diagram of $Mn_{0.985}Fe_{0.015}As$ is revisited in figure 5.3 and the slopes of the phase lines are indicated. The slope of the FM to PM phase line (probed on field removal) is approximately 30%

larger.

The Maxwell estimates suggest that the entropy change on field application should be $\sim 40\%$ larger on field removal (for a fully crossed FOPT on both, field application and removal). This is indicated in figure 5.1. The ratio at 282.5 K (1.3) is slightly underestimated (compared to a full transformation at the FOPT) since the magnetisation isotherm on field removal at 280 K (used for the estimate at 282.5 K together with the 285 K isotherm) did not fully cross the FOPT (see figure 5.1 b). On the other hand, the ratio at 287.5 K (1.5) is slightly overestimated since here the isotherm on field application at 290 K did not fully cross the FOPT (see figure 5.1 a).

Thus, the Maxwell relation and the Clausius-Clapeyron equation both estimate larger entropy change on field removal by a comparable margin, approximately 40% and 30%, respectively. Since the Clausius-Clapeyron equation can estimate only the first order contribution, it confirms that the origin of these non-physical estimates is related to the first order nature of the phase transition.

It is worth noting that for this anomaly to be significant, the magnitude of the hysteresis does not need be very large but only very **temperature dependent**. This follows from the consideration of Clausius-Clapeyron equation — it is the temperature dependence of hysteresis that implies a difference in slope of the two phase lines corresponding to the FOPT. Parallel slopes should result in similar estimates on field application and removal. In the next section, the Maxwell estimates will be compared with the measurements in microcalorimetry.

5.1.2 Comparison with calorimetry

In the calorimeter the irreversibility of the FOPT was studied at 290 K. The temperature was chosen because of the large thermal hysteresis and a finite distribution of the FOPT in field (i.e. the presence of multiple steps/spikes in the heat capacity/latent heat measurement). Because of this, there was no temperature where a 100% FM state could be induced by applying the maximum field (8 T) and then completely and reliably reversed to 100%

Table 5.1 Repeated latent heat measurement at 290 K.

Measurement	$\Delta S_{LH\uparrow}$	$\Delta S_{LH\downarrow}$	$\Delta S_{LH\uparrow} + \Delta S_{LH\downarrow}$
		($J\,K^{-1}\,kg^{-1}$)	
1	-21.3	18.0	3.3
2	-23.2	18.4	4.8
3	-24.2	20.2	4.0
4	-23.8	19.6	4.2
Avg $\pm$ St.dev.	23.1 ± 1.3	19.0 ± 1.0	4.1 ± 0.6
Scaled (/0.87)	26.6 ± 1.5	21.9 ± 1.2	4.7 ± 0.7

PM state on field removal.

At 290 K there is a well-defined PM state at zero field, thus ensuring full reversibility of any FM phase fraction induced on field application. It can be seen in figure 4.20 that on field application a group of smaller latent heat peaks usually follows one dominant peak. These are not seen at 290 K. Since the smaller peaks correspond to approximately 13% of the total latent heat, the FM phase fraction induced at 290 K was estimated to be 87%. The latent heat measurements were scaled up accordingly for a best estimate of latent heat corresponding to a full phase transition. The latent heat measurement was repeated 4 times and the results are shown in table 5.1.

Note that based on the discussion of errors of the latent heat measurement, at a given temperature a precision better than $\pm 0.3\,J\,K^{-1}\,kg^{-1}$ was expected. The standard deviation of the multiple measurements (table 5.1) is several times larger. This could be attributed to two factors — a varying FM phase fraction induced on the subsequent field applications and a drift of the bath temperature during the measurement.[1] Only the latter should affect

[1] In a way consistent with a thermal drift, the critical fields were observed to reduce gradually in subsequent measurements (not below critical fields corresponding to 287.5 K). The thermal drift was attributed to a change in thermal balance of the probe when the sample space was evacuated for the latent heat measurement. This

the difference in latent heat observed on a subsequent field application and removal. This is consistent with a lower standard deviation observed for the difference in latent heat (see table 5.1).

The heat capacity contribution (FM state only) was integrated from a low temperature reference point. Thus, the reference point as well as most of the integrated heat capacity changes were measured in a fully FM state. The measured heat capacity contribution should therefore correspond to a full FM state without any scaling. The reference point fitting for the relevant critical fields at 290 K (7.6 T on field application and 3 T on field removal) has been shown in figure 4.19.

The total entropy change on field application and removal is presented in figure 5.4, where it is compared with the estimates via Maxwell relation. As is consistent with the model of Amaral and Amaral (2009), the calorimetric measurements show an entropy change magnitude somewhere between the estimates given by Maxwell relation on field application and removal. The measurement error (in this case dominated by the error in mass, 7%, and the standard deviation of the repeated latent heat measurement, 6%) is, however, too large to say so conclusively.

A difference between field application and removal is observed even within the calorimetric measurement, however, this is much smaller and of an opposite sense compared with the Maxwell estimates. The net difference of $-2.1 \pm 0.8\ \mathrm{J\,K^{-1}\,kg^{-1}}$ corresponds to a net heat of $620 \pm 230\ \mathrm{J\,kg^{-1}}$ expelled per field application/removal cycle.[2]

This heat dissipation can be accounted for by considering the irreversible magnetic work done in the hysteretic magnetisation cycle, as discussed in the beginning of the chapter. The magnetisation loops at 290 K and 285 K are shown in figure 5.5. The area of the

effect was later reduced by improving the heat sinking of the probe and thus reducing the effect of helium exchange gas on the thermal balance.

[2]Note that the absolute error of the entropy change difference is smaller than that of the entropy change on field application and removal presented in figure 5.4. This is because the relative errors, such as in sample mass have to be included only after a sum/difference (of high precision measurements made on the same sample) has been taken.

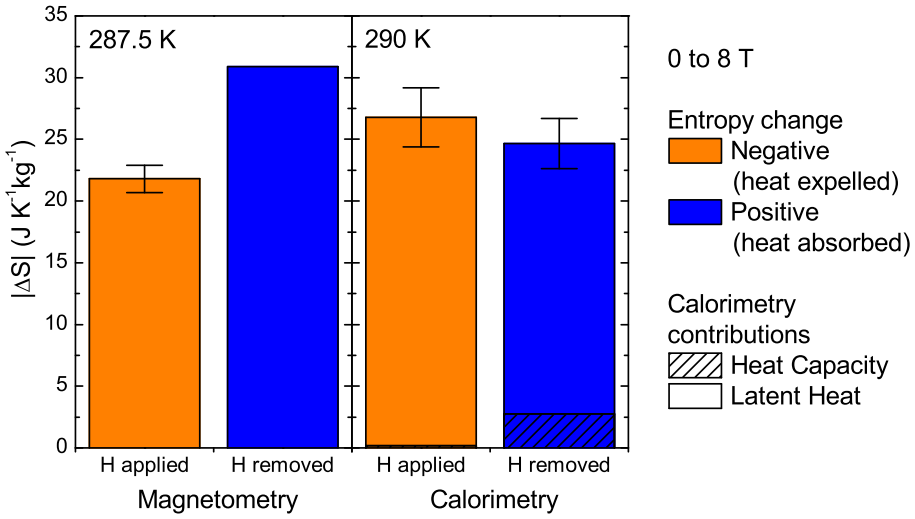


Figure 5.4 Comparison of the effects of irreversibility in magnetometry estimates and calorimetry. The lower error bounds in the magnetometry estimate on field application correspond to the actual estimate from the data for 287.5 K (probably underestimated since the phase transition was not fully crossed at the 290 K isotherm). The estimate for 282.5 K should form a reliable upper bound on the Maxwell estimate for a complete FOPT on field applicaton. The calorimetric measurements lie within the spread of the magnetometry estimates. A difference between field application and removal is observed even within the calorimetric measurement, however it is much smaller and in the opposite sense.

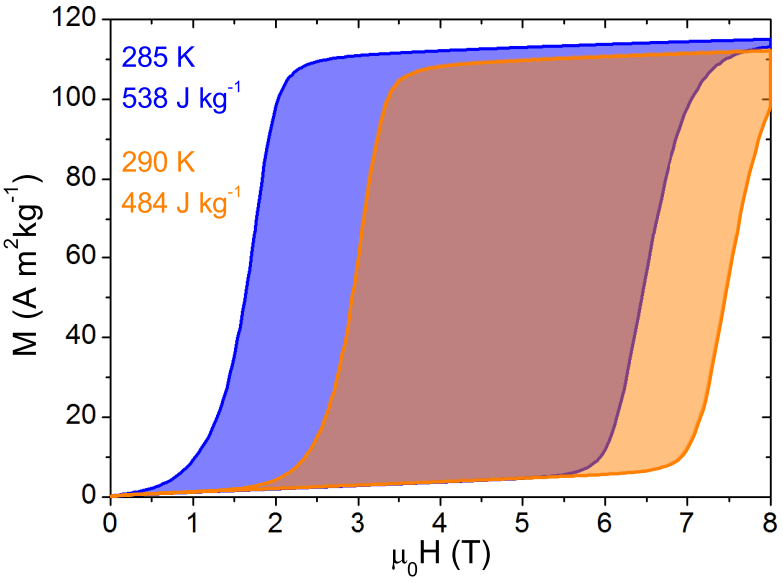


Figure 5.5 Hysteresis loss in an isothermal magnetisation loop in $Mn_{0.985}Fe_{0.015}As$ at 285 K and 290 K.

magnetisation loop at 290 K corresponds to an irreversible work of 484 J kg^{-1}, however, the transformation is not fully complete on field application. At 285 K the irreversible work estimate (538 J kg^{-1}) should be more representative of a full transformation. Based on the difference in hysteresis width and height between 290 K and 285 K, the full transformation hysteresis loss at 290 K can be estimated to be 500 ± 5 J kg^{-1}.

The net irreversible magnetic work done on the sample per cycle agrees within error with the net heat expelled by the sample as observed in the calorimeter. Thus, rather than a net reduction of sample entropy upon cycling (which would also be non-physical), **the calorimeter appears to measure an additional heat flux, which corresponds to the dissipation of irreversible magnetic work**. This heat flux increases the entropy of the bath — entropy is generated in the irreversible process.

It is also worth noting the difference in heat capacity contribution between field application and removal (figure 5.4). This is due to the fact that on field application the sample is in the PM state within the hysteresis region, and therefore there is no entropy change

over the corresponding field variation. On field removal, however, the sample is in the FM state within the hysteresis region with a finite continuous entropy change.

This also explains why the ratio of Maxwell estimates on field removal and application (~ 1.4) appears marginally larger than the estimate by Clausius-Clapeyron equation (~ 1.3). The former includes the continuous contribution to entropy change within the hysteresis region, which is present only on field removal.

5.2 Irreversibility in inverse MCE

5.2.1 The sample — CoMnSi

CoMnSi undergoes a metamagnetic transition from a helical noncollinear antiferromagnetic (AFM) state to a *high magnetisation* (HM) state. Thus, unlike in the conventional MCE, the application of magnetic field induces a lower order/higher entropy state. In an adiabatic field application the lattice compensates for the increase of magnetic entropy and the sample cools down.

The sample was prepared by Karl Sandeman as described in Sandeman et al. (2006), by induction melting pieces of Mn, Co and Si in 1 bar of argon. The sample was annealed at 1223 K for 60 h and slowly cooled to room temperature at a rate of 0.2 K per minute. Single-phase was confirmed in powder X-ray diffraction at room temperature showing only an orthorhombic (*Pnma*) phase. Scanning electron microscopy did not reveal any secondary phase either.

A phase diagram based on the magnetisation data measured here is presented in figure 5.6. The metamagnetic phase transition is second order (no hysteresis) at high temperatures, however there is a tricritical point below which the metamagnetic transition couples to changes in the nearest-neighbour Mn-Mn separation and the transition becomes first order (Barcza et al., 2013). Compared with the magnetostructural transition in MnAs, the magnetoelastic coupling here is associated with a much lower field hysteresis.

Importantly, the presence of a tricritical point and an onset of hysteresis below it im-

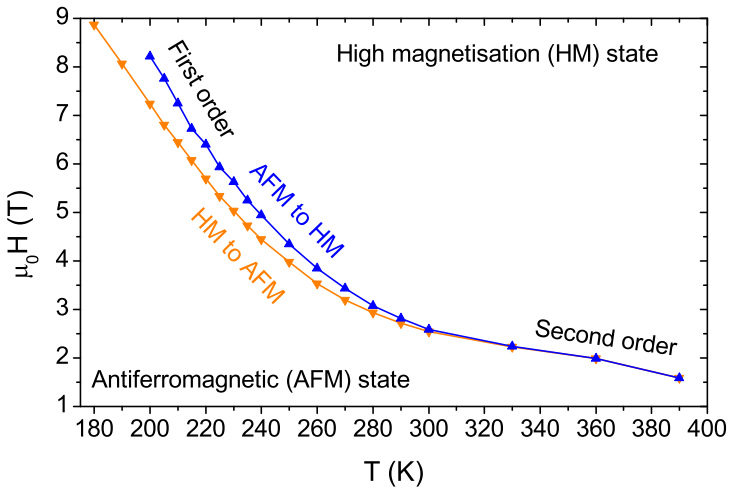
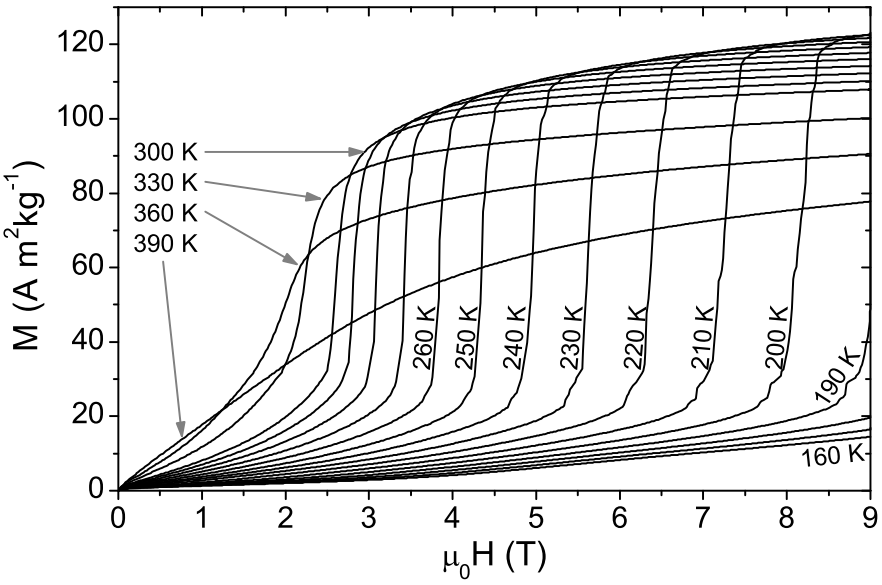


Figure 5.6 Phase diagram of CoMnSi. The critical fields comprising the phase lines were determined by the peak in the first derivative of the magnetisation (figure 5.7) on field application for the AFM to HM phase line and on field removal for the HM to AFM phase line.

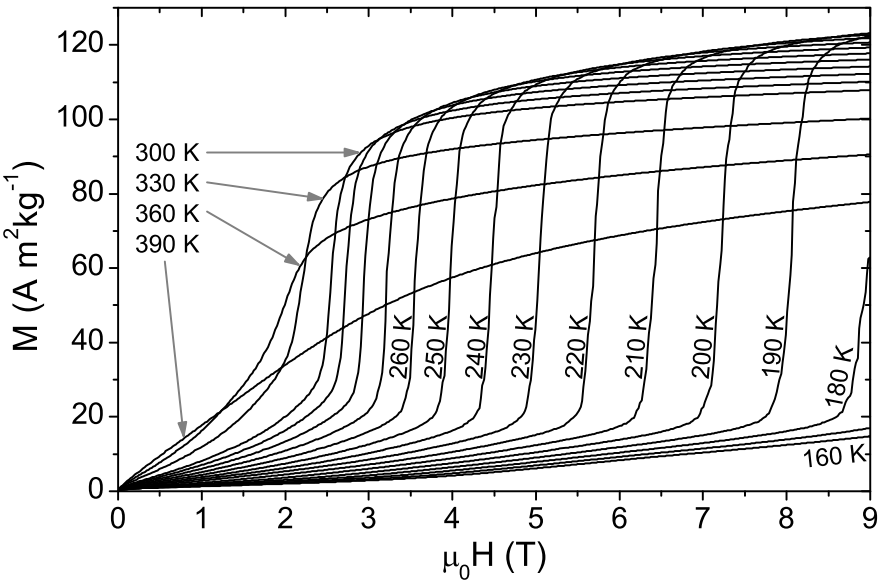
plicate differing slopes of the two first order phase lines. It can be seen from the phase diagram (figure 5.6) that the field hysteresis increases with decreasing temperature and that the slope of the AFM to HM phase line (probed on field application) is larger than the HM to AFM phase line (field removal). Thus, the Maxwell relation should estimate larger entropy change on field application, contrary to the case of $Mn_{0.985}Fe_{0.015}As$ with larger estimate on field removal.

5.2.2 Magnetometry estimates

The magnetisation measurements on CoMnSi are shown in figure 5.7. The corresponding isothermal entropy changes estimated via Maxwell relation are presented in figure 5.8. As expected the estimates of entropy change are larger on field application. Again, such a result is non-physical, corresponding to a net heat absorbed by the sample in a magnetisation/demagnetisation cycle at a constant temperature.



(a)



(b)

Figure 5.7 Magnetisation data for CoMnSi on field (a) application and (b) removal. Since the sample does not exhibit an FOPT/hysteresis at zero field, the isotherms on field application always have a well-defined initial state. On field removal an initial HM state was ensured in the hysteresis region by cooling to the measurement temperature from a well-defined HM state, at the maximum field.

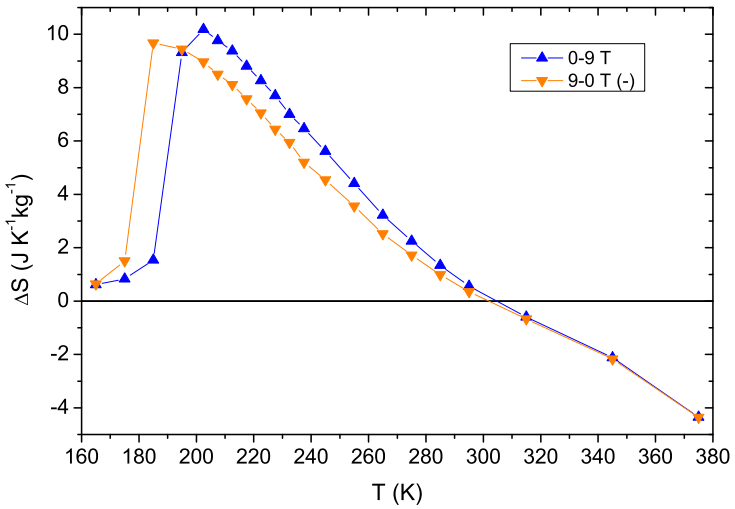


Figure 5.8 Estimates of isothermal entropy change in CoMnSi (field variation 0 to 9 T and reverse) estimated from magnetisation data using Maxwell relation.

5.2.3 Irreversibility in calorimetry

To check the effect of irreversibility in the calorimetry, the measurement was focused on low temperatures where the magnitude of field hysteresis is largest. The isothermal entropy change was studied primarily at 217.5 K and an additional measurement was taken at 227.5 K.

Figure 5.9 shows an example of heat capacity measurement in CoMnSi. A hysteretic FOPT can be distinguished at the discontinuities in heat capacity. Unlike in $Mn_{0.985}Fe_{0.015}As$, field induced changes in heat capacity can be observed in both the low field and high field state. Thus, the heat capacity contribution had to be evaluated for both states. In line with the analysis described in section 3.2.2 the low field state (AFM) contribution was integrated from a low temperature reference point ($\sim$ 190 K) and the high field state (HM) contribution was integrated from a high temperature reference point ($\sim$ 240 K) so that neither of the integrals crosses a first order phase line. Note that the high temperature reference point is non-ideal as it is quite close to the measurement temperatures and therefore the FOPT. The reference point had to be used because Apiezon-N grease was used as an adhesive.

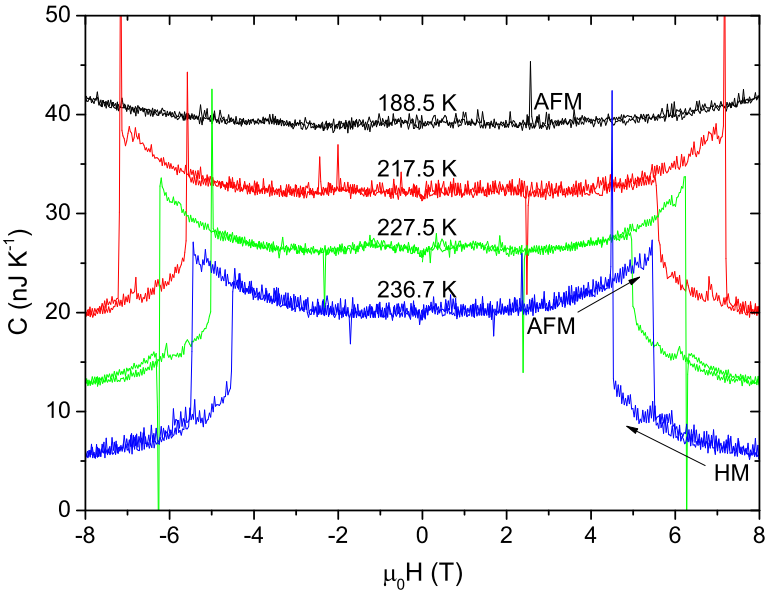
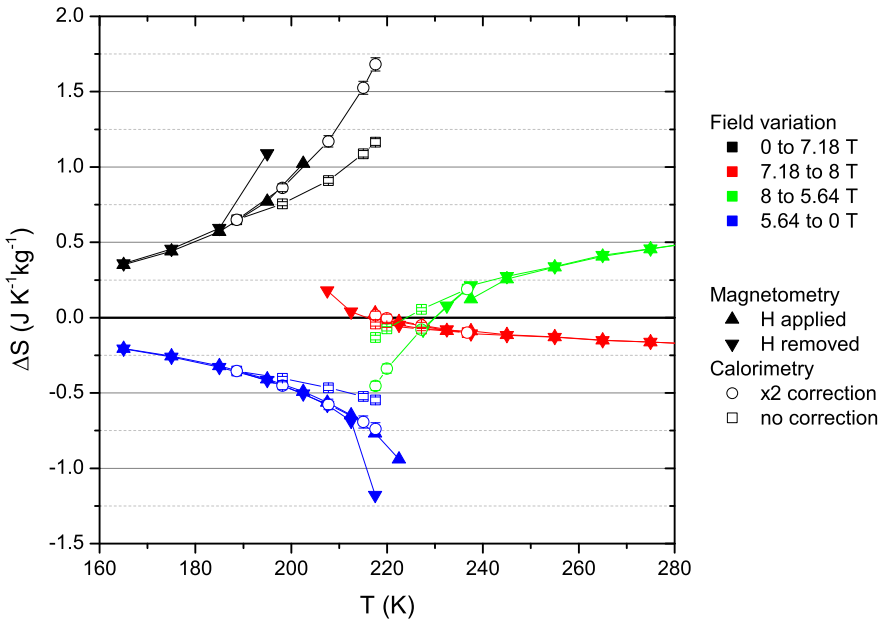


Figure 5.9 Heat capacity measurement in CoMnSi. Plots at different temperatures are offset for clarity.

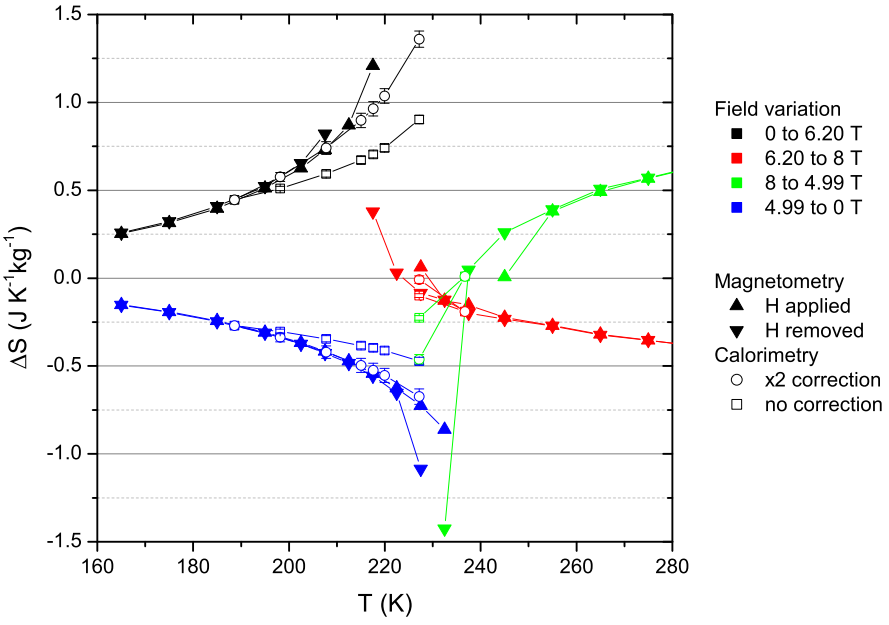
Due to sample movement, no reproducible measurements were obtained above the glass transition of the grease.

The fitting of reference points for the heat capacity contributions is shown in figure 5.10. **Note that as in $Mn_{0.985}Fe_{0.015}As$, a correction factor of 2 had to be applied in order to be able to fit the temperature dependence of the continuous entropy changes with the $\Delta C/T$ integral.** With the correction factor a very good fit is obtained resulting in a very small estimated uncertainty in the reference points (± 0.01 J K^{-1} kg^{-1}), except for the case of the high field contribution at 227.5 K where an error of ± 0.1 J K^{-1} kg^{-1} was assumed due to the proximity of the FOPT. The latent heat measurement was repeated 4 times at 217.5 K. The reproducibility of the measured latent heat was within $\pm 1\%$ and consistent with the precision expected from baseline noise. The latent heat measurement is shown in figure 5.11.

The total entropy changes on field application and removal are shown in figure 5.12. Note that the level of entropy change measured in the calorimeter appears systematically



(a)



(b)

Figure 5.10 Fitting of reference points in CoMnSi at (a) 217.5 K and (b) 227.5 K. Correction factor of 2 had to be applied to heat capacity data in order to fit the temperature dependence of the continuous entropy changes. Only one integration step could be performed for high field contributions at 227.5 K. Therefore, an order of magnitude larger uncertainty in reference point was assumed.

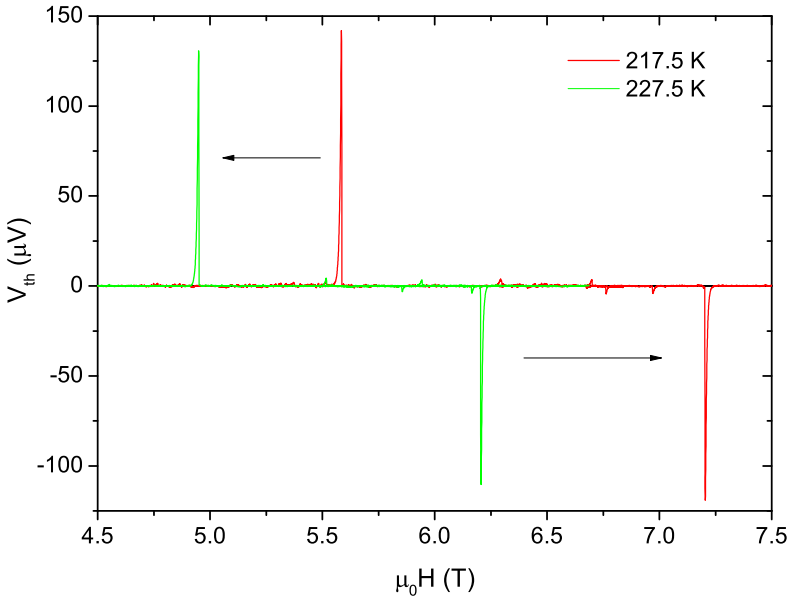


Figure 5.11 The latent heat measurement in CoMnSi. The phase transition is dominated by a single peak but several smaller peaks are also present.

below the estimates (on both field application and removal) from magnetometry. One may expect the actual entropy change to be between the two estimates. A possible explanation might be in the differences between fragment and bulk. At 217.5 K, the transition in the fragment studied here exhibits field hysteresis width 1.5 T whereas it is only 0.7 T in the bulk.

Nevertheless, as expected, the calorimetric measurements show larger entropy change on field removal, which is consistent with a net heat expelled by the sample per cycle. The measured differences are compared with hysteresis loss (in a magnetisation loop) in table 5.2. At both measurement temperatures the fragment exhibits twice as large field hysteresis as the bulk. Consequently the effect of irreversible work may be expected to be twice as large but still only about 100 J kg^{-1}, which is significantly smaller than in the case of $Mn_{0.985}Fe_{0.015}As$. Measurement of such a small net heat flux approaches the current precision limit of the microcalorimeter. Nevertheless, **a net heat expelled was observed at both temperatures and it is comparable with the irreversible work as given by the**

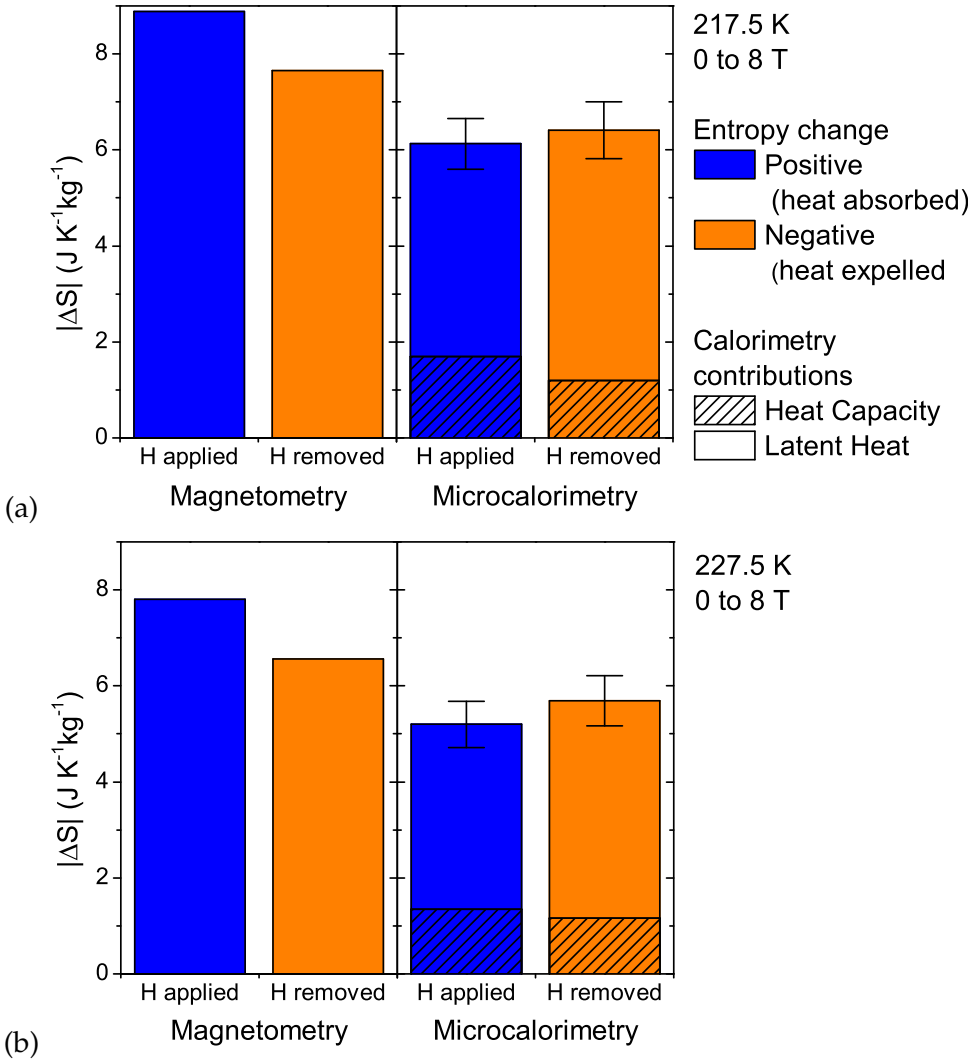


Figure 5.12 Comparison of irreversibility effects in magnetometry and calorimetry in CoMnSi. Calorimetry measures larger entropy change on field removal, corresponding to a net heat expelled per cycle.

Table 5.2 Comparison of the net heat expelled in the calorimetric measurement and the irreversible magnetic work as given by a hysteretic mangetisation loop.

	Calorimetry (fragment)		Magnetometry (bulk)	
T (K)	Net heat expelled ($\mathrm{J\,kg^{-1}}$)	Hysteresis (T)	Irreversible magnetic work ($\mathrm{J\,kg^{-1}}$)	Hysteresis (T)
217.5	61 ± 27	1.5	68	0.7
227.5	112 ± 43	1.2	56	0.6

(bulk) magnetisation loop.

The results presented here are consistent (although not conclusively, due to relatively large measurement error) with the full irreversible heat being measured by the calorimeter. It is worth pointing out that it should be possible to measure such an irreversible heat only in the latent probe. This may pin down the moment of the dissipation of the irreversible work to the moment of the release of latent heat at the first order phase transition.

5.3 Summary

It was shown that the use of Maxwell relation as well as Clausius-Clapeyron equation can lead to erroneous estimates of isothermal entropy change in systems with temperature dependent hysteresis. These are apparent when comparing estimates on field application and removal and result in a non-physical difference between the two. This effect is beyond and above the 'colossal' artefact. It is linked to the slope of a hysteretic first order phase line and it cannot be avoided by any particular magnetisation history. It forms an intrinsic limitation of the use Maxwell relation, which assumes equilibrium thermodynamics, when applied to hysteretic systems.

An apparent difference in entropy change on field application and removal was observed also in the direct calorimetric measurement, however, this was smaller and in op-

posite sense. It was attributed to the dissipation of irreversible magnetic work performed on the sample in the hysteretic magnetisation/demagnetisation cycle.

Both observations were confirmed in two systems with fundamentally different manifestation of the MCE. A material with conventional MCE ($Mn_{0.985}Fe_{0.015}As$) and a material with inverse MCE (CoMnSi).

Chapter 6

Conclusions

In this thesis the magnetocaloric effect (MCE) at a first order phase transition (FOPT) has been studied with a focus on hysteresis and irreversibility related effects. Two methods of determining the MCE have been used and compared:

- an indirect estimation of MCE from magnetisation measurements via a Maxwell relation — a commonly used technique for primary sample characterisation
- a direct calorimetric measurement of MCE in a microcalorimter — a unique tool enabling a separate measurement of latent heat and heat capacity

The application of Maxwell relation in very hysteretic first order systems has led to reports in the literature of 'colossal' MCE, which were later widely disputed. Other reports have shown that a non-colossal estimate can be achieved by following a different magnetisation protocol. Here the different thermomagnetic histories were reproduced and studied in a direct measurement using the field-sweeping capability of the microcalorimeter. It has been shown that while there are differences in the directly observed MCE due to thermomagnetic history, they do not amount to a 'colossal' MCE. Thus it was confirmed that the concentration of entropy change resulting in the 'colossal' MCE, as given by the Maxwell relation, is artificial.

It has also been shown that colossal MCE cannot be observed by driving the sample through the phase transition in a mixed-phase state, as it has been confirmed quantitatively here that the first order contribution to the total entropy change scales with the phase fractions (Kuepferling et al., 2008). This validates various numerical and graphical approaches used to recover non-colossal MCE estimates from the magnetisation data using phase fractions, e.g. in Liu et al. (2007); Tocado et al. (2009); Balli et al. (2009); Cui et al. (2010); Das et al. (2010a).

More subtle effects of hysteresis were studied by considering an isothermal magnetisation cycle through a hysteresis region. It was shown that the use of Maxwell relation as well as Clausius-Clapeyron equation can lead to erroneous estimates of isothermal entropy change in systems with temperature dependent hysteresis. These are apparent when comparing estimates on field application and removal and result in a non-physical difference between the two. This effect is beyond and above the 'colossal' artefact. It is linked to the slope of a hysteretic first order phase line and it cannot be avoided by any particular magnetisation history. It forms an intrinsic limitation of the use Maxwell relation, which assumes equilibrium thermodynamics, when applied to hysteretic systems. Thus, if using the Maxwell relation for sample characterisation, the estimates on field application and removal should be checked for consistency.

An apparent difference in the entropy change of the sample on field application and removal was observed also in the direct calorimetric measurement, however, this was smaller and in opposite sense. It was attributed to the dissipation of irreversible magnetic work performed on the sample in the hysteretic magnetisation/demagnetisation cycle. This observation was confirmed in two systems with fundamentally different manifestation of the MCE: a material with conventional MCE ($Mn_{0.985}Fe_{0.015}As$) and a material with inverse MCE (CoMnSi). While in both cases the net heat expelled agreed quantitatively with the expected magnitude of the irreversible work, the uncertainty in the calorimetric measurements was too large to make any conclusions other than qualitative ones about the sign of the net heat.

Part of the reason for caution is a currently unexplained correction factor of 2 that had to be applied to all ac heat capacity data. A thorough review of the microcalorimeter has been undertaken but a definitive reason for a factor of 2 correction could not be established without further measurements. Nevertheless, as an outcome of the review, several suggestions were made to improve the precision and accuracy of the calorimeter. With these implemented, a better precision in the net heat dissipation measurement above could be achieved.

Finally, a significant work was done on the analysis method to accurately separate the first and higher order contributions to isothermal entropy change, utilising the unique feature of the microcalorimeter to measure the latent heat and ac heat capacity separately. It also was proposed how the ac heat capacity data could be used to infer latent heat when it is to small or distributed to measure using the latent heat measurement. An experimental method was proposed to measure an equilibrium entropy change of a FOPT in systems with a tricritical point.

Chapter 7

Further Work

Microcalorimeter development

The most pressing issue to address is the correction factor of 2 in the heat capacity probe. A possible reason for the correction may be an error in the Seebeck coefficient arising from an improper use of the heater resistance for measuring the local temperature. For instance, there could be a difference in self-heated and zero-power heater resistance as a function of temperature. This hypothesis may be tested by measuring a sample with a sharp feature in $C(T)$. Its temperature dependence could be measured as a function of heater resistance in self-heating mode (by applying dc offset at constant bath temperature) and as a function of bath temperature directly. This has not been addressed here simply due to a lack of time.

Irrespective of the outcome of the above, a reference sample should be measured. A magnetic sample, such as Ni or Gd could be used. The saturation magnetisation of the fragment could provide an alternative and possibly more accurate measurement of sample mass. The setup improvements suggested in chapter 2 should be implemented for higher precision and accuracy.

Results improvement

The results presented here could be measured with the improved microcalorimeter. A more precise measurement would allow for more quantitative statements regarding the amount of irreversible heat we measure and its dynamics. For example, is all the irreversible heat dissipated at the FOPT?

Exploring the free energy landscape near tricritical point

An analysis method was proposed that could measure the equilibrium entropy change of a FOPT by integrating heat capacity data around a tricritical point. The equilibrium entropy change could be compared with the effective entropy change measured directly at the FOPT which should include heat flux due to irreversible work. By doing so on both field application and removal, it may be possible to determine the relative amounts of irreversible work dissipated and estimate the critical field corresponding to the equilibrium phase line.

Bibliography

J. S. Amaral and V. S. Amaral. The effect of magnetic irreversibility on estimating the magnetocaloric effect from magnetization measurements. *Appl. Phys. Lett.*, 94(4):042506, 2009.

J.S. Amaral and V.S. Amaral. On estimating the magnetocaloric effect from magnetization measurements. *J. Magn. Magn. Mater.*, 322(9–12):1552 – 1557, 2010.

M. Balli, D. Fruchart, D. Gignoux, and R. Zach. The "colossal" magnetocaloric effect in $Mn_{1-x}Fe_xAs$: What are we really measuring? *Appl. Phys. Lett.*, 95(7):072509, 2009.

A. Barcza, Z. Gercsi, H. Michor, K. Suzuki, W. Kockelmann, K. S. Knight, and K. G. Sandeman. Magnetoelastic coupling and competing entropy changes in substituted CoMnSi metamagnets. *Phys. Rev. B*, 87:064410, 2013.

V. Basso, M. Kupferling, C. P. Sasso, and L. Giudici. A peltier cell calorimeter for the direct measurement of the isothermal entropy change in magnetic materials. *Rev. Sci. Instrum.*, 79(6):063907, 2008.

G. V. Brown. Magnetic heat pumping near room-temperature. *J. Appl. Phys.*, 47(8):3673–3680, 1976.

L. Caron, Z. Q. Ou, T. T. Nguyen, D. T. C. Thanh, O. Tegus, and E. Bruck. On the determination of the magnetic entropy change in materials with first-order transitions. *J. Magn. Magn. Mater.*, 321(21):3559, 2009.

D. Coulomb. Thermag IV conference foreword. In P. W. Egolf, editor, *Fourth IIF-IIR International Conference on Magnetic Refrigeration at Room Temperature*, 2010.

W. B. Cui, W. Liu, and Z. D. Zhang. The origin of large overestimation of the magnetic entropy changes calculated directly by maxwell relation. *Appl. Phys. Lett.*, 96(22):222509, 2010.

S. Y. Dankov, A. M. Tishin, V. K. Pecharsky, and K. A. Gschneider. Experimental device for studying the magnetocaloric effect in pulse magnetic fields. *Rev. Sci. Instrum.*, 68(6): 2432–2437, 1997.

S. Das, J. S. Amaral, and V. S. Amaral. Prediction of realistic entropy behavior from mixed state magnetization data for first order phase transition materials. *J. Appl. Phys.*, 107(9): 09A912, 2010a.

S. Das, J. S. Amaral, and V. S. Amaral. Handling mixed-state magnetization data for magnetocaloric studies-a solution to achieve realistic entropy behaviour. *J. Phys. D: Appl. Phys.*, 43(15):152002, 2010b.

A. de Campos, D. L. Rocco, A. M. G. Carvalho, L. Caron, A. A. Coelho, S. Gama, L. M. da Silva, F. C. G. Gandra, A. O. dos Santos, L. P. Cardoso, P. J. von Ranke, and N. A. de Oliveira. Ambient pressure colossal magnetocaloric effect tuned by composition in $Mn_{1-x}Fe_xAs$. *Nature Mater.*, 5(10):802, 2006.

H. Fjellvåg, A. Kjekshus, A. F. Andresen, and A. Zieba. Structural and magnetic properties of $Mn_{1-t}Fe_tAs$ ($0.00 \leq t \leq 0.20$). *J. Magn. Magn. Mater.*, 73(3):318, 1988.

Simon Foner. Versatile and sensitive vibrating-sample magnetometer. *Review of Scientific Instruments*, 30(7):548–557, 1959.

S. Gama, A. A. Coelho, A. de Campos, A. M. G. Carvalho, F. C. G. Gandra, P. J. von Ranke, and N. A. de Oliveira. Pressure-induced colossal magnetocaloric effect in MnAs. *Phys. Rev. Lett.*, 93:237202, 2004.

S. Gama, A. de Campos, A. A. Coelho, C. S. Alves, Y. Ren, F. Garcia, D. E. Brown, L. M. da Silva, A. M. G. Carvalho, F. C. G. Gandra, A. O. dos Santos, L. P. Cardoso, and P. J. von Ranke. A general approach to first order phase transitions and the anomalous behavior of coexisting phases in the magnetic case. *Adv. Funct. Mater.*, 19(6):942–949, 2009.

W. F. Giauque and D. P. MacDougall. Attainment of temperatures below 1° absolute by demagnetization of $Gd_2(SO_4)_3 \cdot 8H_2O$. *Phys. Rev.*, 43(9):768, 1933.

A. Giguere, M. Foldeaki, B. R. Gopal, R. Chahine, T. K. Bose, A. Frydman, and J. A. Barclay. Direct measurement of the "giant" adiabatic temperature change in $Gd_5Si_2Ge_2$. *Phys. Rev. Lett.*, 83(11):2262–2265, 1999.

B. R. Gopal, R. Chahine, and T. K. Bose. Sample translatory type insert for automated magnetocaloric effect measurements. *Rev. Sci. Instrum.*, 68(4):1818–1822, 1997.

B. Hernando, J. L. S. Llamazares, V. M. Prida, D. Baldomir, D. Serantes, M. Ilyn, and J. Gonzalez. Magnetocaloric effect in preferentially textured $Mn_{50}Ni_{40}In_{10}$ melt spun ribbons. *Appl. Phys. Lett.*, 94(22):222502, 2009.

S. Jeppesen, S. Linderoth, N. Pryds, L. Theil Kuhn, and J. Buch Jensen. Indirect measurement of the magnetocaloric effect using a novel differential scanning calorimeter with magnetic field. *Review of Scientific Instruments*, 79(8), 2008.

M. Kuepferling, V. Basso, C. P. Sasso, L. Giudici, J. D. Moore, K. Morrison, and L. F. Cohen. Hall imaging of the history dependence of the magnetocaloric effect in $Gd_5Si_{2.09}Ge_{1.91}$. *IEEE T. Magn.*, 44(11):3233–3236, 2008.

G. J. Liu, J. R. Sun, J. Shen, B. Gao, H. W. Zhang, F. X. Hu, and B. G. Shen. Determination of the entropy changes in the compounds with a first-order magnetic transition. *Appl. Phys. Lett.*, 90(3):032507, 2007.

J. Marcos, F. Casanova, X. Batlle, A. Labarta, A. Planes, and L. Manosa. A high-sensitivity

differential scanning calorimeter with magnetic field for magnetostructural transitions. *Rev. Sci. Instrum.*, 74(11):4768–4771, 2003.

N. Menyuk, J. A. Kafalas, K. Dwight, and J. B. Goodenough. Effects of pressure on the magnetic properties of MnAs. *Phys. Rev.*, 177(2):942, 1969.

A. A. Minakov, S. B. Roy, Y. V. Bugoslavsky, and L. F. Cohen. Thin-film alternating current nanocalorimeter for low temperatures and high magnetic fields. *Rev. Sci. Instrum.*, 76(4): 043906, 2005.

Y. Miyoshi, K. Morrison, J. D. Moore, A. D. Caplin, and L. F. Cohen. Heat capacity and latent heat measurements of CoMnSi using a microcalorimeter. *Rev. Sci. Instrum.*, 79(7): 074901, 2008.

K. Morrison. *Study of first order magnetocaloric materials*. PhD thesis, Imperial College, Universtity of London, 2010.

K. Morrison, J. Lyubina, J. D. Moore, A. D. Caplin, K. G. Sandeman, O. Gutfleisch, and L. F. Cohen. Contributions to the entropy change in melt-spun $LaFe_{11.6}Si_{1.4}$. *J. Phys. D: Appl. Phys.*, 43(13), April 7 2010.

K. Morrison, M. Bratko, J. Turcaud, A. Berenov, A. D. Caplin, and L. F. Cohen. A calorimetric method to detect a weak or distributed latent heat contribution at first order magnetic transitions. *Rev. Sci. Instrum.*, 83(3):033901, 2012.

A. K. Pathak, M. Khan, I. Dubenko, S. Stadler, and N. Ali. Large magnetic entropy change in $Ni_{50}Mn_{50-x}In_x$ heusler alloys. *Appl. Phys. Lett.*, 90(26):262504, 2007.

V. K. Pecharsky and K. A. Gschneidner. Giant magnetocaloric effect in $Gd_5(Si_2Ge_2)$. *Phys. Rev. Lett.*, 78(23):4494–4497, 1997a.

V. K. Pecharsky and K. A. Gschneidner. Tunable magnetic regenerator alloys with a giant magnetocaloric effect for magnetic refrigeration from ∼20 to ∼290 k. *Appl. Phys. Lett.*, 70 (24):3299–3301, 1997b.

V. K. Pecharsky and K. A. Gschneidner. Effect of alloying on the giant magnetocaloric effect of $Gd_5(Si_2Ge_2)$. *J. Magn. Magn. Mater.*, 167(3):L179–L184, 1997c.

V. K. Pecharsky, K. A. Gschneidner, A. O. Pecharsky, and A. M. Tishin. Thermodynamics of the magnetocaloric effect. *Phys. Rev. B*, 64:144406, 2001.

Quantum Design. *Physical Property Measurement System, Vibrating Sample Magnetometer (VSM) Option User's Manual*. Quantum Design, 6325 Lusk Boulevard, San Diego, CA 92121, USA, fourth edition, January 2008.

N. V. R. Rao, R. Gopalan, V. Chandrasekaran, and K. G. Suresh. Microstructure, magnetic properties and magnetocaloric effect in melt-spun Ni-Mn-Ga ribbons. *J. Alloy Compd.*, 478(1-2):59–62, 2009.

K. G. Sandeman. Gas-free refrigeration. *Magnetics Technology International*, Showcase 2011: 32–34, 2011.

K. G. Sandeman, R. Daou, S. Özcan, J. H. Durrell, N. D. Mathur, and D. J. Fray. Negative magnetocaloric effect from highly sensitive metamagnetism in $CoMnSi_{1-x}Ge_x$. *Phys. Rev. B*, 74:224436, 2006.

J. R. Sun, F. X. Hu, and B. G. Shen. Comment on "direct measurement of the 'giant' adiabatic temperature change in $Gd_5Si_2Ge_2$". *Phys. Rev. Lett.*, 85(19):4191–4191, 2000.

O. Tegus, E. Bruck, K. H. J. Buschow, and F. R. de Boer. Transition-metal-based magnetic refrigerants for room-temperature applications. *Nature*, 415(6868):150–152, 2002.

W. Thomson. *Cyclopedia of the Physical Sciences*. Richard Green and Company, London and Glasgow, 2nd edition, 1860.

A. M. Tishin and Y. I. Spichkin. *The magnetocaloric effect and its applications*. Series in condensed matter physics. Institute of Physics Pub., Bristol and Philadelphia, 2003.

L. Tocado, E. Palacios, and R. Burriel. Entropy determinations and magnetocaloric parameters in systems with first-order transitions: Study of MnAs. *J. Appl. Phys.*, 105(9):093918, 2009.

T. Tohei, H. Wada, and T. Kanomata. Negative magnetocaloric effect at the antiferromagnetic to ferromagnetic transition of Mn_3GaC. *J. Appl. Phys.*, 94(3):1800–1802, 2003.

Sander van Herwaarden. Thermal Conductivity Gauge XEN-TCG3880, October 2010. URL http://www.xensor.nl/pdffiles/sheets/xen-tcg3880.pdf.

Sander van Herwaarden. Gas Nanocalorimeters XEN-39390 series, January 2013. URL http://www.xensor.nl/pdffiles/sheets/nanogas3939.pdf.

P. J. von Ranke, S. Gama, A. A. Coelho, A. de Campos, A. M. G. Carvalho, F. C. G. Gandra, and N. A. de Oliveira. Theoretical description of the colossal entropic magnetocaloric effect: Application to MnAs. *Phys. Rev. B*, 73:014415, 2006.

H. Wada and Y. Tanabe. Giant magnetocaloric effect of $MnAs_{1-x}Sb_x$. *Appl. Phys. Lett.*, 79 (20):3302, 2001.

G. F. Wang, E. Palacios, R. Burriel, A. A. Coelho, and S. Gama. Direct and indirect determinations of the giant magnetocaloric effect in $Mn_{1-x}Co_xAs$ compounds. In P. W. Egolf, editor, *Proceedings of the 4th International Conference on Magnetic Refrigeration at Room Temperature*, pages 233–244, Paris, 2010. IIR.

P. Weiss and A. Piccard. Le phénomène magnétocalorique. *J. Phys. (Paris)*, 5th Ser. 7:103–109, 1917.

A. Zieba, R. Zach, H. Fjellvåg, and A. Kjekshus. Effect of external-pressure and chemical substitution on the phase-transitions in MnAs. *J. Phys. Chem. Solids.*, 48(1):79–89, 1987.

Appendix A

Copyright Permissions

Summary of copyright permissions

Page number	Content type	Source	Copyright holder & year	Permission to re-use
16-23	figures	Pecharsky et al. (2001)	©2001 American Physical Society	Granted (p. 147)
24	figures	Pecharsky and Gschneidner (1997a)	©1997 American Physical Society	Granted (p. 147)
30	images	van Herwaarden (2013)	©2013 Xensor Integration	Granted (p. 148)
87	figures	Wada and Tanabe (2001)	©2001 AIP Publishing LLC	Granted (p. 149)
88	figures	Gama et al. (2004)	©2004 American Physical Society	Granted (p. 147)
89	figure	Menyuk et al. (1969)	©1969 American Physical Society	Granted (p. 147)
90	figure	Fjellvåg et al. (1988)	©1988 Elsevier	Granted (p. 150)
91	figures	de Campos et al. (2006)	©2006 Macmillan Publishers Ltd	Granted (p. 151)
92	figure	von Ranke et al. (2006)	©2006 American Physical Society	Granted (p. 147)
93-94	figures	Liu et al. (2007)	©2007 AIP Publishing LLC	Granted (p. 152)
96	figure	Tocado et al. (2009)	©2009 AIP Publishing LLC	Granted (p. 153)
97-98	figures	Caron et al. (2009)	©2009 Elsevier	Granted (p. 154)
100	figures	Amaral and Amaral (2009)	©2009 AIP Publishing LLC	Granted (p. 155)
102	text	de Campos et al. (2006)	©2006 Macmillan Publishers Ltd	Granted (p. 156)
103	text	Fjellvåg et al. (1988)	©1988 Elsevier	Granted (p. 157)

AMERICAN PHYSICAL SOCIETY
One Physics Ellipse, College Park, MD 20740 · http://www.aps.org

October 11, 2013

Milan Bratko
Imperial College London
m.bratko09@imperial.ac.uk

Ref # 24763

Thank you for your permission request dated Oct. 7, 2013. We are pleased to grant you a non-exclusive, non-transferable permission, English rights, limited to **print and electronic format**, provided you meet the criteria outlined below. Permission is for a one-time use and does not include permission for future editions, updates, databases, translations, or any other matters. Permission must be sought for each additional use. This permission does not include the right to modify APS material.

Please print the required copyright credit line on the first page that the material appears: "Reprinted (abstract/excerpt/figure) with permission from [FULL REFERENCE CITATION] as follows: authors names, journal title, volume number, page number and year of publication. Copyright (YEAR) by the American Physical Society.

The following language must appear somewhere on the website: "Readers may view, browse, and/or download material for temporary copying purposes only, provided these uses are for noncommercial personal purposes. Except as provided by law, this material may not be further reproduced, distributed, transmitted, modified, adapted, performed, displayed, published, or sold in whole or part, without prior written permission from the American Physical Society."

Provide a hyperlink from the reprinted APS material (the hyperlink may be embedded in the copyright credit line). APS's link manager technology makes it convenient and easy to provide links to individual articles in APS journals. For information, see: http://link.aps.org/.

You must also obtain permission from at least one of the authors for each separate work, if you haven't done so already. The author's name and address can be found on the first page of the published Article.

Use of the APS material must not imply any endorsement by the American Physical Society.

Permission is granted for use of the following APS material only:

- Figs. 1, 7, 9, 10, 11, Phys. Rev. B 64, 144406 (2001)
- Fig. 1, Phys. Rev. B 73, 014415 (2006)
- Fig. 12, Phys. Rev. 177, 942–951 (1969)
- Figs. 3, 4, Phys. Rev. Lett. 78, 4494–4497 (1997)
- Figs. 1, 2, Phys. Rev. Lett. 93, 237202 (2004)

Permission is limited to the single title specified of the publication as follows:
A thesis entitled 'The Magnetocaloric Effect at a First Order Phase Transition' which will be added to Spiral, Imperial's online repository http://spiral.imperial.ac.uk/.

If you have any questions, please refer to the Copyright FAQ at: http://publish.aps.org/copyrightFAQ.html or send an email to assocpub@aps.org.

Sincerely,

Alex Menendez
Publications Marketing Coordinator

Bratko, Milan

From: Xensor Integration bv <info@xensor.nl>
Sent: 11 October 2013 09:28
To: Bratko, Milan
Subject: RE: Copyright Permission Request

Dear Milan

I confirm that I am the copyright holder of the extract above and hereby give permission to include it in the print and electronic version of your thesis. I understand that the electronic version of the thesis will be made available, via the internet, for non-commercial purposes under the terms of the user licence.

met vriendelijke groet, best regards, Sander

Xensor Integration bv *X-cellence through X-perience*
dr.ir. A.W. van Herwaarden, PhD

address: Distributieweg 28, 2645 EJ Delfgauw, The Netherlands
phone: +31 15 257 80 40, fax: +31 15 257 80 50
email: svh@xensor.nl, website: www.xensor.nl

CONFIDENTIAL: Xensor copyright. This document (its contents and all appertained matters): is confidential, belongs to and is property of Xensor, and may not be copied, reproduced, displayed, modified, disclosed or transferred in any manner to any unauthorized person without written permission from Xensor.
OFFERS+AGREEMENTS: All our offers and agreements are governed by the FHI General Conditions of Delivery 2010 issued by FHI, Federation of Technology Branches, filed at the Chamber of Commerce of Gooi-, Eem- and Flevoland under the number 40507574.
See http://www.xensor.nl/pdffiles/divers/fhi-levervw-en-2010.pdf

Van: Bratko, Milan [mailto:m.bratko09@imperial.ac.uk]
Verzonden: maandag 7 oktober 2013 15:10
Aan: 'info@xensor.nl'
Onderwerp: Copyright Permission Request

To whom it may concern,

I have completed my **PhD thesis** at Imperial College London entitled '**The Magnetocaloric Effect at a First Order Phase Transition**'.

I seek your permission to reprint, in my thesis extracts from **Gas Nanocalorimeters XEN-39390 series by Sander van Herwaarden, January 2013**. The extract to be reproduced is: **figures 2.2 and 2.3**.

I would like to include the extracts in the **printed examination copy** of my thesis and also the **electronic version which will be added to Spiral**, Imperial's online repository http://spiral.imperial.ac.uk/ and made available to the public under a Creative Commons Attribution-NonCommercial-NoDerivs licence – **no fee** will be charged.

If you are happy to grant me all the permissions requested, please return a signed copy of this email. If you wish to grant only some of the permissions requested, please list these and then sign.

Best Regards,

Milan Bratko

AIP PUBLISHING LLC LICENSE
TERMS AND CONDITIONS

Sep 30, 2013

All payments must be made in full to CCC. For payment instructions, please see information listed at the bottom of this form.

License Number	3238720698096
Order Date	Sep 30, 2013
Publisher	AIP Publishing LLC
Publication	Applied Physics Letters
Article Title	Giant magnetocaloric effect of MnAs1−xSbx
Author	H. Wada, Y. Tanabe
Online Publication Date	Nov 12, 2001
Volume number	79
Issue number	20
Type of Use	Thesis/Dissertation
Requestor type	Student
Format	Print and electronic
Portion	Figure/Table
Number of figures/tables	2
Title of your thesis / dissertation	The magnetocaloric effect at a first order phase transition
Expected completion date	Sep 2013
Estimated size (number of pages)	150
Total	0.00 GBP
Terms and Conditions	

AIP Publishing LLC -- Terms and Conditions: Permissions Uses

AIP Publishing LLC ("AIPP"") hereby grants to you the non-exclusive right and license to use and/or distribute the Material according to the use specified in your order, on a one-time basis, for the specified term, with a maximum distribution equal to the number that you have ordered. Any links or other content accompanying the Material are not the subject of this license.

1. You agree to include the following copyright and permission notice with the reproduction of the Material:"Reprinted with permission from [FULL CITATION]. Copyright [PUBLICATION YEAR], AIP Publishing LLC." For an article, the copyright and permission notice must be printed on the first page of the article or book chapter. For photographs, covers, or tables, the copyright and permission notice may appear with the Material, in a footnote, or in the reference list.
2. If you have licensed reuse of a figure, photograph, cover, or table, it is your responsibility to ensure that the material is original to AIPP and does not contain the copyright of another entity, and that the copyright notice of the figure, photograph, cover, or table does not indicate that it was reprinted by AIPP, with permission, from another source. Under no circumstances does AIPP, purport or intend to grant permission to reuse material to which it does not hold copyright.
3. You may not alter or modify the Material in any manner. You may translate the Material into another language only if you have licensed translation rights. You may not use the Material for promotional purposes. AIPP reserves all rights not specifically granted herein.

ELSEVIER LICENSE
TERMS AND CONDITIONS

Sep 30, 2013

This is a License Agreement between Milan Bratko ("You") and Elsevier ("Elsevier") provided by Copyright Clearance Center ("CCC"). The license consists of your order details, the terms and conditions provided by Elsevier, and the payment terms and conditions.

All payments must be made in full to CCC. For payment instructions, please see information listed at the bottom of this form.

Supplier	Elsevier Limited The Boulevard,Langford Lane Kidlington,Oxford,OX5 1GB,UK
Registered Company Number	1982084
Customer name	Milan Bratko
Customer address	
License number	3238721295646
License date	Sep 30, 2013
Licensed content publisher	Elsevier
Licensed content publication	Journal of Magnetism and Magnetic Materials
Licensed content title	Structural and magnetic properties of Mn1−*t*Fe*t*As (0.00 ≤*t*≤ 0.20)
Licensed content author	H. Fjellvåg,A. Kjekshus,A.F. Andresen,A. Zięba
Licensed content date	July 1988
Licensed content volume number	73
Licensed content issue number	3
Number of pages	9
Start Page	318
End Page	326
Type of Use	reuse in a thesis/dissertation
Intended publisher of new work	other
Portion	figures/tables/illustrations
Number of figures/tables/illustrations	1
Format	both print and electronic
Are you the author of this Elsevier article?	No
Will you be translating?	No
Order reference number	

NATURE PUBLISHING GROUP LICENSE
TERMS AND CONDITIONS

Sep 30, 2013

This is a License Agreement between Milan Bratko ("You") and Nature Publishing Group ("Nature Publishing Group") provided by Copyright Clearance Center ("CCC"). The license consists of your order details, the terms and conditions provided by Nature Publishing Group, and the payment terms and conditions.

All payments must be made in full to CCC. For payment instructions, please see information listed at the bottom of this form.

License Number	3238711135471
License date	Sep 30, 2013
Licensed content publisher	Nature Publishing Group
Licensed content publication	Nature Materials
Licensed content title	Ambient pressure colossal magnetocaloric effect tuned by composition in Mn1|[minus]|xFexAs
Licensed content author	Ariana de Campos,Daniel L Rocco,Alexandre Magnus G. Carvalho,Luana Caron,Adelino A. Coelho et al.
Licensed content date	Oct 1, 2006
Volume number	5
Issue number	10
Type of Use	reuse in a thesis/dissertation
Requestor type	academic/educational
Format	print and electronic
Portion	figures/tables/illustrations
Number of figures/tables/illustrations	2
High-res required	no
Figures	Figure 3b, Figure 4
Author of this NPG article	no
Your reference number	
Title of your thesis / dissertation	The magnetocaloric effect at a first order phase transition
Expected completion date	Sep 2013
Estimated size (number of pages)	150
Total	0.00 GBP
Terms and Conditions	

Terms and Conditions for Permissions

AIP PUBLISHING LLC LICENSE
TERMS AND CONDITIONS

Sep 30, 2013

All payments must be made in full to CCC. For payment instructions, please see information listed at the bottom of this form.

License Number	3238720805728
Order Date	Sep 30, 2013
Publisher	AIP Publishing LLC
Publication	Applied Physics Letters
Article Title	Determination of the entropy changes in the compounds with a first-order magnetic transition
Author	G. J. Liu, J. R. Sun, J. Shen, B. Gao, et al.
Online Publication Date	Jan 18, 2007
Volume number	90
Issue number	3
Type of Use	Thesis/Dissertation
Requestor type	Student
Format	Print and electronic
Portion	Figure/Table
Number of figures/tables	3
Title of your thesis / dissertation	The magnetocaloric effect at a first order phase transition
Expected completion date	Sep 2013
Estimated size (number of pages)	150
Total	0.00 GBP

Terms and Conditions

AIP Publishing LLC -- Terms and Conditions: Permissions Uses

AIP Publishing LLC ("AIPP"") hereby grants to you the non-exclusive right and license to use and/or distribute the Material according to the use specified in your order, on a one-time basis, for the specified term, with a maximum distribution equal to the number that you have ordered. Any links or other content accompanying the Material are not the subject of this license.

1. You agree to include the following copyright and permission notice with the reproduction of the Material:"Reprinted with permission from [FULL CITATION]. Copyright [PUBLICATION YEAR], AIP Publishing LLC." For an article, the copyright and permission notice must be printed on the first page of the article or book chapter. For photographs, covers, or tables, the copyright and permission notice may appear with the Material, in a footnote, or in the reference list.
2. If you have licensed reuse of a figure, photograph, cover, or table, it is your responsibility to ensure that the material is original to AIPP and does not contain the copyright of another entity, and that the copyright notice of the figure, photograph, cover, or table does not indicate that it was reprinted by AIPP, with permission, from another source. Under no circumstances does AIPP, purport or intend to grant permission to reuse material to which it does not hold copyright.
3. You may not alter or modify the Material in any manner. You may translate the Material into another language only if you have licensed translation rights. You may not use the Material

AIP PUBLISHING LLC LICENSE
TERMS AND CONDITIONS

Sep 30, 2013

All payments must be made in full to CCC. For payment instructions, please see information listed at the bottom of this form.

License Number	3238720429055
Order Date	Sep 30, 2013
Publisher	AIP Publishing LLC
Publication	Journal of Applied Physics
Article Title	Entropy determinations and magnetocaloric parameters in systems with first-order transitions: Study of MnAs
Author	Leticia Tocado, Elías Palacios, Ramón Burriel
Online Publication Date	May 11, 2009
Volume number	105
Issue number	9
Type of Use	Thesis/Dissertation
Requestor type	Student
Format	Print and electronic
Portion	Figure/Table
Number of figures/tables	1
Title of your thesis / dissertation	The magnetocaloric effect at a first order phase transition
Expected completion date	Sep 2013
Estimated size (number of pages)	150
Total	0.00 GBP

Terms and Conditions

AIP Publishing LLC -- Terms and Conditions: Permissions Uses

AIP Publishing LLC ("AIPP"") hereby grants to you the non-exclusive right and license to use and/or distribute the Material according to the use specified in your order, on a one-time basis, for the specified term, with a maximum distribution equal to the number that you have ordered. Any links or other content accompanying the Material are not the subject of this license.

1. You agree to include the following copyright and permission notice with the reproduction of the Material:"Reprinted with permission from [FULL CITATION]. Copyright [PUBLICATION YEAR], AIP Publishing LLC." For an article, the copyright and permission notice must be printed on the first page of the article or book chapter. For photographs, covers, or tables, the copyright and permission notice may appear with the Material, in a footnote, or in the reference list.
2. If you have licensed reuse of a figure, photograph, cover, or table, it is your responsibility to ensure that the material is original to AIPP and does not contain the copyright of another entity, and that the copyright notice of the figure, photograph, cover, or table does not indicate that it was reprinted by AIPP, with permission, from another source. Under no circumstances does AIPP, purport or intend to grant permission to reuse material to which it does not hold copyright.
3. You may not alter or modify the Material in any manner. You may translate the Material into another language only if you have licensed translation rights. You may not use the Material

ELSEVIER LICENSE
TERMS AND CONDITIONS

Sep 30, 2013

This is a License Agreement between Milan Bratko ("You") and Elsevier ("Elsevier") provided by Copyright Clearance Center ("CCC"). The license consists of your order details, the terms and conditions provided by Elsevier, and the payment terms and conditions.

All payments must be made in full to CCC. For payment instructions, please see information listed at the bottom of this form.

Supplier	Elsevier Limited The Boulevard,Langford Lane Kidlington,Oxford,OX5 1GB,UK
Registered Company Number	1982084
Customer name	Milan Bratko
Customer address	
License number	3238730258835
License date	Sep 30, 2013
Licensed content publisher	Elsevier
Licensed content publication	Journal of Magnetism and Magnetic Materials
Licensed content title	On the determination of the magnetic entropy change in materials with first-order transitions
Licensed content author	L. Caron,Z.Q. Ou,T.T. Nguyen,D.T. Cam Thanh,O. Tegus,E. Brück
Licensed content date	November 2009
Licensed content volume number	321
Licensed content issue number	21
Number of pages	8
Start Page	3559
End Page	3566
Type of Use	reuse in a thesis/dissertation
Intended publisher of new work	other
Portion	figures/tables/illustrations
Number of figures/tables/illustrations	3
Format	both print and electronic
Are you the author of this Elsevier article?	No
Will you be translating?	No

AIP PUBLISHING LLC LICENSE
TERMS AND CONDITIONS

Sep 30, 2013

All payments must be made in full to CCC. For payment instructions, please see information listed at the bottom of this form.

License Number	3238720896082
Order Date	Sep 30, 2013
Publisher	AIP Publishing LLC
Publication	Applied Physics Letters
Article Title	The effect of magnetic irreversibility on estimating the magnetocaloric effect from magnetization measurements
Author	J. S. Amaral, V. S. Amaral
Online Publication Date	Jan 27, 2009
Volume number	94
Issue number	4
Type of Use	Thesis/Dissertation
Requestor type	Student
Format	Print and electronic
Portion	Figure/Table
Number of figures/tables	2
Title of your thesis / dissertation	The magnetocaloric effect at a first order phase transition
Expected completion date	Sep 2013
Estimated size (number of pages)	150
Total	0.00 GBP

Terms and Conditions

AIP Publishing LLC -- Terms and Conditions: Permissions Uses

AIP Publishing LLC ("AIPP"") hereby grants to you the non-exclusive right and license to use and/or distribute the Material according to the use specified in your order, on a one-time basis, for the specified term, with a maximum distribution equal to the number that you have ordered. Any links or other content accompanying the Material are not the subject of this license.

1. You agree to include the following copyright and permission notice with the reproduction of the Material:"Reprinted with permission from [FULL CITATION]. Copyright [PUBLICATION YEAR], AIP Publishing LLC." For an article, the copyright and permission notice must be printed on the first page of the article or book chapter. For photographs, covers, or tables, the copyright and permission notice may appear with the Material, in a footnote, or in the reference list.
2. If you have licensed reuse of a figure, photograph, cover, or table, it is your responsibility to ensure that the material is original to AIPP and does not contain the copyright of another entity, and that the copyright notice of the figure, photograph, cover, or table does not indicate that it was reprinted by AIPP, with permission, from another source. Under no circumstances does AIPP, purport or intend to grant permission to reuse material to which it does not hold copyright.
3. You may not alter or modify the Material in any manner. You may translate the Material into another language only if you have licensed translation rights. You may not use the Material

NATURE PUBLISHING GROUP LICENSE
TERMS AND CONDITIONS

Sep 30, 2013

This is a License Agreement between Milan Bratko ("You") and Nature Publishing Group ("Nature Publishing Group") provided by Copyright Clearance Center ("CCC"). The license consists of your order details, the terms and conditions provided by Nature Publishing Group, and the payment terms and conditions.

All payments must be made in full to CCC. For payment instructions, please see information listed at the bottom of this form.

License Number	3238711361240
License date	Sep 30, 2013
Licensed content publisher	Nature Publishing Group
Licensed content publication	Nature Materials
Licensed content title	Ambient pressure colossal magnetocaloric effect tuned by composition in Mn1|[minus]|xFexAs
Licensed content author	Ariana de Campos,Daniel L Rocco,Alexandre Magnus G. Carvalho,Luana Caron,Adelino A. Coelho et al.
Licensed content date	Oct 1, 2006
Volume number	5
Issue number	10
Type of Use	reuse in a thesis/dissertation
Requestor type	academic/educational
Format	print and electronic
Portion	Text extract
Extract size	101 to 250 words
Circulation/distribution	<501
Author of this NPG article	no
Your reference number	
Title of your thesis / dissertation	The magnetocaloric effect at a first order phase transition
Expected completion date	Sep 2013
Estimated size (number of pages)	150
Total	0.00 GBP
Terms and Conditions	

Terms and Conditions for Permissions

Nature Publishing Group hereby grants you a non-exclusive license to reproduce this material for this purpose, and for no other use,subject to the conditions below:

ELSEVIER LICENSE
TERMS AND CONDITIONS

Sep 30, 2013

This is a License Agreement between Milan Bratko ("You") and Elsevier ("Elsevier") provided by Copyright Clearance Center ("CCC"). The license consists of your order details, the terms and conditions provided by Elsevier, and the payment terms and conditions.

All payments must be made in full to CCC. For payment instructions, please see information listed at the bottom of this form.

Supplier	Elsevier Limited The Boulevard,Langford Lane Kidlington,Oxford,OX5 1GB,UK
Registered Company Number	1982084
Customer name	Milan Bratko
Customer address	
License number	3238721437564
License date	Sep 30, 2013
Licensed content publisher	Elsevier
Licensed content publication	Journal of Magnetism and Magnetic Materials
Licensed content title	Structural and magnetic properties of Mn1−*t*Fe*t*As (0.00 ≤*t*≤ 0.20)
Licensed content author	H. Fjellvåg,A. Kjekshus,A.F. Andresen,A. Zięba
Licensed content date	July 1988
Licensed content volume number	73
Licensed content issue number	3
Number of pages	9
Start Page	318
End Page	326
Type of Use	reuse in a thesis/dissertation
Intended publisher of new work	other
Portion	excerpt
Number of excerpts	1
Format	both print and electronic
Are you the author of this Elsevier article?	No
Will you be translating?	No
Order reference number	